

# **NONEQUILIBRIUM RESPONSE AND DYNAMICS IN THE MOTT INSULATOR**

*By*

**ARIJIT DUTTA**

**PHYS08201105001**

**Harish-Chandra Research Institute, Prayagraj (Allahabad)**

*A thesis submitted to the*

*Board of Studies in Physical Sciences*

*In partial fulfillment of requirements*

*for the Degree of*

**DOCTOR OF PHILOSOPHY**

*of*

**HOMI BHABHA NATIONAL INSTITUTE**



**January, 2021**

# Homi Bhabha National Institute<sup>1</sup>

## Recommendations of the Viva Voce Committee

As members of the Viva Voce Committee, we certify that we have read the dissertation prepared by Arijit Dutta entitled “Nonequilibrium response and dynamics in the Mott insulator” and recommend that it may be accepted as fulfilling the thesis requirement for the award of Degree of Doctor of Philosophy.

---

Chairman – Prof. Sumathi Rao



Date: 08-06-2021

---

Guide / Convener – Prof. Pinaki Majumdar



Date: 08-06-2021

---

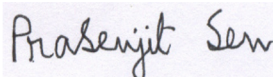
Examiner – Prof. Siddhartha Lal



Date: 08-06-2021

---

Member 1- Prof. Prasenjit Sen



Date: 08-06-2021

---

Member 2- Prof. Anirban Basu



Date: 08-06-2021

---

Member 3- Prof. Anshuman Maharana



Date: 08-06-2021


---

Final approval and acceptance of this thesis is contingent upon the candidate's submission of the final copies of the thesis to HBNI.

I/We hereby certify that I/we have read this thesis prepared under my/our direction and recommend that it may be accepted as fulfilling the thesis requirement.

Date: 08.06.2021

Place: Prayagraj



Prof. Pinaki Majumdar  
Guide

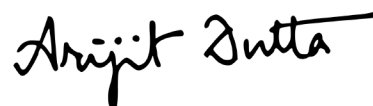
---

<sup>1</sup> This page is to be included only for final submission after successful completion of viva voce.

## **STATEMENT BY AUTHOR**

This dissertation has been submitted in partial fulfillment of requirements for an advanced degree at Homi Bhabha National Institute (HBNI) and is deposited in the Library to be made available to borrowers under rules of the HBNI.

Brief quotations from this dissertation are allowable without special permission, provided that accurate acknowledgement of source is made. Requests for permission for extended quotation from or reproduction of this manuscript in whole or in part may be granted by the Competent Authority of HBNI when in his or her judgment the proposed use of the material is in the interests of scholarship. In all other instances, however, permission must be obtained from the author.

A handwritten signature in black ink, reading 'Arijit Dutta' in a cursive script.

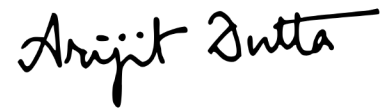
Arijit Dutta





## DECLARATION

I, hereby declare that the investigation presented in the thesis has been carried out by me. The work is original and has not been submitted earlier as a whole or in part for a degree / diploma at this or any other Institution / University.

A handwritten signature in black ink, reading "Arijit Dutta". The signature is written in a cursive, flowing style with a long horizontal stroke at the end.

Arijit Dutta



## List of Publications arising from the thesis

### Journal

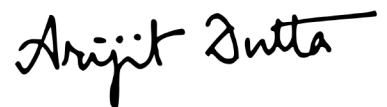
1. “Spatial behavior in a Mott insulator near the voltage-driven resistive transition”, Arijit Dutta and Pinaki Majumdar, Phys. Rev. B., **2020**, 101, 245155.

### Preprint

1. “Thermal fluctuation driven nonequilibrium resistive and magnetic transitions in a voltage biased Mott insulator”, Arijit Dutta and Pinaki Majumdar, arxiv: 2009.05533.

### Conferences

1. Presented a talk and a poster in **ICTP School and Conference on Complex Quantum Systems out of Equilibrium in Many-Body physics and Beyond** at Yerevan, Armenia, 2019 on “Voltage driven breakdown of a Mott insulator,” and “Suppression of thermal scales in a voltage driven Mott insulator” respectively.
2. Awarded for the best poster in **QMAT-2019** at IISC, Bangalore, 2019 on “Nonequilibrium phase transitions in a voltage driven Mott insulator.”
3. Awarded for the best short talk in **QMAT-2018** at IISER-Mohali, Chandigarh, 2018 on “Voltage driven breakdown of a Mott insulator.”
4. Participated and presented a poster in **International Workshop on Bose-Einstein Condensation and Related Phenomena (IWBECP)** at S. N. Bose National Centre for Basic Sciences, Kolkata, 2018 on “Thermal transitions of spin-orbit coupled superfluids.”



Arijit Dutta



## ACKNOWLEDGEMENTS

I would try to briefly mention all the people who have contributed significantly in my journey towards this thesis. The most significant academic contribution came from my supervisor, Prof. Pinaki Majumdar, who kept asking difficult questions and made sure I learned from my mistakes. I am thankful to him for his patience and due diligence. I am grateful to Prof. Kishnendu Sengupta for a fruitful collaboration and for providing guidance on several occasions. I thank Prof. Prasenjit Sen for his support and encouragement. His insights into several topics in physics and across disciplines, from politics to cricket, have enriched my experience in the formative years spent at HRI. Prof. Sumathi Rao is one of the kindest persons I have met. Apart from introducing me to the fascinating world of topological physics, she also provided much needed respite from the daily grind by hosting evening parties. Her presence was very reassuring as it would offer a space for sharing (read whining about) anything in the world.

I was fortunate to attend several courses offered by brilliant scientists during my integrated Ph.D. coursework. Out of them, I feel compelled to mention the ones taught by Prof. Ashoke Sen, Prof. Rajesh Gopakumar and Prof. Jayanta K. Bhattacharjee, as they have left a lasting impression on me. I must thank the administrative staff at HRI, and especially, Mr. Amit Roy for helping me on several occasions. I am grateful to Mr. Rajiv Kumar at the cluster facility for attending to technical problems even beyond the stipulated working hours. I also express my deepest gratitude to the ground-level workforce at HRI which has served delicious food, maintained the scenic beauty of the campus and guarded our boundaries. Their tedious, but crucial, labour has greatly contributed in making my extended stay at the institute a pleasant one.

In the course of this thesis I met several colleagues and made many friends. The seniors, Tarat-da, Rambha-da and Joshi (with whom I also had a chance to collaborate) were especially helpful. My batchmates, Sarosh and Nabarun were exceptionally brilliant and a source of inspiration. Dibya and Soumyadeep have been good friends since college. Arnab, Satadal, Subbu and Arpan-da have kept alive a ‘social life’ even in these difficult times amid the pandemic. I must thank all the people whom I met in several sporting activities at HRI, but primarily, badminton, cricket and table tennis. They are too numerous to be named here, but their contribution is invaluable as it was through these activities that I could cope with the stress of pursuing a Ph.D.

I am grateful to my parents for supporting me in my decision to pursue this unusual career. Their unwavering support has allowed me to continue this pursuit. I feel indebted to my friend and wife, Arpita, for her reaffirming presence in my life. It was her strength and courage that put me through the hardships I faced in this journey.

# Contents

<b>Summary</b>	<b>1</b>
<b>List of Figures</b>	<b>3</b>
<b>1 Introduction</b>	<b>13</b>
1.1 Overview . . . . .	13
1.2 The physics at equilibrium . . . . .	15
1.2.1 Mott insulators . . . . .	15
1.2.2 The Hubbard model . . . . .	16
1.2.3 Linear response theory . . . . .	18
1.3 Nonequilibrium experimental probes . . . . .	21
1.3.1 Transport measurements . . . . .	21
1.3.2 Pump-probe spectroscopy . . . . .	22
1.3.3 Ultracold atomic gases . . . . .	23
1.3.4 Inelastic neutron scattering . . . . .	25
1.4 Nonequilibrium theoretical approaches . . . . .	25
1.4.1 Time-dependent approaches . . . . .	26
1.4.2 Steady state approaches . . . . .	29
1.4.3 Auxiliary master equations . . . . .	32
1.5 Our motivation and principal results . . . . .	33
<b>2 Theoretical tools</b>	<b>35</b>
2.1 Model . . . . .	35
2.2 Methods . . . . .	36
2.2.1 Keldysh mean field theory at $T = 0$ . . . . .	38
2.2.2 Langevin for the thermal steady state . . . . .	41
2.2.3 Accessing equilibrium dynamics . . . . .	47
2.3 Observables . . . . .	50
2.3.1 Current . . . . .	50
2.3.2 Density of states . . . . .	52
2.3.3 Dynamical structure factor . . . . .	52
2.3.4 Static structure factor . . . . .	53

2.3.5	Magnetic moment distribution . . . . .	53
<b>3</b>	<b>Voltage driven insulator-metal transition at zero temperature</b>	<b>55</b>
3.1	Background . . . . .	55
3.2	Equilibrium mean-field theory . . . . .	57
3.3	Mean-field theory at finite bias . . . . .	58
3.3.1	I-V characteristic . . . . .	59
3.3.2	Density of states . . . . .	62
3.3.3	Charge and spin profiles . . . . .	64
3.4	Discussion . . . . .	67
3.4.1	Spectrum at finite bias . . . . .	67
3.4.2	Nature of the transition . . . . .	68
3.4.3	The large bias state . . . . .	68
3.4.4	Quantum fluctuations and long range Coulomb effects . . . . .	68
3.4.5	Numerical checks . . . . .	69
3.5	Conclusion . . . . .	70
<b>4</b>	<b>Nonequilibrium response of the Mott insulator at finite temperature</b>	<b>71</b>
4.1	Background . . . . .	72
4.2	Physics at equilibrium . . . . .	73
4.3	Effective Langevin equation . . . . .	75
4.4	Benchmarks . . . . .	76
4.5	Results at finite bias . . . . .	76
4.5.1	Magnetism and ‘phase diagram’ . . . . .	76
4.5.2	Transport characteristics . . . . .	79
4.5.3	Density of states . . . . .	80
4.5.4	Local charge and spin density . . . . .	82
4.6	Effective models . . . . .	83
4.6.1	$T = 0$ state at finite $V$ . . . . .	83
4.6.2	Suppression of Néel temperature . . . . .	84
4.6.3	The large $V$ state . . . . .	86
4.7	Discussion . . . . .	87
4.7.1	Validity of approximations . . . . .	87
4.7.2	Landau damping in the metallic phase . . . . .	87
4.7.3	Numerical issues . . . . .	89
4.7.4	Comparison with experiments . . . . .	90
4.8	Conclusion . . . . .	90
<b>5</b>	<b>Nonequilibrium magnetic dynamics</b>	<b>93</b>
5.1	Background . . . . .	93

---

5.2	Model and method . . . . .	94
5.2.1	Model . . . . .	94
5.2.2	Equilibrium Heisenberg limit . . . . .	95
5.2.3	Random phase approximation . . . . .	95
5.2.4	Langevin dynamics approach . . . . .	97
5.3	Results from Langevin dynamics . . . . .	98
5.3.1	The equilibrium case . . . . .	98
5.3.2	Effect of voltage bias . . . . .	100
5.4	Discussion . . . . .	101
<b>Appendices</b>		<b>105</b>
<b>A</b>	<b>Appendix A</b>	<b>107</b>
A.1	Justification for choosing collinear moments . . . . .	107
A.2	Perturbative corrections to DOS . . . . .	109
<b>B</b>	<b>Appendix B</b>	<b>111</b>
B.1	High temperature form of $\Pi^K$ . . . . .	111
B.2	Charge fluctuations within the Langevin scheme . . . . .	114
<b>Bibliography</b>		<b>117</b>



# List of Figures

- 1.1 Left: Pressure-temperature phase diagram of  $\kappa - (ET)_2Cu[N(CN)_2]Cl$ , an organic Mott insulator, determined by transport measurements. AF and SC are abbreviations for antiferromagnet and superconductor, respectively. The black dotted line represents the magnetic transition while the solid black line with data points shown in red indicates finite temperature insulator-metal transition, which ends at a critical point around 40K. Right: Conductance  $G(P, T)$  around the critical endpoint in the phase diagram. The light blue shaded area indicates the conductance jump. The red and purple lines represent the critical behavior that gives the critical exponents  $\delta$  and  $\beta$ , corresponding to pressure and temperature driven conductance jumps respectively. Taken from Ref.[30] . . . . . 16
- 1.2 Schematic representation of a pressure induced Mott transition.  $U$  is the on-site Coulomb repulsion, and  $W$  is the bandwidth of the system. At low pressure, where  $U/W > 1$  in the insulating phase, majority of particles (electrons or holes) are localised at lattice sites, even at a finite temperature. For  $U/W < 1$ , at high pressure, the particles can move freely with double occupancies and vacancies allowed in the system. The transition between the two regimes occurs as an insulator-metal transition, without symmetry breaking. Taken from Ref.[30]. . . 17
- 1.3 Schematic representation of linear response theory. The system is at equilibrium for times before  $t_0$ . At  $t_0$  the perturbation  $H'$  is turned on and the system evolves according to the new Hamiltonian  $H_0 + H'$  and remains in a nonequilibrium state. Linear response theory relates the expectation value  $\delta\langle A \rangle_{neq}$  of any operator  $A$  in the nonequilibrium state to a equilibrium expectation value  $\langle \dots \rangle_{eq}$  of the more complicated time-dependent commutator  $[A(t), H'(t')]$  (Ref. [27]). . . . . 18

- 
- 1.4 Nonlinear transport characteristics across different transition metal oxide materials. (a1) Current-voltage (I-V) characteristics and its variation with temperature for a  $5\ \mu\text{m}$  long  $\text{VO}_2$  sample. The equilibrium insulator-metal transition temperature  $T_{\text{IMT}} \sim 340\ \text{K}$ . (a2) Resistance (R) as a function of temperature (T) for different values of bias voltages for the same sample [39]. (b1) Temperature dependent I-V for the ruthenate Mott insulator  $\text{Ca}_3(\text{Ru}_{0.9}\text{Ti}_{0.1})_2\text{O}_7$  of length  $0.15\text{mm}$ .  $T_{\text{IMT}} \sim 114\ \text{K}$  for this material. (b2) The time evolution of sample voltage ( $V_{\text{sample}}$ ) at  $T = 5\ \text{K}$  for the same material. Voltage pulses at fixed time scale  $\sim 800\ \mu\text{s}$  with increasing magnitudes were applied to the sample and load resistance [41]. (c1)-(c2) Temperature dependent I-V for two different types of voltage pulses in magnetite ( $\text{Fe}_3\text{O}_4$ ) of longitudinal size  $\sim 1\ \mu\text{m}$  and  $T_{\text{IMT}} = 108\ \text{K}$  [43]. . . . . 21
- 1.5 Femtosecond pump-probe absorption spectroscopy in undoped cuprates  $\text{Nd}_2\text{CuO}_4$  (NCO) and  $\text{La}_2\text{CuO}_4$  (LCO), taken from Ref.[53]. Panels (a) and (b) show normalized spectra of changes in photoinduced absorption ( $\Delta\text{OD}$ ) for NCO and LCO respectively, for different time delays after excitation. The solid black lines in both the panels show  $\Delta\text{OD}$  for 1% doped NCO and 2% doped LCO respectively, for comparison. (c) Schematic representation of the photoinduced phenomena: [i] ground state of the Mott insulator, [ii] photoinduced metallic states showing the Drude response, [iii] localized carriers showing the midgap absorption, and [iv] heating of the system after photocarrier recombinations. . . 23
- 1.6 Expansion of homogeneously confined interacting fermions. (a) Experimental in situ absorption images for different interactions after 25 ms expansion in a horizontally homogeneous lattice.  $J$  and  $U$  are the hopping and the onsite Coulomb interaction strengths, respectively. The images show a symmetric crossover from a ballistic expansion for non-interacting clouds to an interaction-dominated expansion for both attractive and repulsive interactions. The dynamics is independent of the sign of the interaction, revealing a novel, dynamic symmetry of the Hubbard model. (b) Simulated density distributions using a 2D Boltzmann equation. Taken from Ref. [62] . . . . . 24

1.7	Spin waves in $La_2CuO_4$ . (A) Dispersion relation along high symmetry directions in the 2D Brillouin zone, shown in inset (C), at $T = 10K$ (open symbols) and $295K$ (solid symbols). Solid (dashed) line is a fit to the spin-wave dispersion relation at $T = 10K(295K)$ which is obtained from a Heisenberg model with first-, second-, third-nearest neighbour and ring exchange magnetic couplings. (B) Wavevector dependence of the spin-wave intensity at $T = 295K$ compared with predictions of linear spin-wave theory shown by the solid line. Taken from Ref. [68]. . . . .	26
1.8	DMFT self-consistency (Ref. [121]). . . . .	28
2.1	Schematic diagram showing the setup. The sites having onsite Hubbard repulsion are marked in blue, while the noninteracting bath sites are marked in yellow. The coupling between the system and the bath is denoted by red bonds. The bias is applied symmetrically at the two edges by tuning the chemical potential of the baths. . . . .	36
2.2	The complex time Keldysh contour for accessing steady states. In order to access steady states one can take $t_0$ (initial time) and $t_{max}$ (maximum time) to $\pm\infty$ . In order to calculate observables, e.g. the two-point function, one makes insertions at intermediate times $t_1$ and $t_2$ . . . . .	37
2.3	Implementation of self-consistency for Keldysh mean field theory. . . . .	41
2.4	Flowchart for implementation of the Langevin scheme. $t_{max}$ is the desired run length. . . . .	49
3.1	(a)-(d) Comparing the density of states in the antiferromagnetic state and the ‘paramagnetic’ phase with random moment orientations for $U/t = 2, 4, 6, 8$ respectively. The ordered state remains gapped at all values of $U$ . At $U/t = 2$ , loss of order creates a gapless DOS. At $U/t = 4$ , the ‘paramagnetic’ state is gapless but band singularities are absent. At $U/t = 6$ there is a pseudogap, while $U/t = 8$ shows a clean gap persisting in the ‘paramagnetic’ state. (e) Charge gap $2\Delta$ as a function of $U$ for the Hartree-Fock ground state at equilibrium. (f) Energy difference $E_{mag}$ between the antiferromagnetic ground state and the ‘paramagnetic’ state with random moment orientations, as a function of $U$ . $E_{mag} \sim t^2/U$ at large $U$ . . . . .	58

- 
- 3.2 (a) The I-V characteristics for different values of interaction strength  $U$ , showing the transition from an insulating Mott state to a metallic state. The current rises sharply around a ‘critical bias’  $V_c$ , and finally saturates to a scale  $I_{sat}(U)$  when  $V \gg V_c$ . The dependence of  $I_{sat}$  on the  $U$  is shown in the inset. (b) A map of the current for varying  $U$  and  $V$ . The broken line demarcates the insulator-metal ‘phase boundary’. . . . . 60
- 3.3 (a) Size dependence of I-V characteristics at  $U = 6$ . The current is measured in units of  $et/\hbar$ . Both the critical bias  $V_c$ , as well as the saturation current  $I_{sat}$  depend on the longitudinal size of the system. (b) The region around  $V_c$  has been plotted in log scale to highlight its size dependence. (c) Shows the dependence of  $I_{sat}$  on the longitudinal size. The data can be fitted reasonably to  $I_{sat} \propto 1/L_x$ . For a fixed  $V$  the current, and the ‘metallization’ effect in general, would vanish as  $L_x \rightarrow \infty$ . . . . . 61
- 3.4 Density of states: the upper row shows the variation of local DOS  $A_{ii}(\omega, x)$  along the longitudinal direction,  $(x)$ , with changing bias at  $U = 6t$ . The panels a1-a5 are for  $V = \{0, 3, 5, 6, 12\}$  respectively. The regimes are (a1) the reference AF-I state at  $V = 0$ , (a2) AF-I at low  $V$ , (a3) AF-I to AF-M breakdown, (a4) AF-M at large current, (a5) PM-M state with current saturation. The lower row shows the behavior of the system averaged density of states with changing bias at  $U = 6t$ . Panels b1-b5 are for the same values of  $V$  as the respective panel above. The system size is  $32 \times 8$ . . . . . 63
- 3.5 The auxiliary fields,  $\phi(x, V)$  and  $|M(x, V)|$  as a function of bias for  $U = 6t$ . Panels (a) and (b) show the spatial profile for a few values of  $V$  corresponding to the pre-breakdown regimes in the I-V curve. The open circles denote the data points, while solid lines denote fitted curves for  $\phi$  in (a) and  $|M|$  in (b) using the trial functions. The broken lines in grey denote the zero bias profiles and serve as reference. Panels (c) and (d) show the auxiliary field profiles in the post-breakdown  $V = 5, 6$  and saturation  $V = 12$  regimes. The results shown are for a  $48 \times 8$  system at  $U = 6$ . . . . . 64
- 3.6 The fitting parameters - penetration length  $\xi$  and scale factor  $A$  as a function of bias  $V$ , in the neighbourhood of the voltage driven crossover for  $U = 6$ . The system size is  $48 \times 8$ . . . . . 65

- 
- 3.7 Fourier content of the auxiliary field modulations at  $U = 6t$  plotted for different  $V$ . The upper panels show the Fourier transform of  $\delta\phi(x) = \phi(x) - \phi_{tr}(x)$ , while the lower panels show the Fourier transform of  $\delta M(x) = M(x) - M_{tr}(x)$ . Voltages are  $V = \{3.6, 4.1, 5, 8\}$  from left to right columnwise. As  $V$  increases across the transition, the interval containing the dominant modes shrinks to a narrow interval around  $k_x = 0$  for  $\delta\phi(k_x)$  and  $k_x = \pi$  for  $\delta M(k_x)$  respectively.  $L_x = 48$  for the plot shown. . . . . 66
- 3.8 The perturbatively corrected DOS, in the pre-breakdown regime for different values of  $\xi$  keeping  $A$  fixed at 1.5. The gap reduces with increasing  $\xi$ . . . . . 67
- 3.9 (a1)-(d1)  $\eta$  dependence of bond currents across the system for various voltage ( $V$ ) values.  $\eta$  must be chosen to be much smaller than the average level spacing  $\delta$  ( $\sim 0.02$  for a  $32 \times 8$  system) to avoid gross violation in current conservation across the system. . . . . 69
- 4.1 Equilibrium phase diagram of the 3D Hubbard model in the temperature  $T/t$  vs interaction strength  $U/t$  plane, where  $t$  is the hopping strength. The solid red squares show dependence of the Néel temperature  $T_N$  on  $U/t$ , as obtained from a classical auxiliary field Monte-Carlo method on  $4^3$  clusters. The AF-I region denotes the Néel antiferromagnetic phase and insulating characteristics. The open squares are the  $T_N$  obtained from a DQMC method (Ref.[166]). The light blue region depicts the preformed local moment regime which is a paramagnetic insulator phase. The dashed line shows the  $T_N$  obtained from Hartree-Fock theory and the gray region denotes the paramagnetic metal phase. Taken from Ref.[26] . . . . . 73
- 4.2 Results for equilibrium 3D Hubbard model at  $U/t = 6$ . (a) The variation of the single particle density of states (DOS) with temperature. The charge gap reduces with increasing temperature and crosses over to a pseudogap at  $T = 0.2t$ . (b) The variation of optical conductivity with temperature. A Drude weight appears in the optical spectrum as the system undergoes the pseudogap crossover. (c) Dependence of the logarithm of resistivity on inverse temperature. The data above the pseudogap crossover ( $t/T = 5$ ) fits well with a straight line having slope equal to the zero temperature single particle gap  $\Delta$  and intercept  $\log(\rho_0)$ .  $\Omega$  is the energy cutoff used to calculate the d. c. conductivity (unpublished). . . . . 74

- 
- 4.3 (a) Comparison of temperature dependence of the structure factor peak with equilibrium ‘classical’ Monte carlo. The Néel temperature  $T_N = 0.22t$  at  $U = 6t$ . The two curves coincide, except very close to  $T_N$ . (b) Comparison of moment distribution for different temperatures. The distributions match at low temperature and somewhat deviate near  $T_N$ . . . . . 76
- 4.4 (a) Phase diagram of the voltage biased repulsive Hubbard model at  $U = 6t$ . The AF-I, P-M and P-I are the antiferromagnetic insulator, paramagnetic metal and paramagnetic insulator phases respectively. Insulating regimes have  $\partial I/\partial T > 0$  and the metal has  $\partial I/\partial T < 0$ . CX marks the hysteretic window. The solid blue line indicates  $T_N(V)$ , the dashed white line  $T_{IMT}(V)$  and the broken grey line indicates  $T_{pg}(V)$ . (b) The magnetic ordering peak,  $S(\pi, \pi, \pi)$  as a function of temperature ( $T$ ) for upward (open circles) and downward (solid squares) voltage ( $V$ ) sweeps. Beyond  $T = 0.02t$  the two curves coincide for all values of  $V$ . The inflection point for each curve gives the Néel temperature ( $T_N$ ) for the corresponding  $V$ . . . . . 77
- 4.5 (a-d) Variation of the moment magnitude distribution with temperature ( $T$ ) for  $V/t = 0, 2, 3$  and  $5$  respectively. The solid (dashed) lines denote the distribution for upward (downward) sweeps at different temperatures. . . . . 78
- 4.6 (a) The current-voltage characteristics with changing temperature ( $T$ ) for upward voltage sweeps. The inset shows the hysteretic behaviour at very low  $T$ . The solid lines and open circles correspond to upward voltage sweeps while the dashed lines and filled squares correspond to downward voltage sweeps. At  $T < 0.02t$ , the current changes discontinuously at  $V_c^\pm(T)$  for the upward and downward sweeps, respectively. Beyond the coexistence region the I-V has a unique threshold at  $V_c(T)$  which gets smeared with increasing  $T$  and vanishes for  $T > 0.1t$ . (b) Current ( $I$ ) as a function of temperature ( $T$ ) for different  $V$ .  $\partial I/\partial T > (<) 0$  indicates an insulating (metallic) phase. The peak in the  $I(T, V)$  curve for a fixed  $V$  indicates a temperature driven insulator to metal transition (IMT). (c) Resistance ( $R = V/I$ ) vs  $T$  plotted on a log scale. A minimum in the  $R(T, V)$  curve for a fixed  $V$  indicates insulator to metal crossover. . . . . 79

- 
- 4.7 Top: Map of DOS for varying temperature and voltage, on the upward sweep. For  $V/t \leq 2.2$ , the low  $T$  DOS remains gapped and becomes pseudogapped for  $T > T_{pg}$ , in both the sweep cycles. For  $2.2 < V/t < 3.4$  the DOS remains gapped at low temperature, develops subgap weight with increasing  $T$ , even in the insulating phase, and ultimately becomes pseudogapped at large  $T$ . For the downward sweep, the DOS in this regime retains subgap weight even to the lowest temperature. For  $V/t \geq 3.4$  the DOS remains ungapped at low  $T$ , broadens with increasing  $T$ , and develops a pseudogap at high  $T$ . Bottom: The variation of density of states (DOS) with temperature for  $V/t = 0, 2.2, 3.4$  and  $5$ . . . . . 81
- 4.8 LDOS at an edge site (top row) and at a central site (bottom row) for  $V/t = 0, 2.2, 3.4$  and  $5$  from left to right. The edge sites remain ungapped for all voltages and temperatures due to hybridisation with the leads, while the sites at the center remain (un)gapped in the (metallic) insulating phase. Increasing temperature leads to enhancement of weight at the Fermi level up to the pseudogap temperature  $T_{pg}(V)$ . Beyond  $T_{pg}$  the LDOS broadens and the weight at the Fermi level gradually decreases. . . . . 82
- 4.9 (a1-d1) Variation of the average charge profile, along the longitudinal direction, with increasing temperature for  $V/t = 0, 2, 3.4$  and  $6$ . With sufficient averaging the profile becomes antisymmetric about the center of the system, hence only the left half has been shown. (a2-d2) Variation of the average local moment magnitude along the longitudinal direction. The averaging leads to a symmetric profile across the center of the system. . . . . 83
- 4.10 (a) Effective functional for different values of  $V/t$ . For  $V < V_c^-$  it has a unique minimum at large  $M$ . For  $V_c^- < V \leq V_c^+$  it develops two minima (inset). For  $V > V_c^+$  there is a unique minimum at  $M = 0$ . (b) The resulting moment  $\bar{M}$  at the minimum, which gets a sweep dependence in the coexistence region due to the presence of two minima. The open symbols are actual data points for  $T = 0.001t$ . The lines show the corresponding profile obtained from the effective functional. The red square indicates the point at which the moment profile jumps in the upward sweep according to the effective functional. In the effective description, the large  $V$  moment has been approximated to be zero. . . . . 84

- 
- 4.11 (a) Variation of average moment magnitude  $\langle |M| \rangle$  with temperature ( $T$ ) for different values of bias voltage ( $V$ ). For each  $V$  the corresponding Néel temperature ( $T_N(V)$ ) has been marked with a black cross on the trace.  $\langle |M| \rangle(T)$  develop minima at  $T_*(V)$ . (b) Comparison of the ratios of Néel temperatures at finite  $V$  over that at  $V = 0$  and the corresponding squared average moment magnitudes at  $T_*$ . The comparison suggests that the finite  $V$  magnetic transition can be modeled by an effective Heisenberg model with  $J_{ij}^{eff} = \frac{t^2}{U} |\vec{M}_i| |\vec{M}_j|$ , where the amplitudes must be sampled from the  $P(m; V, T)$  distributions obtained through the full Langevin scheme. (c) Variation of magnetic structure factor peak at  $(\pi, \pi, \pi)$  with temperature for different values of  $V$ . From this, the Néel temperature for the effective Heisenberg model is extracted and compared with that obtained from the full calculation in (d). They show almost exact match at low  $V$ , and significant difference at large  $V$  close to the metallic phase which indicates failure of the effective Heisenberg picture. . . . . 85
- 4.12 Comparison of the approximate current (solid lines) with the exact result (open circles) in the paramagnetic metal phase for  $V/t = 4, 6$ . . . . . 86
- 5.1 Variation of the time-series for the nearest neighbor overlap  $O_{NN}$  across the thermally driven antiferromagnet (AF) to paramagnet (PM) crossover in the 2D Hubbard model. Panels (a)-(d) represent temperatures  $T/t_{hop} = 0.01, 0.1, 0.16$  and  $0.3$  respectively, while the crossover temperature is  $T_c = 0.15t_{hop}$  at  $U/t_{hop} = 6$ . The mean of the time-series at low temperature has a negative value owing to AF correlations, which gradually goes to zero with increasing temperature as the system becomes magnetically disordered.  $\tau_0 = 1/t_{hop}$  is the unit of time. . . 98
- 5.2 (a1)-(a4) Temperature dependence of the auxiliary field dynamical structure factor  $D_{\vec{q}}(\omega)$  at  $U/t_{hop} = 6$ . Panels from left to right correspond to  $T/t_{hop} = 0.001, 0.08, 0.12$  and  $0.18$  respectively. (b1)-(b4) Corresponding plots for the dynamical spin structure factor  $\mathcal{D}_{\vec{q}}(\omega)$ . . . . . 99
- 5.3 Variation in the auxiliary field dynamical structure factor with changing onsite Hubbard interaction strength at  $T/t_{hop} = 0.01$ . The panels correspond to  $U/t_{hop}$  values (a) 6, (b) 8 and (c) 20. . . . . 99
- 5.4 Time-series of the nearest neighbour overlap of the spins  $O_i^{NN}$  at the edge, quarter (half-way between the edge and the center) and the central sites with varying bias  $V/t_{hop}$  values (a) 0, (b) 4, (c) 5 and (d) 6. The Hubbard interaction  $U/t_{hop} = 8$  and the temperature  $T/t_{hop} = 0.01$ . . . . . 100



5.5	Magnon spectrum with increasing bias ( $V$ ) in the driven dissipative 2D Hubbard model at $U/t_{hop} = 8$ and temperature $T/t_{hop} = 0.01$ . Panels (a)-(d) correspond to bias $V/t_{hop} = 0, 4, 5$ and $6$ respectively. The system size is $12 \times 12$ with periodic boundary condition in the transverse direction. . . . .	100
5.6	Variation of lineshapes with bias voltage for $\vec{q} = (\frac{\pi}{2}, 0)$ and $(\frac{\pi}{2}, \frac{\pi}{2})$ at $U/t_{hop} = 8$ and $T/t_{hop} = 0.01$ . The multi-peak features are due to the spatial inhomogeneity in the longitudinal direction due to the presence of leads. It also contributes to the unusual broadening of the peaks along with Gilbert damping and longitudinal relaxation of the local moments. . . . .	101
5.7	Magnon spectrum with increasing bias ( $V$ ) for the effective Heisenberg model. The moment amplitudes are fixed by the $T = 0$ nonequilibrium mean field profiles. Panels (a)-(d) correspond to bias $V/t_{hop} = 0, 4, 5$ and $6$ respectively. The system size is $24 \times 24$ with periodic boundary condition in the transverse direction. . . . .	102
5.8	Variation of lineshapes of the amplitude modulated Heisenberg model at $J = 0.5t_{hop}$ with effective bias voltage ( $V_{eff}$ ) for $\vec{q} = (\frac{\pi}{2}, 0)$ and $(\frac{\pi}{2}, \frac{\pi}{2})$ . The effective voltage enters the model through the parameters $A$ and $\xi$ , which define the approximate amplitude profile of the local moments through Eqs.3.6. . . . .	103
B.1	(Top panel) Time series for local densities at the sites $i = (L_x/4, 0, 0)$ shown in blue and $i = (L_x/2, 0, 0)$ shown in orange, respectively, with changing temperature and voltage. For a fixed voltage $V$ , increasing temperature $T$ leads to an enhancement of charge fluctuations, while for a fixed $T$ the charge fluctuations undergo a nonmonotonic change with increasing $V$ , as the system goes from an insulating to a metallic phase. (Bottom panel) The behaviour of the mean (left panel) and standard deviation (right panel) of the distribution of charge fluctuation at the site $i = (L_x/4, 0, 0)$ is plotted as a function of $V$ for various temperatures $T$ . Both the quantities show nonanalytic features close to the insulator-metal transition for $T < T_{pg}$ . . . . .	115

# SUMMARY

In this thesis we have developed a real space and real time scheme to tackle out of equilibrium strongly correlated problems in a dissipative environment. It exploits the separation of timescales between the ‘fast’ electronic degrees of freedom and the ‘slow’ collective modes. Starting from a Schwinger-Keldysh action we arrive at the effective Langevin equation governing the dynamics of the slow degrees of freedom, by introducing auxiliary fields and making a semiclassical ‘gradient approximation’ in the temporal coordinates. The Keldysh-based Langevin scheme reduces to a nonequilibrium mean-field theory at zero temperature and incorporates non-gaussian thermal fluctuations of the auxiliary fields at finite temperature. Using this, we have studied the nonequilibrium steady state response and magnetic dynamics in the Mott insulator, modeled by the single-band Hubbard model at half-filling, connected to metallic leads at the edges. A voltage bias is imposed by maintaining the leads at different chemical potentials.

We first discuss the inhomogeneous nonequilibrium mean-field theory of the voltage bias driven transition from a Mott insulator to a correlated metal. Within our Keldysh mean-field approach the problem reduces to a self-consistency scheme for the charge and spin profiles in this open system. We solve this problem for a two dimensional antiferromagnetic Mott insulator at zero temperature. The charge and spin magnitude remains uniform over the system at zero bias, but a bias  $V$  leads to spatial modulation over a length scale  $\xi(V)$  near the edges.  $\xi(V)$  grows rapidly and becomes comparable to system size as  $V$  increases towards a threshold scale  $V_c$ . The linear response conductance of the insulator is zero with the current being exponentially small for  $V \ll V_c$ . The current increases rapidly as  $V \rightarrow V_c$ . Beyond  $V_c$ , we observe an inhomogeneous low moment antiferromagnetic metal, and at even larger bias, a current saturated paramagnetic metal. We also observe a strong spatial dependence of the local density of states (LDOS) near the voltage driven transition. We suggest an approximate scheme for the spectral features of this nonequilibrium system.

Next, we use the Langevin dynamics approach to map out the thermal phases of an antiferromagnetic Mott insulator pushed out of equilibrium by a large voltage bias ( $V$ ). The Mott insulator is realised in the half-filled Hubbard model in a three dimensional bar geometry with leads at voltage  $\pm V/2$  connected at the two ends. We decouple the strong Hubbard interaction via the combination of an auxiliary vector field, to capture magnetic fluctuations, and a homo-

---

geneous scalar field to maintain half-filling. The magnetic fluctuations are assumed to be slow on electronic timescales. At low temperature, we find a voltage driven first order transition from a Mott insulator to a correlated metal. The current-voltage characteristics show hysteresis with respect to voltage sweeps, up to a coexistence temperature  $T_{cx}$ , as found in experiments on several transition metal oxides. We find an initially slow and then progressively rapid suppression of the Néel temperature  $T_N$  and pseudogap temperature  $T_{pg}$  with bias, and discover that the bias leads to a finite temperature insulator-metal transition. We explain the thermal results in terms of strong amplitude fluctuation of the local moments in the first order landscape.

Lastly, we discuss the nonequilibrium steady state dynamics of the collective magnon modes in the two dimensional voltage driven half-filled Hubbard model at low temperatures. From the time-series of the auxiliary fields obtained through the Langevin scheme, we calculate the dynamical spin structure factor  $D_{\vec{q}}(\omega)$ , which captures the low energy magnetic excitation spectrum obtained in inelastic neutron scattering (INS) experiments. At low temperatures, for the periodic system at equilibrium, it has a well defined spin-wave dispersion  $\omega(\vec{k})$ , with Goldstone modes at  $\vec{k} = (0, 0)$  and  $(\pi, \pi)$ . For the open system, new low energy features appear due to broken translation invariance along the transport direction. As  $V$  approaches the threshold voltage ( $V_c$ ) for the insulator-metal transition in two dimensions, we find that a new low energy branch develops in the spectrum. This is due to the reduction in amplitude of the moments, governed by the penetration length  $\xi(V)$ . The essential features in  $D_{\vec{q}}(\omega)$  are captured by a classical Heisenberg model with modified moment amplitudes.

# SUMMARY

In this thesis we have developed a real space and real time scheme to tackle out of equilibrium strongly correlated problems in a dissipative environment. It exploits the separation of timescales between the ‘fast’ electronic degrees of freedom and the ‘slow’ collective modes. Starting from a Schwinger-Keldysh action we arrive at the effective Langevin equation governing the dynamics of the slow degrees of freedom, by introducing auxiliary fields and making a semiclassical ‘gradient approximation’ in the temporal coordinates. The Keldysh-based Langevin scheme reduces to a nonequilibrium mean-field theory at zero temperature and incorporates non-gaussian thermal fluctuations of the auxiliary fields at finite temperature. Using this, we have studied the nonequilibrium steady state response and magnetic dynamics in the Mott insulator, modeled by the single-band Hubbard model at half-filling, connected to metallic leads at the edges. A voltage bias is imposed by maintaining the leads at different chemical potentials.

We first discuss the inhomogeneous nonequilibrium mean-field theory of the voltage bias driven transition from a Mott insulator to a correlated metal. Within our Keldysh mean-field approach the problem reduces to a self-consistency scheme for the charge and spin profiles in this open system. We solve this problem for a two dimensional antiferromagnetic Mott insulator at zero temperature. The charge and spin magnitude remains uniform over the system at zero bias, but a bias  $V$  leads to spatial modulation over a length scale  $\xi(V)$  near the edges.  $\xi(V)$  grows rapidly and becomes comparable to system size as  $V$  increases towards a threshold scale  $V_c$ . The linear response conductance of the insulator is zero with the current being exponentially small for  $V \ll V_c$ . The current increases rapidly as  $V \rightarrow V_c$ . Beyond  $V_c$ , we observe an inhomogeneous low moment antiferromagnetic metal, and at even larger bias, a current saturated paramagnetic metal. We also observe a strong spatial dependence of the local density of states (LDOS) near the voltage driven transition. We suggest an approximate scheme for the spectral features of this nonequilibrium system.

Next, we use the Langevin dynamics approach to map out the thermal phases of an antiferromagnetic Mott insulator pushed out of equilibrium by a large voltage bias ( $V$ ). The Mott insulator is realised in the half-filled Hubbard model in a three dimensional bar geometry with leads at voltage  $\pm V/2$  connected at the two ends. We decouple the strong Hubbard interaction via the combination of an auxiliary vector field, to capture magnetic fluctuations, and a homo-

---

geneous scalar field to maintain half-filling. The magnetic fluctuations are assumed to be slow on electronic timescales. At low temperature, we find a voltage driven first order transition from a Mott insulator to a correlated metal. The current-voltage characteristics show hysteresis with respect to voltage sweeps, up to a coexistence temperature  $T_{cx}$ , as found in experiments on several transition metal oxides. We find an initially slow and then progressively rapid suppression of the Néel temperature  $T_N$  and pseudogap temperature  $T_{pg}$  with bias, and discover that the bias leads to a finite temperature insulator-metal transition. We explain the thermal results in terms of strong amplitude fluctuation of the local moments in the first order landscape.

Lastly, we discuss the nonequilibrium steady state dynamics of the collective magnon modes in the two dimensional voltage driven half-filled Hubbard model at low temperatures. From the time-series of the auxiliary fields obtained through the Langevin scheme, we calculate the dynamical spin structure factor  $D_{\vec{q}}(\omega)$ , which captures the low energy magnetic excitation spectrum obtained in inelastic neutron scattering (INS) experiments. At low temperatures, for the periodic system at equilibrium, it has a well defined spin-wave dispersion  $\omega(\vec{k})$ , with Goldstone modes at  $\vec{k} = (0, 0)$  and  $(\pi, \pi)$ . For the open system, new low energy features appear due to broken translation invariance along the transport direction. As  $V$  approaches the threshold voltage ( $V_c$ ) for the insulator-metal transition in two dimensions, we find that a new low energy branch develops in the spectrum. This is due to the reduction in amplitude of the moments, governed by the penetration length  $\xi(V)$ . The essential features in  $D_{\vec{q}}(\omega)$  are captured by a classical Heisenberg model with modified moment amplitudes.

# Introduction

## 1.1 Overview

A confluence of ideas between quantum mechanics and statistical mechanics gave rise to modern condensed matter theory. The correspondence between Euclidean quantum field theory and quantum statistical mechanics led to development of finite temperature quantum many body theory [1]. It led to a better understanding of the low temperature properties of metals via Fermi liquid theory [2] and also provided an approach to various symmetry broken phases[3, 4] like superconductors, magnets, charge density waves, etc. The developments in theory were supplemented by emergence of a number of experimental techniques including electric and thermal transport, neutron, electron, Raman, and X-ray scattering, calorimetric measurements, scanning tunneling microscopy and many more [5].

A crucial concept relating theoretical approaches to experiments is “linear response theory” which hinges on two principles: (i) proportionality of the response to the drive for sufficiently weak perturbations, and (ii) the fluctuation-dissipation theorem [6, 7]. The former allows for characterization of a system’s response to weak external perturbation in terms of *response functions* which are independent of the strength of perturbation and depend only on the equilibrium state. The latter relates response functions to the thermodynamic *fluctuations* in the equilibrium state. The combination of the two has been an indispensable tool in interpreting experimental data and comparing it to theory.

Modern experiments, however, have pushed the frontier to a domain where linear response theory is no longer applicable. Technology driven miniaturization has contributed to this. As sample sizes have shrunk by orders of magnitude, the effective field inside them has grown correspondingly, driving the systems strongly out of the linear response regime. Simultaneously, developments in ultracold atoms and ultrafast lasers has given access to time-dependent phenomena like thermalisation after a quench, and periodic driving, with unprecedented experimental control. This has led to the discovery of rich and novel paradigms like non-thermal fixed points

---

[8], self-organized criticality [9] and hidden metastable phases [10–15], that inherently exist out of equilibrium.

The approach to nonlinear transport in classical systems is based on Boltzmann kinetic theory which connects the dynamics to thermodynamics. It can be generalized to a semiclassical theory to study transport in semiconductors by invoking the Fermi golden rule. However, it was realised that the correct kinetic equation for most quantum systems could not be deduced simply from the golden rule but had to be *derived* from more general considerations. This led to the development of quantum kinetic theory which incorporated the effect of interactions within a perturbative framework and, in practical applications, assumed the presence of quasiparticles along with some sort of linearization scheme close to equilibrium. This approach has been remarkably successful in numerous systems [16–18].

However, strongly correlated systems, like the Mott insulator, which do not have well defined quasiparticles, have been difficult to fit within this framework. The few attempts at applying the kinetic theory ideas to Mott systems have highlighted the importance of starting from a more general framework [19, 20]. The Schwinger-Keldysh approach (abbreviated simply as the Keldysh approach) offers a framework suited for describing generic nonequilibrium quantum systems. Even though it was introduced nearly sixty years ago by Schwinger [21], and subsequently developed by Kadanoff and Baym [22] while being independently pursued by Keldysh [23], it has gained prominence mainly in the last couple of decades. However, nonperturbative numerical techniques within this framework are still at a nascent stage.

Mott insulators are materials which cannot be described by the conventional band theory of solids. A combination of strong local repulsion and commensurate filling inhibits electron tunneling, leading to localization of electrons. The Mott physics related to suppression of ‘double occupancy’ plays a crucial role in many families of transition metal compounds like the cuprates, ruthenates, iridates and nickelates. The problem of nonequilibrium transport in Mott insulators has been an active field of research, but there are outstanding problems. The temperature dependent transport characteristics of Mott insulators is one of the unsettled issues between theory and experiments.

On the theoretical front, dynamical mean field theory (DMFT) [98] and its variants, which focus on local quantum fluctuations, have been successful in capturing equilibrium ‘Mott physics’. Combined with *ab-initio* methods, they have been used for modeling real materials. A complementary approach that emphasises spatial thermal fluctuations rather than quantum fluctuations is the *static* auxiliary field based Monte-Carlo. It has been successfully applied to several interesting problems [24–26]. Recently, a nonequilibrium generalization of DMFT [104] has been developed. Though it has successfully captured several out of equilibrium phenomena, it performs poorly with respect to experiments in capturing long time steady state transport in *inhomogeneous* Mott systems. Furthermore, the effect of strong electronic driving on the magnetism in these systems remains relatively unexplored.

In this thesis, we have developed a nonperturbative scheme for handling nonequilibrium

transport and dynamics of strongly correlated systems and applied it to the problem of long time steady state transport in Mott insulators driven by a strong bias voltage. Based on the Schwinger-Keldysh framework, it relies on the *separation of timescales* between the fermionic degrees of freedom and the bosonic collective modes.

In this Chapter we briefly discuss the equilibrium physics of Mott insulators, the Hubbard model realisation of the Mott state, linear response theory, and the experimental and theory situation on nonequilibrium studies in Mott systems. In Chapter 2, we discuss our models and methods for handling the driven Mott state. Chapter 3 discusses a mean field approach for transport in the nonequilibrium zero temperature state, while Chapter 4 presents a Langevin equation formulation of the driven Mott state at the finite temperature. Chapter presents results on the collective magnetic excitations in the voltage biased Mott insulator.

## 1.2 The physics at equilibrium

### 1.2.1 Mott insulators

Mott insulators are a class of materials that, according to conventional band theory, should conduct electricity but are in fact insulators. This happens due to electron–electron interactions whose effects are not considered in conventional band theory. A material is called insulating if its dc electrical conductivity ( $\sigma$ ) approaches zero as the temperature is lowered, i.e.,  $\lim_{T \rightarrow 0} \sigma(T) = 0$ . If the conductivity remains finite or diverges at a finite temperature the system is considered metallic or superconducting respectively.

Band theory provides an independent electron description of the ground state: for  $N$  electrons the lowest lying  $N/2$  states are filled with two electrons each. In the independent-electron picture, the system is predicted to be metallic if the density of states at the Fermi level is non-vanishing:  $\rho(\epsilon_F) \neq 0$ . If  $\rho(\epsilon_F) = 0$  the system must be an insulator, at least for translation invariant systems. Band theory asserts it is necessary to have an even number of electrons per unit cell for  $\rho(\epsilon_F) = 0$ , since a band with orbital degeneracy  $n$  can hold  $2n$  electrons per unit cell. On the other hand, with an odd number of electrons per unit cell we necessarily have a partially filled band, hence  $\rho(\epsilon) \neq 0$ , and consequently the material must be a metal. This basic prediction of band theory fails spectacularly for transition metal oxides in which the valence orbitals are  $d$  or  $f$  orbitals. Hence valence electrons are much more localized in these systems. This leads to a strong energy penalty for placing two electrons in the same local valence orbital, and the motion of valence electrons becomes strongly correlated on the lattice. Building on the ideas of Wigner [28], Mott gave the famous *Mott criterion* for insulator to metal transition based on the competition between the Debye screening length and the Bohr radius and applied these ideas to study transition metals [29]. Later, organic compounds, like the  $\kappa - (ET)_2X$  [30] and  $\kappa$ -BEDT[31] families, were discovered to be Mott insulators on frustrated lattices. The left panel in Fig.1.1 shows the phase diagram and a material in the  $\kappa - (ET)_2X$  family. The insulating



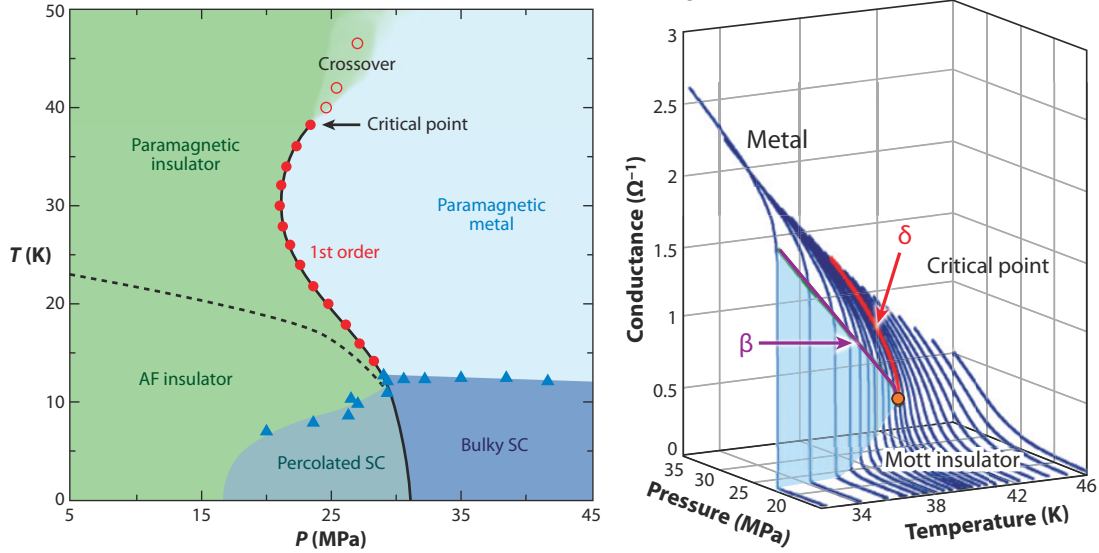


Figure 1.1: Left: Pressure-temperature phase diagram of  $\kappa - (ET)_2Cu[N(CN)_2]Cl$ , an organic Mott insulator, determined by transport measurements. AF and SC are abbreviations for antiferromagnet and superconductor, respectively. The black dotted line represents the magnetic transition while the solid black line with data points shown in red indicates finite temperature insulator-metal transition, which ends at a critical point around  $40K$ . Right: Conductance  $G(P, T)$  around the critical endpoint in the phase diagram. The light blue shaded area indicates the conductance jump. The red and purple lines represent the critical behavior that gives the critical exponents  $\delta$  and  $\beta$ , corresponding to pressure and temperature driven conductance jumps respectively. Taken from Ref.[30]

phase is stable at low pressure and undergoes a magnetic transition from an antiferromagnet to a paramagnet with increasing temperature. At low temperatures one finds a transition to a superconducting state with increasing pressure. It is a well known that superconductivity lurks in the vicinity of the antiferromagnetic insulating phase and a transition can be induced by doping, as in cuprates, or by applying pressure. Above the superconducting phase, we have a pressure driven insulator-metal transition at finite temperature, indicated by a first order line truncating at a critical point around  $40K$ . Apart from the details, the generic structure and phases mentioned in the phase diagram is ubiquitous across Mott insulators. The right panel in Fig.1.1 shows conductance as a function of pressure and temperature, which characterises the nature of the insulator-metal transition.

## 1.2.2 The Hubbard model

The first model based theory was proposed by Hubbard. Considering just one valence orbital he introduced a model, now named after him [32, 33], with a kinetic energy term and a local Coulomb repulsion.

$$\mathcal{H} = -t \sum_{\substack{\langle ij \rangle \\ \sigma \in \uparrow, \downarrow}} c_{i\sigma}^\dagger c_{j\sigma} + h.c. + U \sum_i n_{i\uparrow} n_{i\downarrow} \quad (1.1)$$

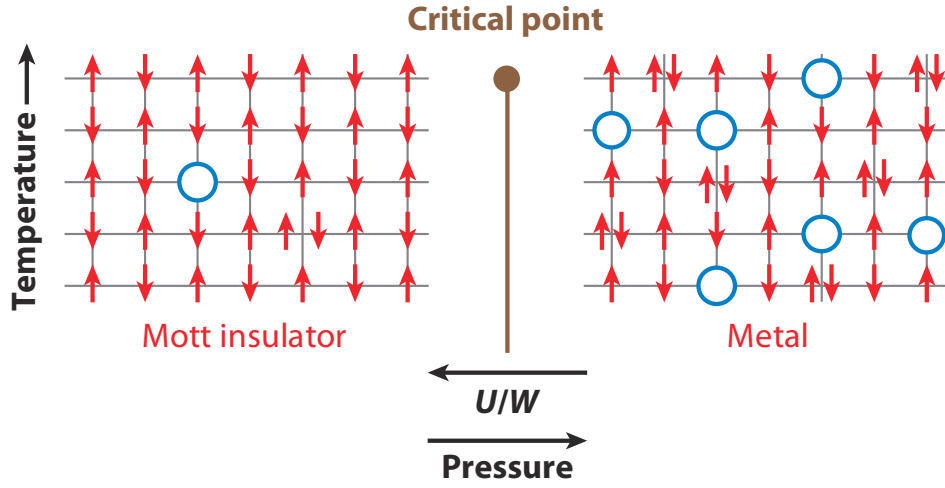


Figure 1.2: Schematic representation of a pressure induced Mott transition.  $U$  is the on-site Coulomb repulsion, and  $W$  is the bandwidth of the system. At low pressure, where  $U/W > 1$  in the insulating phase, majority of particles (electrons or holes) are localised at lattice sites, even at a finite temperature. For  $U/W < 1$ , at high pressure, the particles can move freely with double occupancies and vacancies allowed in the system. The transition between the two regimes occurs as an insulator-metal transition, without symmetry breaking. Taken from Ref.[30].

where  $n_{i\sigma} = c_{i\sigma}^\dagger c_{i\sigma}$ ,  $t$  is the nearest neighbour hopping which promotes delocalisation of the electrons, and  $U$  is the onsite Coulomb repulsion which penalizes double occupancy. The operators  $c_{i\sigma}$  and  $c_{i\sigma}^\dagger$  are the annihilation and creation operators which satisfy the canonical anticommutation relations.

$$\{c_{i\sigma}, c_{j\sigma'}\} = \{c_{i\sigma}^\dagger, c_{j\sigma'}^\dagger\} = 0 \quad (1.2)$$

$$\{c_{i\sigma}, c_{j\sigma'}^\dagger\} = \delta_{ij}\delta_{\sigma\sigma'} \quad (1.3)$$

The limitations of this model, i.e., omission of longer-range interaction, neglect of multiple bands, need to be reevaluated when applied to real materials. However it turns out that even this seemingly simple model describes very rich physics that is far from completely understood. An exact solution for this model at arbitrary filling beyond 1D systems has not been found. Nevertheless a lot of theoretical machinery has been developed and the behaviour is reasonably understood in the half-filled limit.

Quite generally, when the Coulomb scale becomes larger than the kinetic energy significant deviations from band behaviour are expected. A schematic representation of the Mott transition is shown in Fig.1.2. It shows the transition from an insulating phase where particles are localised on lattice sites and double occupancies (along with vacancies) are energetically disfavoured, to a metallic phase, where particles can get delocalized as double occupancies are allowed. The transition doesn't break any symmetry. The barring of double occupancy can also be interpreted in terms of formation of a local moment[34]. From the above arguments, we conclude that strong electron correlation promotes formation of local moments.

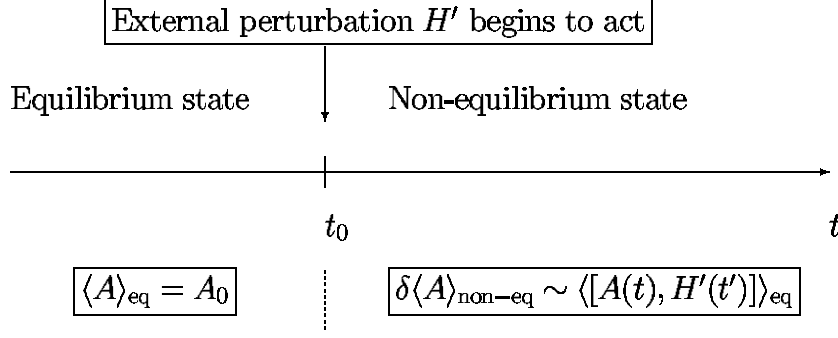


Figure 1.3: Schematic representation of linear response theory. The system is at equilibrium for times before  $t_0$ . At  $t_0$  the perturbation  $H'$  is turned on and the system evolves according to the new Hamiltonian  $H_0 + H'$  and remains in a nonequilibrium state. Linear response theory relates the expectation value  $\delta \langle A \rangle_{\text{neq}}$  of any operator  $A$  in the nonequilibrium state to a equilibrium expectation value  $\langle \cdots \rangle_{\text{eq}}$  of the more complicated time-dependent commutator  $[A(t), H'(t')]$  (Ref. [27]).

Apart from the insulating character, which is due to the presence of large local moments, a Mott insulator generally hosts some kind of magnetic ordering of the moments at low temperatures. In bipartite lattices a Néel antiferromagnetic order is most prevalent, while frustrated lattices can host various other kinds of magnetic textures. The antiferromagnetic state can easily be motivated from the half-filled Hubbard dimer, by realising that it leads to a gain in magnetic exchange energy  $J \sim \frac{t^2}{U}$  through virtual hopping, which is not possible for a ferromagnetic alignment of the local moments[34]. With increasing temperature  $T$ , the antiferromagnetic Mott insulator undergoes a magnetic transition to a paramagnetic Mott insulator as  $T \sim J$ .

### 1.2.3 Linear response theory

Linear response theory (LRT) deals with the scenario where an equilibrium system is weakly perturbed out of equilibrium. It hinges on the fact that in case of weak external perturbation the response of the system can be approximated very well by the terms linear in the perturbation. This is called the linear response (LR) regime, and though the system is in a non-equilibrium state all its characteristics can be inferred from the properties of its equilibrium state (Fig.1.3). Consider an equilibrium system described by the time independent Hamiltonian  $H_0$ . The expectation value of an operator  $A$  is given by:

$$\langle A \rangle = \frac{1}{Z_0} \text{Tr} [\rho_0 A] = \frac{1}{Z_0} \sum_n \langle n^0 | A | n^0 \rangle e^{-\beta E_n} \quad (1.4a)$$

$$\rho_0 = e^{-\beta H_0} = \sum_n |n^0\rangle \langle n^0| e^{-\beta E_n} \quad (1.4b)$$

where  $\rho_0$  is the equilibrium density operator,  $Z_0 = \text{Tr} [\rho_0]$  is the equilibrium partition function and  $\beta$  is the inverse temperature.  $\{|n^0\rangle\}$  represents a complete set of eigenstates of the Hamiltonian  $H_0$ , with eigenvalues  $E_n$ . Suppose now that at some time  $t_0$ , an external perturbation is applied to the system, driving it out of equilibrium. The perturbation is described by an additional time dependent term in the Hamiltonian:

$$H(t) = H_0 + H'(t)\Theta(t - t_0) \quad (1.5)$$

In order to find the expectation value of the operator  $A$  for  $t > t_0$  we must find the time evolution of the eigenstates of the unperturbed Hamiltonian  $|n(t)\rangle$ . From this we can infer  $\langle A(t) \rangle$  as:

$$\langle A(t) \rangle = \frac{1}{Z_0} \text{Tr} [\rho(t)A] = \frac{1}{Z_0} \sum_n \langle n(t)|A|n(t) \rangle e^{-\beta E_n} \quad (1.6a)$$

$$\rho(t) = \sum_n |n(t)\rangle \langle n(t)| e^{-\beta E_n} \quad (1.6b)$$

The crucial assumption here is that although the states evolve with a modified Hamiltonian after the perturbation is switched on, the distribution of states (which are now time dependent) is governed by the same Boltzmann distribution  $\frac{e^{-\beta E_n}}{Z_0}$  as the equilibrium states. The time dependence of the states  $|n(t)\rangle$  in the interaction representation is given by

$$|n(t)\rangle = e^{-iH_0 t} U(t, t_0) |n(t_0)\rangle \quad (1.7)$$

where  $|n(t_0)\rangle \equiv |n^0\rangle$ . To linear order in  $H'$ , we have  $U(t, t_0) = 1 - i \int_{t_0}^t dt' H'(t')$ . Inserting this in Eq. 1.6a, one obtains the expectation value of the operator  $A$  to linear order in the perturbation

$$\langle A(t) \rangle = \langle A \rangle_0 - i \int_{t_0}^t dt' \sum_n \frac{e^{-\beta E_n}}{Z_0} \langle n(t_0) | A(t) H'(t') - H'(t') A(t) | n(t_0) \rangle \quad (1.8a)$$

$$= \langle A \rangle_0 - i \int_{t_0}^t dt' \langle [A(t), H'(t')] \rangle_0 \quad (1.8b)$$

where  $\langle \dots \rangle_0$  denotes equilibrium average with respect to the Hamiltonian  $H_0$ .  $A(t)$  and  $H'(t')$  are operators in the interaction representation. The above equation relates an inherently nonequilibrium quantity  $\langle A(t) \rangle$  to a correlation function of the system at equilibrium. It can be rewritten as

$$\delta \langle A(t) \rangle \equiv \langle A(t) \rangle - \langle A \rangle_0 = \int_{t_0}^{\infty} dt' \chi_{AH'}(t, t') e^{-\eta(t-t')} \quad (1.8c)$$

where

$$\chi_{AH'}(t, t') = -i\theta(t - t') \langle [A(t), H'(t')] \rangle_0 \quad (1.8d)$$

is the retarded response function. The infinitesimal positive parameter  $\eta$  forces the response at time  $t$  due to the influence of  $H'$  at time  $t'$  to decay when  $t \gg t'$ . In the end of a calculation we

must therefore take the limit  $\eta \rightarrow 0^+$ . We are interested in the case where  $H'(t) = \lambda(t)A$ , as most experiments measure the correlation function  $\langle A(t)A(t') \rangle$ . Here  $\lambda$  must be a small parameter for LRT to be applicable. From the Lehmann representation we can show

$$\begin{aligned}\langle A(t)A(t') \rangle &= \sum_{m,n} e^{-\beta E_m} \langle m|A(t)|n \rangle \langle n|A(t')|m \rangle \\ &= \sum_{m,n} e^{-\beta E_m} |\langle m|A|n \rangle|^2 e^{-i(E_n - E_m)(t - t')} \end{aligned} \quad (1.9a)$$

Defining  $t_r \equiv t - t'$  and taking a Fourier transform gives

$$K(\omega) \equiv \int_{-\infty}^{\infty} dt_r \langle A(t)A(t') \rangle e^{i\omega t_r} = \sum_{m,n} e^{-\beta E_m} |\langle m|A|n \rangle|^2 2\pi \delta(\omega - (E_m - E_n)) \quad (1.9b)$$

Similarly, we can expand the retarded response function using the Lehmann representation to obtain

$$\chi_{AA}(t_r) = -i\theta(t - t') \langle [A(t), A(t')] \rangle_0 \quad (1.9c)$$

$$= -i \sum_{m,n} (e^{-\beta E_m} - e^{-\beta E_n}) |\langle m|A|n \rangle|^2 e^{-i(E_m - E_n)(t - t')} \theta(t - t') \quad (1.9d)$$

Taking a Fourier transform gives us,

$$\text{Im} [\chi_{AA}(\omega)] = \pi (1 - e^{-\beta\hbar\omega}) \sum_{m,n} e^{-\beta E_n} |\langle m|A|n \rangle|^2 \delta(\omega - (E_m - E_n)) \quad (1.9e)$$

Comparing Eq. 1.9b and 1.9e we arrive at the relation (restoring  $\hbar$ )

$$K(\omega) = \frac{2\hbar}{1 - e^{-\beta\hbar\omega}} \text{Im} [\chi_{AA}(\omega)] = 2\hbar (1 + n_B(\hbar\omega)) \text{Im} [\chi_{AA}(\omega)] \quad (1.10)$$

which is the quantum fluctuation-dissipation theorem that relates the correlation function with the dissipative part of the retarded response function  $\chi_{AA}(\omega)$ .  $n_B(\omega) \equiv \frac{1}{e^{\beta\hbar\omega} - 1}$  is the Bose distribution function.

LRT has been an indispensable tool for classifying different equilibrium phases, based on their response to weak perturbation, into metals, insulators, superconductors, etc. By construction, the results within LRT remain independent of the strength of external force. The central theme of the thesis is to deal with scenarios where LRT becomes ineffective in predicting the response of a system to a *strong* perturbation. In such a scenario the state of the system might get completely reorganised depending on the strength of perturbation, as we shall find out later.

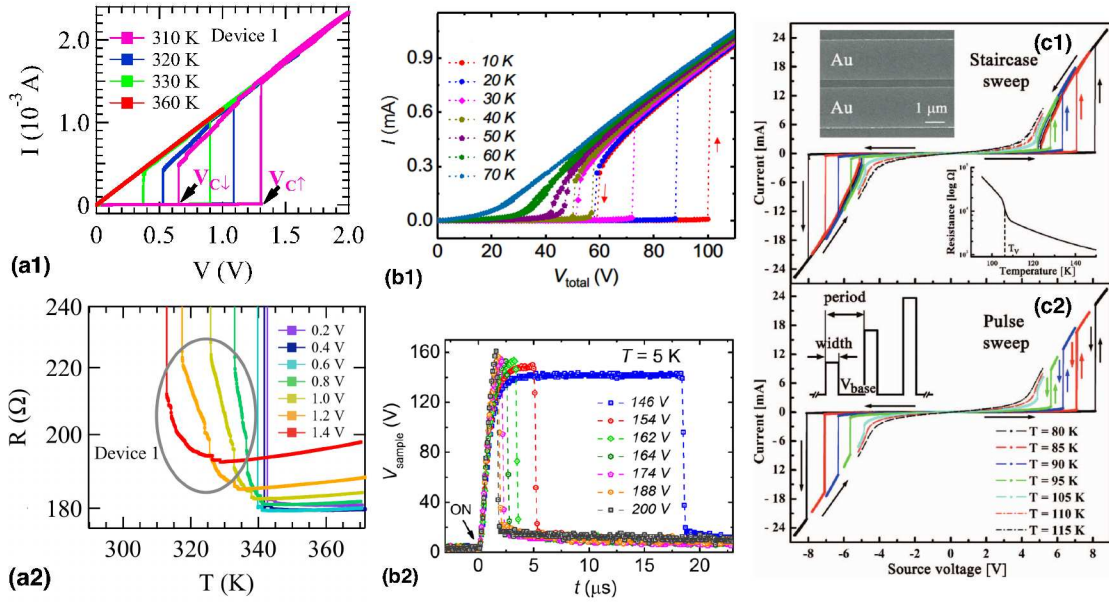


Figure 1.4: Nonlinear transport characteristics across different transition metal oxide materials. (a1) Current-voltage (I-V) characteristics and its variation with temperature for a  $5\ \mu\text{m}$  long  $\text{VO}_2$  sample. The equilibrium insulator-metal transition temperature  $T_{\text{IMT}} \sim 340\ \text{K}$ . (a2) Resistance ( $R$ ) as a function of temperature ( $T$ ) for different values of bias voltages for the same sample [39]. (b1) Temperature dependent I-V for the ruthenate Mott insulator  $\text{Ca}_3(\text{Ru}_{0.9}\text{Ti}_{0.1})_2\text{O}_7$  of length  $0.15\text{mm}$ .  $T_{\text{IMT}} \sim 114\ \text{K}$  for this material. (b2) The time evolution of sample voltage ( $V_{\text{sample}}$ ) at  $T = 5\ \text{K}$  for the same material. Voltage pulses at fixed time scale  $\sim 800\ \mu\text{s}$  with increasing magnitudes were applied to the sample and load resistance [41]. (c1)-(c2) Temperature dependent I-V for two different types of voltage pulses in magnetite ( $\text{Fe}_3\text{O}_4$ ) of longitudinal size  $\sim 1\ \mu\text{m}$  and  $T_{\text{IMT}} = 108\ \text{K}$  [43].

## 1.3 Nonequilibrium experimental probes

While much of the inspiration for the work in this thesis grew from existing experiments, we also make certain predictions which need to be tested in future. Hence, we give a brief review of experiments that are directly or conceptually connected to the topics addressed in this work.

### 1.3.1 Transport measurements

Metal-insulator transitions are accompanied by huge changes, often orders of magnitude, in resistivity [35]. Examples include high- $T_c$  cuprates, transition metal dichalcogenides, rare earth and transition metal oxides. Most insulator metal transitions in Mott insulators, which have been rigorously studied experimentally over the years, were inferred through transport experiments. Majority of these experiments have probed the system well within the linear response regime.

With the advent of better fabrication and characterisation techniques experiments have achieved miniaturisation of samples, as well as better control. This has led to a proliferation of nonlinear transport measurements in recent times. They reveal a host of new phenomena like voltage driven resistive switching, hysteresis, nonequilibrium structural transition [36], switching



---

to a hidden state [11] and pattern formation [37].

Of particular interest are the experiments on transition metal oxide (TMO) Mott insulators, e.g., vanadium oxides [38, 39], ruthenates [40, 41] and iron oxides [42, 43]. Many of these compounds undergo thermally driven insulator metal transition (IMT) at some temperature  $T_{IMT}$  in equilibrium, often with accompanying change in structure. However, at temperatures much below  $T_{IMT}$  these can be driven into a metallic phase by applying a large voltage across the sample. The nonlinear current-voltage (I-V) characteristics for these materials have been obtained from two terminal and four terminal measurements. Fig.1.4 shows the temperature dependent I-V and other transport characteristics for three different materials. These and a host of other experiments reveal some generic features in the I-V:

- A low temperature hysteresis in the current with respect to voltage sweep - changing abruptly from low current to high current at some voltage  $V_{c+}$  on the upward sweep, and showing the reverse switching at  $V_{c-} < V_{c+}$  on the downward sweep, and
- Reduction of  $V_{c\pm}$  and also  $\Delta V_c = V_{c+} - V_{c-}$  with increasing temperature, with hysteresis vanishing above some temperature  $T^*$ .

These features have been observed in samples of nanometer [42] to millimeter [41] size.

Apart from the I-V character, several other remarkable effects have emerged in transport experiments due to the presence of a large bias. Experiments on 1D organic Mott insulators[37], as well as on ruthenates[44], have shown the emergence of wave-like patterns with increasing voltage. Another experiment on a ruthenate material has found suppression of magnetic transition temperature with increasing bias[48].

### 1.3.2 Pump-probe spectroscopy

Pump-probe spectroscopy is an experimental technique used to study ultrafast electronic dynamics. In this technique, an ultrashort laser pulse is split into two portions; a stronger pump beam is used to excite the sample, generating a non-equilibrium state, and a weaker probe beam is used to monitor the pump-induced changes in the sample by optical spectroscopy [53] or photoemission [54]. Recording these changes as a function of time delay between the arrival of pump and probe pulses yields information about the relaxation of electronic states in the sample.

In Mott insulators, a pump pulse with energy larger than the Mott-Hubbard gap creates charged excitations of doublons (doubly occupied sites) and holons (unoccupied sites). In optical spectroscopy experiments, these excitations lead to a Drude-like low frequency response at femtosecond (fs) timescales, as shown in Fig.1.5. The dissipationless Drude component, corresponding to the coherent motion of charges, indicates a transient photoinduced insulator to metal transition, which quickly relaxes through recombination processes and, at later times, by transferring energy to other degrees of freedom. The Drude peak vanishes within a few

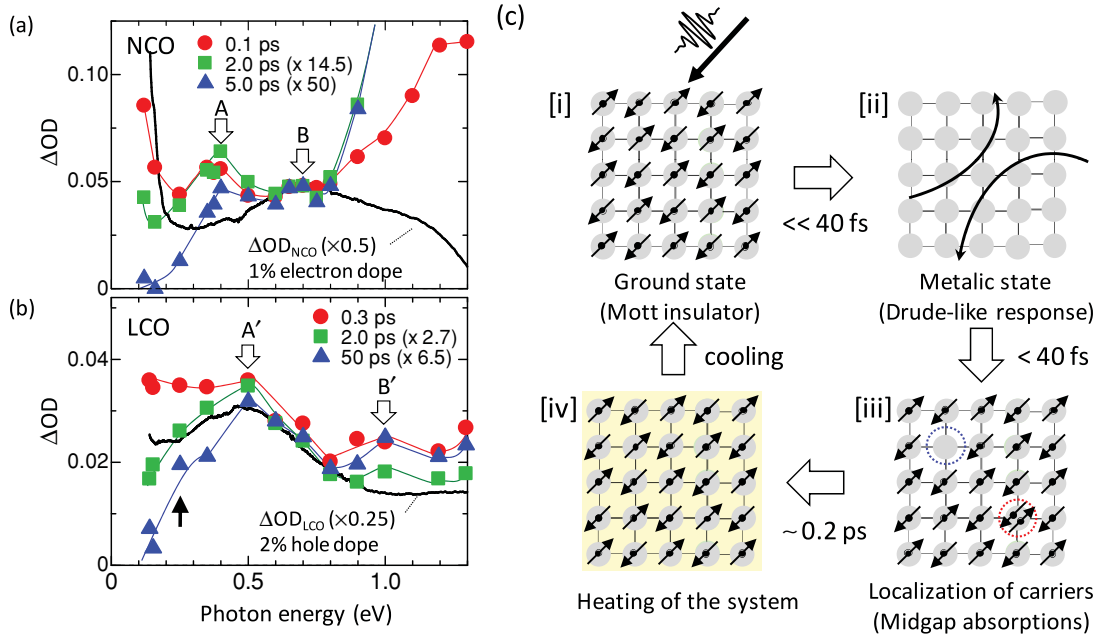


Figure 1.5: Femtosecond pump-probe absorption spectroscopy in undoped cuprates  $Nd_2CuO_4$  (NCO) and  $La_2CuO_4$  (LCO), taken from Ref.[53]. Panels (a) and (b) show normalized spectra of changes in photoinduced absorption ( $\Delta OD$ ) for NCO and LCO respectively, for different time delays after excitation. The solid black lines in both the panels show  $\Delta OD$  for 1% doped NCO and 2% doped LCO respectively, for comparison. (c) Schematic representation of the photoinduced phenomena: [i] ground state of the Mott insulator, [ii] photoinduced metallic states showing the Drude response, [iii] localized carriers showing the midgap absorption, and [iv] heating of the system after photocarrier recombinations.

femtoseconds after excitation and the relaxation processes show up as ‘in-gap’ features in the time evolution of the optical spectrum.

Time-resolved magneto-optic measurements, like magneto-optical Kerr rotation (MOKE), have also revealed ultrafast switching of magnetic order after photoexcitation in strongly correlated systems [58]. On the other hand, time-resolved photoemission spectroscopy (trPES) [59] and angle-resolved PES (trARPES) [60] have been used to study the time evolution of the single-particle spectrum and the band structure, respectively, of correlated materials after excitation by a pump beam. These experiments have led to a new paradigm in which the coupling between various degrees of freedom can be probed by measuring the relaxation timescales after excitation. Each of these timescales are typically associated with particular kind of processes, and hence, the relaxation mechanisms allow us to identify, within a single experiment, the dominant interactions present in a material.

### 1.3.3 Ultracold atomic gases

Unlike real materials, where all kinds of interactions are simultaneously present, ultracold atoms allow us to *design* systems which can simulate specific Hamiltonians and manipulate their coupling strengths, with unprecedented control, via Feshbach resonances [61]. These also allow



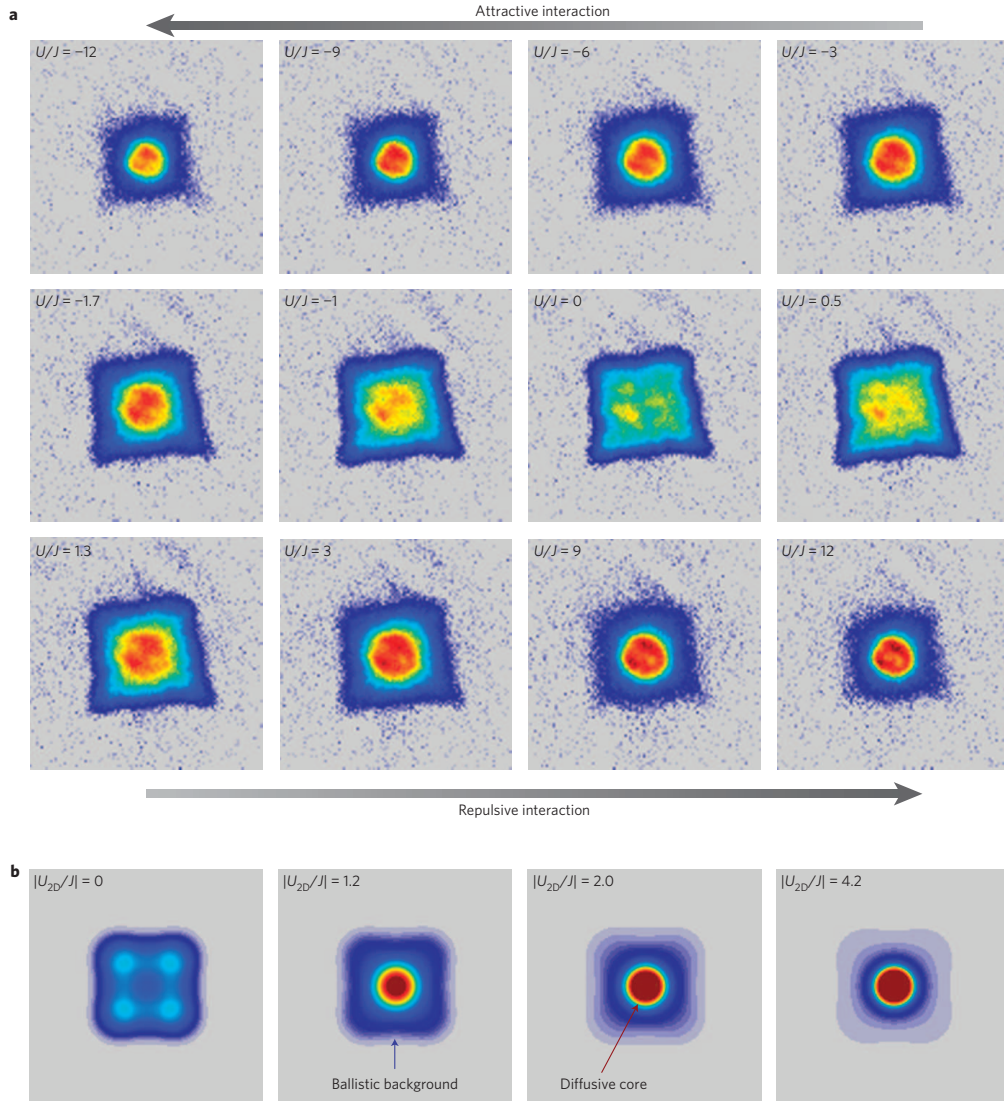


Figure 1.6: Expansion of homogeneously confined interacting fermions. (a) Experimental in situ absorption images for different interactions after 25 ms expansion in a horizontally homogeneous lattice.  $J$  and  $U$  are the hopping and the onsite Coulomb interaction strengths, respectively. The images show a symmetric crossover from a ballistic expansion for non-interacting clouds to an interaction-dominated expansion for both attractive and repulsive interactions. The dynamics is independent of the sign of the interaction, revealing a novel, dynamic symmetry of the Hubbard model. (b) Simulated density distributions using a 2D Boltzmann equation. Taken from Ref. [62]

for the cleanest realization of closed system dynamics in which quantum states with coherence longer than the typical timescales of the dynamics can be prepared.

In the cold atomic systems, the dynamics has longer timescales than in solid-state materials and therefore it can be followed without ultrafast probes. The dynamics of ultracold gases can be imaged either directly in the confining trapping potential, to access the density distribution  $n(\vec{x})$  in position space, or after they are released, during a time-of-flight expansion measuring the momentum distribution  $n(\vec{k})$ . Fig. 1.6 shows the momentum distribution snapshots for expansion

of an interacting cloud after  $25ms$  for different values of the onsite Hubbard interaction. Since the momentum distribution does not depend on the sign of  $U$ , this reveals a ‘dynamical symmetry’ between the  $+U$  and the  $-U$  Hubbard models [62].

Several other interesting problems have also been studied within the ultracold atoms setup, like the slow decay of artificially excited doublons into particle-hole pairs [63, 64], doublon production due to an interaction quench [18], and periodic modulation of lattice depth to excite to excite doublons whose production rate is sensitive to nearest neighbour density and spin correlator [65].

### 1.3.4 Inelastic neutron scattering

Neutron scattering is a powerful probe of strongly correlated systems. It can directly detect common phenomena such as magnetic order, and can be used to determine the coupling between magnetic moments through measurements of the spin-wave dispersions. In the absence of magnetic order, one can detect diffuse scattering and dynamic correlations. Neutrons are also sensitive to the arrangement of atoms in a solid (crystal structure) and lattice dynamics (phonons). With a spin angular momentum of  $\frac{1}{2}\hbar$ , the neutron interacts directly with the magnetization density of the solid. While elastic scattering can directly reveal static magnetic order (e.g., neutron diffraction provided the first experimental evidence for Néel antiferromagnetism [66]), through inelastic scattering one can probe dynamic spin-spin correlations [67].

The differential scattering cross section  $dS/d\Omega d\omega$  in inelastic neutron scattering (INS) experiments is a measure of the spin autocorrelation function, which can be expressed in terms of dynamical spin susceptibility  $\chi_{\vec{q}}(\omega)$  using the fluctuation-dissipation theorem (Eq. 1.10).

$$\frac{dS}{d\Omega d\omega} \sim \sum_{ij} \int dt \langle \sigma_i^-(t) \sigma_j^+(0) \rangle e^{i\omega t - i\vec{q} \cdot (\vec{r}_i - \vec{r}_j)} \propto \frac{1}{1 - e^{\beta\omega}} \text{Im} [\chi_{\vec{q}}(\omega)] \quad (1.11)$$

where  $\vec{\sigma}$  is the electronic spin and  $\beta$  is the inverse temperature. In an ordered antiferromagnet, one can measure the precession of the spins about their average orientations, which show up as dispersing spin waves, as shown in Fig. 1.7, for the square-lattice spin-1/2 antiferromagnet and high- $T_c$  parent compound  $La_2CuO_4$ .

## 1.4 Nonequilibrium theoretical approaches

The last section described various experiments which probe out of equilibrium response in Mott insulators and discussed the related phenomenology. In this section, we first review the theoretical methods available to study out of equilibrium lattice systems in presence of strong correlation. Then we go on to discuss the method we have developed and used to study the voltage biased Mott insulator at steady state.

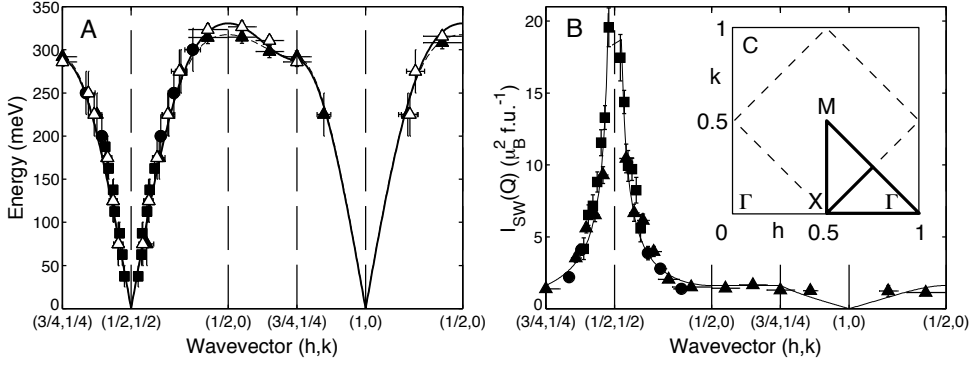


Figure 1.7: Spin waves in  $La_2CuO_4$ . (A) Dispersion relation along high symmetry directions in the 2D Brillouin zone, shown in inset (C), at  $T = 10K$  (open symbols) and  $295K$  (solid symbols). Solid (dashed) line is a fit to the spin-wave dispersion relation at  $T = 10K$  ( $295K$ ) which is obtained from a Heisenberg model with first-, second-, third-nearest neighbour and ring exchange magnetic couplings. (B) Wavevector dependence of the spin-wave intensity at  $T = 295K$  compared with predictions of linear spin-wave theory shown by the solid line. Taken from Ref. [68].

### 1.4.1 Time-dependent approaches

Generic nonequilibrium quantum systems are described by a time-dependent Schrödinger equation. A naive approach would be to solve it numerically for a many-body wave function. While this approach has been tried for small systems [69], it is, however, quite restricted in terms of the system size and accessible timescales, due to exponential growth of the Hilbert space dimension. Hence, alternative approaches often geared towards specific simplifying limits have been developed for nonequilibrium systems, some of which are discussed below.

#### 1.4.1.1 Time-dependent perturbative approaches

Time dependent perturbative approaches such as second order perturbation theory (SOPT), self-consistent perturbation theory and iterated perturbation theory (IPT) have been used to study nonequilibrium Hubbard model in the weak coupling regime. In the weak coupling perturbation theory the self energy is expanded to the requisite order and the Green's function is obtained by resumming the Dyson's series. This, and its generalisation to IPT, has been used to study problems like thermalisation in the Hubbard model after a quench [71, 123] and damping of Bloch oscillations [72]. They have been useful in identifying various *prethermal* regimes in the isolated Hubbard model.

Bare perturbation theory is not a conserving approximation [73]. As a result conserved quantities, like the total energy after a quench, keep drifting even when the Hamiltonian becomes time independent (post-quench). To remedy this self-consistent approaches which use the dressed Green's function to construct the self energy have been developed. Still, they fail to capture the dynamics even for moderate interaction strengths when compared against exact methods [116]. Sophisticated resummation techniques like the T-matrix approximation [74, 75] and its variants

also fail when the interaction strength becomes larger than the bandwidth of the noninteracting system. Hence, the applicability of perturbative expansions in the interaction strength for studying out of equilibrium insulator metal transition at long times even within the dynamical mean field theory (DMFT) framework (discussed below) remains unclear.

Other approaches which exploit the largeness of the number of internal degree of freedom  $\mathcal{N}$ , or that of the spatial dimensions  $\mathcal{D}$ , can be used to study the time dependent response of interacting many body systems. Within these schemes it can be shown that processes beyond a certain order in the expansion parameter become irrelevant as  $\mathcal{N}(\mathcal{D}) \rightarrow \infty$ . Although they involve a formal perturbative expansion in terms of the inverse of some large parameter, these approaches often yield results which are nonperturbative in the strength of interaction and driving fields.

One such study has focussed on the nonequilibrium response of quantum dot arrays, with a large  $\mathcal{N}$  no. of onsite levels, which are coupled to each other by nearest-neighbour tunneling matrix[76]. By setting up an expansion in the dimensionless tunneling conductance, it has been shown that terms beyond the second order drop out in the  $\mathcal{N} \rightarrow \infty$  limit. This limit also allows one to obtain analytic expression for the transient and long time bond currents flowing across the system. It captures some generic features of field driven Hubbard models, like the damping of Bloch oscillations at finite interaction strength and ‘breakdown’ of the Mott insulator beyond a threshold field. However, it fails to predict the nature of breakdown transition or that of the state at large field.

#### 1.4.1.2 Time-dependent Gutzwiller Mean Field Theory

The time-dependent Gutzwiller (TDG) [77–80] method is an extension of the well known Gutzwiller approximation [81–83] which involves making a variational ansatz for the time-dependent wavefunction and becomes exact in the limit of infinite coordination. The dynamics of the variational parameters and of the wavefunction is obtained by applying the time-dependent variational principle on the action and imposing local constraints. In doing so, the interacting many-body Hamiltonian gets mapped to an effective noninteracting Hamiltonian which depends on local variational parameters and defines an effective Schrödinger equation for the noninteracting electrons. The variational parameters themselves are determined by an evolution equation that involves the effective Hamiltonian. This allows the method to capture local correlations beyond the standard mean-field techniques.

However, it describes particle dynamics only in terms of an effective one-body Hamiltonian and does not couple states at different momenta. This misses out the dissipative processes (collisions) which lead to a genuine relaxation to steady state. It has been used to study quench problems [77, 78] and nonlinear transport in a Mott insulator connected to leads [80]. However, it does not capture qualitative features of the  $I - V$  characteristics found in experiments on Mott insulators. Moreover, the temperature dependence of the nonequilibrium response has not been established using this method although a finite temperature generalization of the method exists

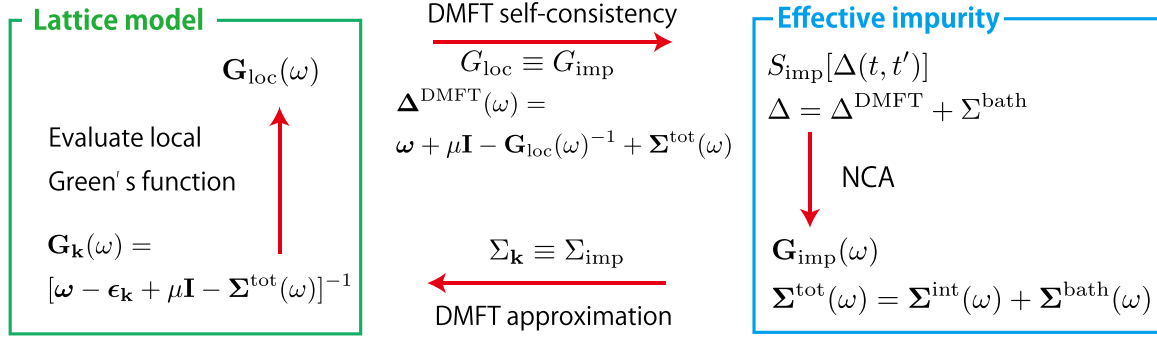


Figure 1.8: DMFT self-consistency (Ref. [121]).

[84].

### 1.4.1.3 Time-dependent DMRG

The density matrix renormalisation group (DMRG) [85–87] is presently the most successful numerical method for studying low temperature (or ground state) properties of one dimensional quantum lattice systems at equilibrium [88]. In recent years, it has undergone remarkable developments, due to insights from information theoretic concepts and the generalization to matrix product states (MPS) [89–91]. It has been extended and adapted to study real-time evolution [90–93], even at finite temperature and in presence of dissipation [94].

In the context of nonequilibrium dynamics in Mott insulators, it has been applied to study breakdown of the field driven isolated Mott insulator [95, 96], and the bias driven nonlinear transport in a Mott insulator connected to leads [97]. However, it could only access relatively short times which indicate that the system might be stuck in a prethermalised phase. Moreover, DMRG, by construction, is limited to one dimensional or quasi-two dimensional systems, like ladders etc., whose properties are known to be very different from two or three dimensional systems.

### 1.4.1.4 Nonequilibrium dynamical mean field theory

Dynamical mean field theory (DMFT) [98] has been a versatile tool for studying strongly correlated lattice systems for nearly three decades. The central idea in this approach is mapping of a lattice problem to an effective impurity problem immersed in a self-consistently obtained bath [99]. The mapping becomes exact in the limit of infinite dimensions [100]. The method treats spatial correlations in a mean-field manner, but accurately treats the temporal quantum fluctuations. Some amount of spatial correlations can be recovered by its real-space [101] and cluster extensions [102]. It has been used extensively to study insulator-metal transitions in two and three dimensional lattice systems and has been successful in modeling real materials when combined with band structure calculations [103]. A nonequilibrium generalization of this method has been developed [104, 105] and used to study a large number of nonequilibrium problems



including Bloch oscillations [106, 107], dielectric breakdown of Mott insulators [108–110], photoexcitations and photodoping [112–114], time-dependent parameter changes [116–118] and periodically driven systems [119–121].

Fig.1.8 shows the algorithm for DMFT self-consistency schematically. A crucial ingredient within the DMFT framework is the *impurity solver* - the technique used to solve the effective impurity problem. Different solvers can give very different results in the same physical situation; so one must select the correct solver depending on the problem at hand. At equilibrium, quantum Monte-Carlo (QMC) solvers provide an *exact* solution of the impurity problem in situations which allow for successful handling of the *fermion sign-problem*. However, additional complications arise in the nonequilibrium context essentially because of real time evolution, in which case the continuous-time Monte-Carlo (CTQMC) [122] schemes suffer from the dynamical sign-problem (also known as the phase-problem). This limits the time range over which accurate results can be obtained. For nonequilibrium DMFT applications, the times which can be reached with the strong-coupling CTQMC approach are usually too short. The weak-coupling CTQMC method, on the other hand, has been useful for studying ultrafast phenomena in the weak to intermediate coupling regime [117, 123, 124].

On the other hand there are approximate solvers like IPT and non-crossing approximation (NCA) [125] which are computationally cheaper and perform reasonably for equilibrium problems. IPT, which reproduces the correct strong coupling limit at half-filling in equilibrium, fails beyond weak coupling in the nonequilibrium setting. NCA and its extensions provide reliable results in the strong insulating phase but falter in the metallic phase at low temperatures. Moreover, inhomogeneous systems and symmetry broken phases with nontrivial spatial configurations bring in additional complications and are poorly handled within this framework.

Due to these issues DMFT has difficulty in handling steady state (non-periodic) nonequilibrium problems. Specifically, for the voltage driven breakdown of Mott insulators, which requires dealing with long-time response of an inhomogeneous system, it does not capture the qualitative features in the current-voltage characteristics as found in experiments. Recently, there has been an extension of nonequilibrium DMFT specifically meant to handle steady state problems which will be discussed below.

## 1.4.2 Steady state approaches

### 1.4.2.1 Imaginary time effective equilibrium approaches

The central idea in equilibrium statistical mechanics is that the statistical density matrix of a state  $s$  at energy  $E_s$  and particle number  $N_s$  is given by the Boltzmann factor  $e^{-\beta(E_s - \mu N_s)}$ . This facilitates theoretical description of quantum systems in equilibrium since both the thermal average and time evolution are based on the same operator, and one can use Wick rotation to formulate an imaginary time theory which captures both types of dynamics. The real time correlators can be obtained by performing an analytic continuation of the imaginary time correlation functions, and

connection with experiments can also be made by utilising the fluctuation-dissipation theorems, well established at equilibrium.

Away from equilibrium, the form of statistical density matrix is unknown. In principle, one must track the exact evolution of the system starting from some initial time  $t_0$  to some later time  $t_f$  till all measurements have been recorded. However, in presence of dissipation, if the separation between  $t_0$  and  $t_f$  is large as compared to the intrinsic relaxation time, then properties of the system become time independent at long times even in presence of strong driving. An early attempt to formulate NESS in quantum many-body systems was made by Zubarev [126], who tried to construct a time-independent density matrix formalism by solving the equation of motion within the scattering state formalism. This approach has later been revisited by Hershfield in the context of transport through quantum dot systems [127] whereby one can express such nonequilibrium quantum impurity models in terms of the system's Lippmann–Schwinger operators [128].

**Hershfield  $Y$  operator technique** The NESS density matrix  $\rho$  is written in the Boltzmann form,  $\rho = \exp(-\beta(H - Y))$  by introducing a new operator  $Y$  (known as the Hershfield  $Y$  operator) which takes care of nonequilibrium boundary conditions like lead chemical potentials etc. Hershfield introduced the idea that  $Y$  can be expressed in terms of Lippmann-Schwinger operators  $\psi_{\alpha k \sigma}$  which are fermionic operators that diagonalize the full Hamiltonian (including the leads and the coupling terms)

$$H = \sum_{\alpha k} \epsilon_{\alpha k} \psi_{\alpha k \sigma}^\dagger \psi_{\alpha k \sigma} \quad (1.12)$$

and can be formally expressed by the equation

$$\psi_{\alpha k \sigma}^\dagger = c_{\alpha k \sigma}^\dagger + \frac{1}{\epsilon_{\alpha k} - \mathcal{L} + i\eta} \mathcal{L}_T c_{\alpha k \sigma}^\dagger \quad (1.13)$$

where  $c_{\alpha k \sigma}^\dagger$  creates an electron in state  $k$  with spin projection  $\sigma$  in the lead  $\alpha$ . In a symmetric left-right lead setup  $\alpha$  takes values  $\pm 1$ . The corresponding dispersion in the leads is denoted by  $\epsilon_{\alpha k}$ .  $\mathcal{L}$  and  $\mathcal{L}_T$  are Liouvillian superoperators corresponding to the full Hamiltonian  $H$  and the tunneling Hamiltonian  $H_T$ , which couples the leads with the interacting system, respectively. Hershfield showed that the  $Y$  operator has the general form

$$Y = \frac{\Phi}{2} \sum_{\alpha k \sigma} \alpha \psi_{\alpha k \sigma}^\dagger \psi_{\alpha k \sigma} \quad (1.14)$$

where  $\Phi$  is the source-drain voltage which is given by the chemical potential difference between the two leads. These scattering operators allow one to reformulate the nonequilibrium problem as an effective equilibrium problem associated with a modified Hamiltonian. The existence and uniqueness of the steady state is tied to the validity of the inequalities  $v_F/L \ll |t_0|^{-1} \ll \eta$ , where  $v_F$  denotes the Fermi velocity,  $t_0$  is the time instant in which the system-bath coupling is switched

on,  $\eta \rightarrow 0^+$  defines a *slow* switch-on rate and  $L$  the linear system size [129]. Intuitively, these inequalities ensure that hot electrons hopping onto a given lead at time  $t_0$  will not be reflected back and return to the junction before the measurement process, and further that the process of switching on  $H_T$  remains adiabatic.

These equations can be easily solved for a non-interacting system. The primary issue with this, in principle exact formulation, is that it cannot be readily applied for interacting problems because it requires the solution of the Lippmann-Schwinger equation for the scattering states, which amounts to knowing the full solution itself. Some efforts have been made to directly implement Hershfield's density matrix within finite-order perturbation theories [130–132] but they have proven quite cumbersome to be extended to infinite orders. Hence, the applicability of these methods for interacting problems is limited to the perturbative regime, except for special scenarios [133]. Moreover, they have been applied mainly to very small systems like quantum dots, and their effectiveness for generic strongly correlated systems remains unclear. Next, we discuss a nonperturbative extension of this method and its domain of validity.

**Matsubara Voltage** Han and Heary [134] proposed that, by introducing a Matsubara term to the source-drain voltage, one can extend the equilibrium formalism such that the perturbation expansion of the imaginary-time Green function can be mapped to the Keldysh real-time theory. The unperturbed Hamiltonian is written as

$$K_0(i\phi_m) = H_0 + (i\phi_m - \Phi) Y_0 \quad (1.15)$$

with the *Matsubara voltage*  $\phi_m = 4\pi m/\beta$  with integer  $m$ . Since  $[H_0, Y_0] = 0$ ,  $e^{-\beta K_0} = e^{-\beta(H_0 - Y_0)} e^{-i\phi_m \beta Y_0}$  and  $e^{-i\phi_m \beta Y_0} = 1$ , the Matsubara voltage drops out and we have the identity

$$e^{-\beta K_0(i\phi_m)} = e^{-\beta(H_0 - \Phi Y_0)} = \rho_0 \quad (1.16)$$

However for a generic point on the imaginary time axis  $\tau \in [0, \beta)$ ,  $e^{-i\phi_m \tau Y} \neq 1$ , and hence the above identity does not hold for the *interacting* density matrix.

By treating the interaction as a perturbation the expectation value of any operator  $A$  can be expanded in powers of the interaction - the Dyson's series expansion - within a real time Keldysh theory for long times and also within an imaginary time theory. It has been argued in Ref. [135] that there exists a term-by-term correspondence of the two expansions provided one makes analytic continuations  $i\phi_m - \Phi \rightarrow 0$  and  $\tau \rightarrow it$ , in that order, and treats energy denominators in the imaginary time expansion to be principal valued

$$\frac{1}{(K_n - K_m)} \rightarrow \mathcal{P} \left( \frac{1}{E_n - E_m} \right) \quad (1.17)$$

as  $i\phi_m \rightarrow \Phi$ .

Although, a straightforward analytic continuation of the nonequilibrium Keldysh contour to



an imaginary-time one is not possible [135], the above procedure provides a nonperturbative mapping of real time observables at long times with the expectation values of the corresponding operators in imaginary time, which can be calculated using numerically exact techniques like QMC. This is potentially a powerful technique for nonequilibrium steady-state problems. However, it was found that the range of validity of this mapping could only be ascertained for specific kinds of level-connectivity and, more importantly, it could not be established for serially coupled dots [136]. This limits the applicability of this formalism to interacting lattice systems.

#### 1.4.2.2 Mean field approaches

One of the simplest methods used to study the NESS in interacting systems is the mean field approach. For the Hubbard model it involves factorization of the onsite interaction term to introduce classical fields which couple to the charge or spin of the fermions. Thus, the interacting problem gets mapped to an effectively noninteracting problem in which the static background fields have to be determined self-consistently.

This has been used to study a variety of steady state problems: pattern formation in 1D Hubbard model [137], filamentary conduction in disordered systems [141], insulator-metal transition induced by an electric field [142] and breakdown of one-dimensional insulators in presence of long-range Coulomb interaction [143]. However, an unrestricted Hartree-Fock treatment of the onsite Hubbard repulsion taking into account the self-consistent renormalisation of the local potential for a voltage driven system was lacking in the literature. We have developed such a scheme details of which shall be discussed in the subsequent chapters.

#### 1.4.3 Auxiliary master equations

The auxiliary master equation approach (AMEA) [144] is a DMFT formulation specifically meant to deal with NESS systems which treats the impurity problem within an auxiliary system consisting of a correlated impurity, a small number  $N_B$  of uncorrelated bath sites and two Markovian environments described by a Lindblad master equation. The approach allows for a solution of the steady-state impurity problem with controlled accuracy and, in many cases, with a small  $N_B$ , while the exact bath spectral function is smoothly obtained in the  $N_B \rightarrow \infty$  limit. The Lindblad quantum master equation can be readily solved by diagonalizing the Lindbladian within the many-body “super-Fock” space of reduced density matrices of the system. Its solution determines both the retarded and Keldysh impurity Green’s function as well as the self-energy, which is subsequently used in the DMFT loop to obtain the new bath hybridization function, which is fitted by new bath parameters.

AMEA has primarily been used to solve transport problems in heterojunctions with a layer of correlated sites sandwiched between noninteracting leads [144, 145]. A real-space version of this has been used to study the interplay of Hubbard repulsion and long-range Coulomb interaction on the charge redistribution at the interface of a paramagnetic Mott insulator sandwiched

---

between two metallic leads [146]. However, it has not been used to study the temperature dependent nonequilibrium transport characteristics of the Mott insulator at steady state, although the formulation should, in principle, be able to capture this.

## 1.5 Our motivation and principal results

We wish to study the finite temperature steady state response of a voltage driven Mott insulator connected to noninteracting leads. Additionally, we also wish to capture the dynamics of the collective modes (magnons) in the voltage driven state.

Unlike the equilibrium scenario, there are no *exact* methods for studying nonintegrable lattice systems out of equilibrium, except in 1D. The quantum Monte-Carlo approaches are severely limited in size and accessible times, and are further marred by the ‘phase problem’. The situation is worse when we consider nonperturbative approaches which attempt to access the long time state at large bias in reasonably sized systems. The AMEA is a potential candidate, but it has not been applied to this specific scenario. Moreover, it is likely to miss the collective mode dynamics due to the local nature of the DMFT approximation.

We have developed a real space and real time scheme to tackle out of equilibrium strongly correlated problems in a dissipative environment. It exploits the separation of timescales between the ‘fast’ electronic degrees of freedom and the ‘slow’ collective modes. Starting from a Schwinger-Keldysh action we arrive at the effective Langevin equation governing the dynamics of the slow degrees of freedom. The scheme gives access to a variety of many body problems in open systems.

At zero temperature this reduces to a nonequilibrium unrestricted Hartree-Fock theory. Using this, we have studied the transport and spectral properties across the voltage-driven insulator-metal transition in a two dimensional Mott insulator connected to noninteracting leads at zero temperature. We find that the effect of bias penetrates deeper into the system with increasing voltage. Moreover, a lengthscale can be associated with the bias, that controls the degree of penetration and ‘diverges’ as the bias approaches a critical value. A strong spatial dependence is also reflected in the local density of states, the charge density and local moment profile inside the system.

We have applied the finite temperature Langevin scheme to study the nonequilibrium steady state response in the half-filled three dimensional Hubbard model, with large onsite repulsion. At low temperatures, we find a voltage driven first order transition from a Mott insulator to a correlated metal. The current-voltage characteristics show hysteresis with respect to voltage sweeps, up to some coexistence temperature, as found in experiments on various transition metal oxides. The Néel temperature is strongly renormalized, and a new temperature scale for insulator metal transition (absent in the equilibrium phase diagram), emerges at large bias.

Being formulated in real time, the Langevin scheme can also access dynamical correlations at steady state, like collective mode spectrum, current noise etc. In this regards, we study the effect

---

of voltage bias on the magnon spectrum in the two dimensional Hubbard model at low, but finite temperature. At low bias we recover the antiferromagnetic spin waves with Goldstone modes at wavevectors  $(0, 0)$  and  $(\pi, \pi)$ , but with additional features due to broken translation symmetry along the longitudinal direction due to the leads. We find that as the voltage approaches critical value the spin wave spectrum develops a new diffuse branch at lower energy. Beyond the critical voltage the usual spin wave spectrum disappears and low energy branch becomes more diffuse, although remnants of the Goldstone features still survive.

## Theoretical tools

### 2.1 Model

The focus in this thesis is on Mott insulators connected to non-interacting leads with a chemical potential difference between them. In addition to introducing the voltage bias, the leads provide dissipative channels for the system to relax. The isolated Mott insulator when subjected to a field does not thermalise for a significantly long time, and instead gets trapped in a prethermalised metastable state[71]. The presence of metallic leads at the two edges allows relaxation to a nonequilibrium steady state (NESS) [147].

We model the Mott insulator (“system”) by the repulsive Hubbard model, while the leads are modelled as conducting electron reservoirs. Each site at the left and right edges of the Mott insulator, Fig. 2.1, is coupled to the nearest bath site via a tunnelling matrix element.

$$\mathcal{H} = \mathcal{H}_{sys} + \mathcal{H}_{bath} + \mathcal{H}_{coup} \quad (2.1)$$

$$\mathcal{H}_{sys} = \sum_{\langle ij \rangle, \sigma} -t_{ij} d_{i\sigma}^\dagger d_{j\sigma} + U \sum_i n_{i\uparrow} n_{i\downarrow} \quad (2.1a)$$

$$\mathcal{H}_{bath} = \sum_{\nu, \beta} (\epsilon_\nu - \mu_\beta) c_\nu^{\dagger\beta} c_\nu^\beta \quad (2.1b)$$

$$\mathcal{H}_{coup} = \sum_{\langle ij \rangle, \sigma} v_{ij} \left( c_{i\sigma}^{\dagger L} d_{j\sigma} + c_{i\sigma}^{\dagger R} d_{j\sigma} + h.c. \right) \quad (2.1c)$$

where  $c_\nu^{\dagger\beta}$  ( $c_\nu^\beta$ ) denote the creation (annihilation) operators of the bath  $\beta \in \{L, R\}$  ( $L$  denotes the left lead and  $R$  the right lead) in their eigenbasis, with eigenenergies  $\epsilon_\nu$ .  $\mu_\beta$  are the chemical potentials in the noninteracting leads.  $\mu_{L,R} = \mu \pm (V/2)$ ,  $V$  being the applied bias.  $v_{ij}$  denote the matrix elements of the system-bath coupling.  $d_{i\sigma}^\dagger$  ( $d_{i\sigma}$ ) are the corresponding operators for the system.  $t_s$ ,  $\mu$  and  $U$  are the nearest-neighbour hopping amplitude, chemical potential and onsite Coulomb repulsion strength, respectively, in the system. Within this setup, we study the 2D dissipative Hubbard model at zero temperature and its collective mode dynamics at low, but

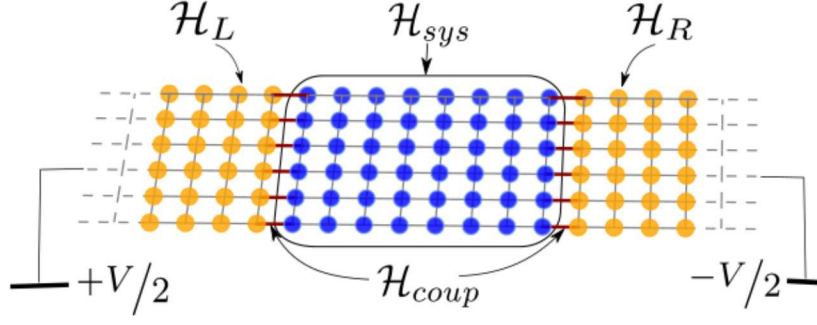


Figure 2.1: Schematic diagram showing the setup. The sites having onsite Hubbard repulsion are marked in blue, while the noninteracting bath sites are marked in yellow. The coupling between the system and the bath is denoted by red bonds. The bias is applied symmetrically at the two edges by tuning the chemical potential of the baths.

finite temperature. We also study the finite temperature phases in the 3D Hubbard model driven out of equilibrium by a voltage bias.

## 2.2 Methods

Starting from the Hamiltonian defined in eq.2.1 one can construct the generating functional by discretising the complex time Keldysh contour shown in Fig. 2.2,

$$Z = \int \mathcal{D}\{\bar{c}, c; \bar{d}, d\} e^{iS[\bar{c}, c; \bar{d}, d]} \quad (2.2)$$

where  $(\bar{c}, c)$  and  $(\bar{d}, d)$  are the Grassmann fields for the lead and system fermions respectively.  $S[\bar{c}, c; \bar{d}, d]$  is the complex time Keldysh action defined on the contour.

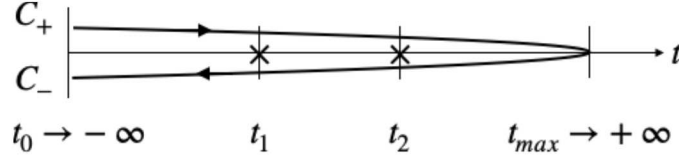
$$S = \int_{-\infty}^{\infty} dt [\mathcal{L}_{sys}(t) + \mathcal{L}_{bath}(t) + \mathcal{L}_{coup}(t)] \quad (2.2a)$$

$$\mathcal{L}_{sys}(t) = \sum_{\langle ij \rangle, \sigma, s} s \bar{d}_{i\sigma}^s(t) (i\partial_t + t_s) d_{j\sigma}^s(t) - U \sum_{i,s} s n_{i\uparrow}^s(t) n_{i\downarrow}^s(t) \quad (2.2b)$$

$$\mathcal{L}_{bath}(t) = \sum_{\nu, \beta, s} s \bar{c}_{\nu\beta}^s(t) (i\partial_t - \epsilon_{\nu} + \mu_{\beta}) c_{\nu\beta}^s(t) \quad (2.2c)$$

$$\mathcal{L}_{coup}(t) = \sum_{\langle ij \rangle, \sigma} v_{ij} (\bar{c}_{i\sigma}^{sL}(t) d_{j\sigma}(t) + \bar{c}_{i\sigma}^{sR}(t) d_{j\sigma}(t) + g.c.) \quad (2.2d)$$

where  $i, j$  are the lattice indices,  $\sigma$  is the spin index,  $\alpha$  labels the leads and  $s$  labels the contour.  $s = \pm 1$  for the upper and the lower contour fields respectively. At each time slice, and for every



$$C = C_+ \cup C_-$$

Figure 2.2: The complex time Keldysh contour for accessing steady states. In order to access steady states one can take  $t_0$  (initial time) and  $t_{max}$  (maximum time) to  $\pm\infty$ . In order to calculate observables, e.g. the two-point function, one makes insertions at intermediate times  $t_1$  and  $t_2$ .

site we can rewrite the interaction term as

$$U n_{i\uparrow}^s n_{i\downarrow}^s = \frac{U}{4} (n_i^s)^2 - U \left( \vec{\sigma}_i^s \cdot \hat{\Omega}_i^s \right)^2 \quad (2.3)$$

where we have suppressed the time label for brevity. Here,  $n_i^s = \bar{c}_{i\uparrow}^s c_{i\uparrow}^s + \bar{c}_{i\downarrow}^s c_{i\downarrow}^s$  is the local density,  $\vec{\sigma}_i^s = \frac{1}{2} \sum_{\alpha\beta} \bar{c}_{i\alpha}^s \vec{\tau}_{\alpha\beta} c_{i\beta}^s$  is the local spin operator and  $\hat{\Omega}_i^s$  is an arbitrary SO(3) vector.  $\vec{\tau}$  is the  $2 \times 2$  Pauli vector.

Each of the two terms can be decomposed by a Hubbard-Stratonovich (HS) transformation. The first transformation introduces a “charge field”  $\phi_i(t)$ :

$$e^{-i \frac{sU}{4} (n_i^s(t))^2} \propto \int d\phi_i^s(t) e^{i \left( \frac{s}{U} (\phi_i^s(t))^2 - s \phi_i^s(t) n_i^s(t) \right)} \quad (2.3a)$$

The HS transformation on the second term can be written in terms of an O(3) “spin field”  $\vec{M}_i(t)$

$$e^{i s U (\vec{\sigma}_i^s(t) \cdot \hat{\Omega}_i^s(t))^2} \propto \int d^3 \vec{M}_i^s(t) e^{i \left( -\frac{s}{U} (|\vec{M}_i^s(t)|)^2 + s \vec{M}_i^s(t) \cdot \vec{\sigma}_i^s(t) \right)} \quad (2.3b)$$

Upon introducing the auxiliary fields the action becomes quadratic in the fermions, which can be integrated out to get the following effective action:

$$\tilde{S}[\phi, M] = -\iota Tr \ln [\iota \check{G}^{-1}(t, t')] + \frac{1}{U} \int dt \sum_i \left[ \phi_i^c(t) \phi_i^q(t) - \vec{M}_i^c(t) \cdot \vec{M}_i^q(t) \right] \quad (2.4)$$

with

$$\check{G}^{-1}(t, t') = \begin{pmatrix} \hat{G}_R^{-1} & \hat{G}_{12}^{-1} \\ \hat{G}_{21}^{-1} & \hat{G}_A^{-1} \end{pmatrix} \quad (2.4a)$$

where the components of  $\check{G}^{-1}$  in the  $2 \times 2$  Keldysh space are given by:

$$\hat{G}_R^{-1}(t, t') = \left( \iota \partial_t - \hat{\mathcal{H}}^c(t) \right) \delta(t - t') + \hat{\Gamma}^R(t, t') \quad (2.4b)$$

$$\hat{G}_A^{-1}(t, t') = \left( \iota \partial_t - \hat{\mathcal{H}}^c(t) \right) \delta(t - t') + \hat{\Gamma}^A(t, t') \quad (2.4c)$$

$$\hat{G}_K^{-1}(t, t') = \hat{\Gamma}_{ij\alpha}^K(t, t') \delta_{\alpha\alpha'} + \left( \hat{G}_R^{-1} \circ F - F \circ \hat{G}_A^{-1} \right)(t, t') \quad (2.4d)$$

$$\left[\hat{G}_{12}^{-1}(t, t')\right]_{ij; \alpha\alpha'} = \frac{1}{2} \left( \vec{M}_i^q(t) \cdot \vec{\tau}_{\alpha\alpha'} - \phi_i^q(t) \delta_{\alpha\alpha'} \right) \delta_{ij} \delta(t - t') + \left[\hat{G}_K^{-1}(t, t')\right]_{ij; \alpha\alpha'} \quad (2.4e)$$

$$\left[\hat{G}_{21}^{-1}(t, t')\right]_{ij; \alpha\alpha'} = \frac{1}{2} \left( \vec{M}_i^q(t) \cdot \vec{\tau}_{\alpha\alpha'} - \phi_i^q(t) \delta_{\alpha\alpha'} \right) \delta_{ij} \delta(t - t') \quad (2.4f)$$

$$\hat{\mathcal{H}}_{ij}^c(t) = \left( \phi_i^c(t) \mathbb{1}_2 - \vec{M}_i^c(t) \cdot \vec{\tau} \right) \delta_{ij} - t_{<ij>} \mathbb{1}_2 \quad (2.4g)$$

where  $\mathbb{1}_2$  is the  $2 \times 2$  identity matrix.  $\hat{\mathcal{H}}^c(t)$  is a time-dependent Hamiltonian which depends on the ‘classical’ component of the auxiliary fields.  $\hat{\Gamma}^{R,A,K}(t, t')$  are dissipation terms which enter the action as a result of integrating out the leads. We approximate the density of states of the leads with a Lorentzian function which does not have nonanalytic features like van Hove singularities or band edges, since these can lead to non-Markovian memory kernels in the correlation functions of the system at long time, as reported in Ref. [148].  $F(t, t')$  is the distribution function of the disconnected system, and  $\circ$  denotes convolution. The ‘classical’ and ‘quantum’ components of the auxiliary fields are linear combinations of the fields introduced in the H-S transformations in Eqs. 2.3a and 2.3b.

$$\vec{M}^c = \frac{1}{2} \left( \vec{M}^+ + \vec{M}^- \right), \quad \vec{M}^q = \left( \vec{M}^+ - \vec{M}^- \right) \quad (2.5)$$

where we have suppressed the time and other labels for notational brevity. A similar transformation holds for the  $\phi$  fields. We have mapped the original fermionic action for the dissipative Hubbard model into an action containing time dependent auxiliary fields. The mapping is formally *exact* up to this point. Next, we make physically motivated approximations and derive two kinds of effective theories.

### 2.2.1 Keldysh mean field theory at $T = 0$

It is instructive to write the action in Eq. 2.4 in frequency representation.

$$\tilde{S}[\phi, M] = Tr \ln \left( i\check{G}^{-1}(\omega, \omega') \right) + \frac{1}{U} \int \frac{d\omega}{2\pi} \sum_i \left( \phi_i^c(\omega) \phi_i^q(-\omega) - \vec{M}_i^c(\omega) \cdot \vec{M}_i^q(-\omega) \right) \quad (2.6a)$$

where the components of  $\check{G}^{-1}$  in the  $2 \times 2$  Keldysh space are given by,

$$\left[ \left( \hat{G}^{-1} \right)^R \right]_{ij; \alpha\alpha'} = (\omega \delta_{ij} + t_{<ij>} + i\hat{\Gamma}_{ij\alpha}^R(\omega)) \delta_{\alpha\alpha'} \delta(\omega - \omega') - (\phi_i^c(\omega - \omega') \delta_{\alpha\alpha'} - \vec{M}_i^c(\omega - \omega') \cdot \vec{\tau}_{\alpha\alpha'}) \delta_{ij} \quad (2.6b)$$

$$\left[ \left( \hat{G}^{-1} \right)^{12} \right]_{ij; \alpha\alpha'} = \frac{1}{2} (\vec{M}_i^q(\omega - \omega') \cdot \vec{\tau}_{\alpha\alpha'} - \phi_i^q(\omega - \omega') \delta_{\alpha\alpha'}) \delta_{ij} + \hat{\Gamma}_{ij\alpha}^K(\omega) \delta(\omega - \omega') \delta_{\alpha\alpha'} \quad (2.6c)$$

$$\left[ \left( \hat{G}^{-1} \right)^{21} \right]_{ij; \alpha\alpha'} = \frac{1}{2} (\vec{M}_i^q(\omega - \omega') \cdot \vec{\tau}_{\alpha\alpha'} - \phi_i^q(\omega - \omega') \delta_{\alpha\alpha'}) \delta_{ij} \quad (2.6d)$$

$$\left[ \left( \hat{G}^{-1} \right)^A \right]_{ij; \alpha\alpha'} = (\omega \delta_{ij} + t_{<ij>} + i \hat{\Gamma}_{ij\alpha}^A(\omega)) \delta_{\alpha\alpha'} \delta(\omega - \omega') - (\phi_i^c(\omega - \omega') \delta_{\alpha\alpha'} - \vec{M}_i^c(\omega - \omega') \cdot \vec{\tau}_{\alpha\alpha'}) \delta_{ij} \quad (2.6e)$$

$\hat{\Gamma}^{R,A,K}(\omega)$  are Fourier transform of  $\Gamma^{R,A,K}(t, t')$ , assuming they depend only on  $t - t'$ . In making this assumption we have neglected the initial transient dynamics of the system after connecting the leads.

At this point one can, in principle, find the saddle point of this action with respect to the frequency dependent auxiliary fields. But for evaluating the saddle point equations one would have to invert the full frequency and site off-diagonal Green's function  $\check{G}^{-1}$ . This is a very challenging task, and requires some physically motivated approximations in order to proceed. Here we invoke the static path approximation (SPA)[24–26], in which we drop the frequency dependence of the auxiliary fields, and thus restrict ourselves to the description of steady states only. The advantage we gain is that the Green's functions become diagonal in frequency. This allows us to access much larger sizes, in order to establish detailed spatial dependence of various quantities of interest. This would be a drastic approximation if we were to consider the transient response of the system. But once it relaxes to a NESS, we expect the average long time behaviour to be reasonably captured by the zero frequency mode of the auxiliary fields. The effect of finite-frequency modes can be built back perturbatively on top of the zero-mode theory.

Let us introduce the notation,

$$\phi_i^{c,q}(\omega = 0) \equiv \phi_i^{c,q}, \quad \vec{M}_i^{c,q}(\omega = 0) \equiv \vec{M}_i^{c,q}$$

and make the auxiliary fields dimensionless by scaling them as

$$\phi_i^{c,q} \rightarrow \frac{U}{2} \phi_i^{c,q}, \quad \vec{M}_i^{c,q} \rightarrow \frac{U}{2} \vec{M}_i^{c,q}$$

With these steps we arrive at an effective steady state description given by the ‘static path’ action  $S^{SPA}$ ,

$$S^{SPA}[\phi, \vec{M}] = -iTr \ln [i\check{G}^{-1}(\omega)] + S'[\phi, \vec{M}] \quad (2.7a)$$

where,

$$\check{G}^{-1}(\omega) \equiv \begin{pmatrix} \left( \hat{G}^{-1}(\omega) \right)^R & \left( \hat{G}^{-1}(\omega) \right)^K \\ \hat{0} & \left( \hat{G}^{-1}(\omega) \right)^A \end{pmatrix} + \hat{\Sigma} \otimes \sigma_x \quad (2.7b)$$



with

$$\left[ \left( \hat{G}^{-1}(\omega) \right)^R \right]_{ij}^{\alpha\alpha'} = \left( (\omega + i\eta)\delta_{ij} + \hat{\Gamma}_{ij\alpha}^R(\omega) \right) \delta_{\alpha\alpha'} - \hat{H}_{ij}^{\alpha\alpha'} \quad (2.7c)$$

$$\left[ \left( \hat{G}^{-1}(\omega) \right)^A \right]_{ij}^{\alpha\alpha'} = \left( (\omega - i\eta)\delta_{ij} + \hat{\Gamma}_{ij\alpha}^A(\omega) \right) \delta_{\alpha\alpha'} - \hat{H}_{ij}^{\alpha\alpha'} \quad (2.7d)$$

$$\left[ \left( \hat{G}^{-1}(\omega) \right)^K \right]_{ij; \alpha\alpha'}^{\alpha\alpha'} = \hat{\Gamma}_{ij\alpha}^K(\omega) \delta_{\alpha\alpha'} + F(\omega - \mu) \left[ \left( \hat{G}^{-1}(\omega) \right)^R - \left( \hat{G}^{-1}(\omega) \right)^A \right]_{ij}^{\alpha\alpha'} \quad (2.7e)$$

$$\hat{\Gamma}_{ij\alpha}^{R,A,K}(\omega) = \sum_{\beta \in \{L,R\}} \left( \sum_{mn} v_{mi} v_{nj} g_{\beta, mn\alpha}^{R,A,K}(\omega) \right) \quad (2.7f)$$

$$\hat{H}_{ij}^{\alpha\alpha'} = -t_{<ij>} \delta_{\alpha\alpha'} + \frac{U}{2} (\phi_i^c \delta_{\alpha\alpha'} - \vec{M}_i^c \cdot \vec{\tau}_{\alpha\alpha'}) \delta_{ij} \quad (2.7g)$$

$$\hat{\Sigma}_{ij}^{\alpha\alpha'} = -\frac{U}{4} (\phi_i^q \delta_{\alpha\alpha'} - \vec{M}_i^q \cdot \vec{\tau}_{\alpha\alpha'}) \delta_{ij} \quad (2.7h)$$

and

$$S'[\phi, \vec{M}] = \frac{U}{4} \sum_i \left( \phi_i^c \phi_i^q - \vec{M}_i^c \cdot \vec{M}_i^q \right) \quad (2.7i)$$

$g_{\beta}^{R,A,K}(\omega)$  denote the retarded, advanced and Keldysh components of Green's function of the reservoir  $\beta$ , while  $\hat{G}^{R,A,K}$  denote those of the system.  $\hat{H}$  is an effective Hamiltonian which one can obtain if one retains only the zero frequency mode of the auxiliary fields.  $F(\omega - \mu)$  is the distribution function of the isolated system.  $\eta$  is a small positive number, which regulates the Keldysh action.

The mean-field consistency conditions can be obtained by extremising the SPA action with respect to the quantum auxiliary fields. We get the following family of saddle point equations:

$$\left. \frac{\delta S^{SPA}}{\delta \phi_i^q} \right|_{\phi^q, \vec{M}^q=0} = 0, \quad \left. \frac{\delta S^{SPA}}{\delta \vec{M}_i^q} \right|_{\phi^q, \vec{M}^q=0} = 0$$

These can be simplified to obtain the consistency conditions:

$$\int_{-D}^D d\omega \operatorname{Im} \left[ \operatorname{Tr} \left( \hat{G}_{ii}^K(\omega) \right) \right] = \phi_i^c \quad (2.8a)$$

$$\int_{-D}^D d\omega \operatorname{Im} \left[ \operatorname{Tr} \left( \hat{G}_{ii}^K(\omega) \vec{\tau} \right) \right] = \vec{M}_i^c \quad (2.8b)$$

where  $\hat{G}^K(\omega) = -\hat{G}^R(\omega) \left( \hat{G}^{-1}(\omega) \right)^K \hat{G}^A(\omega)$  and the trace is over the  $2 \times 2$  spin subspace.  $D$  is the cutoff in energy which must be larger than all other energy scales in the problem.

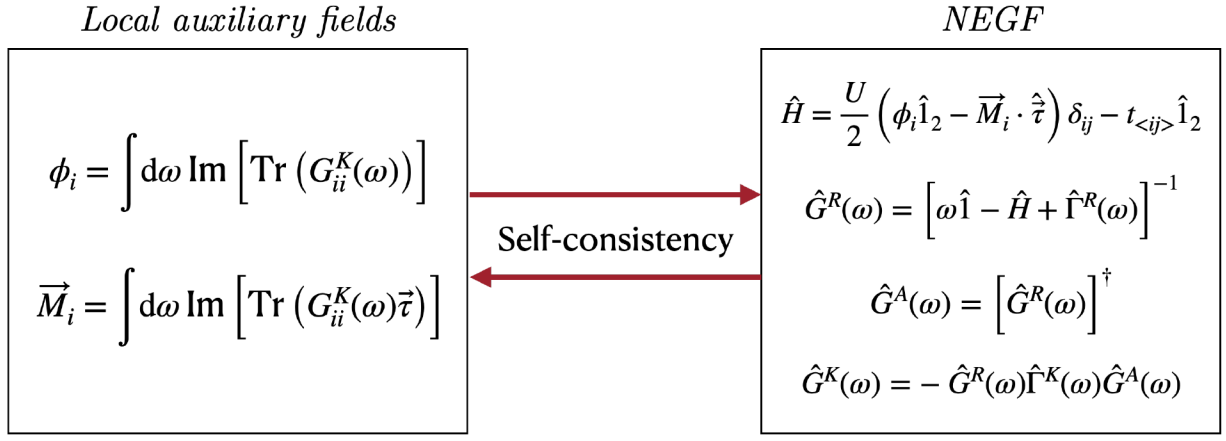


Figure 2.3: Implementation of self-consistency for Keldysh mean field theory.

### 2.2.1.1 Implementation of mean field consistency

Our method involves treating the Hubbard interaction within an unrestricted Hartree-Fock (HF). We have benchmarked the scheme against the analytically tractable zero temperature mean-field limit of the equilibrium ( $V = 0$ ) Hubbard model in 2D with periodic boundary conditions. The implementation of self-consistency is shown schematically in Fig.2.3. Starting with an initial guess for  $\{\phi^c \equiv \phi\}$  and  $\{M_z^c \equiv M\}$ , we calculate the auxiliary fields via frequency integrals of the locally projected Green's functions. The mean field consistency equations are solved iteratively until the solutions converge for every site. The convergence criteria used is  $\max_i \left[ \left( |\vec{M}_i|^{n+1} - |\vec{M}_i|^n \right) / |\vec{M}_i|^n \right] \leq 0.01$  or  $\max_i \left[ |\vec{M}_i|^{n+1} - |\vec{M}_i|^n \right] < 10^{-6}$ , where  $|\vec{M}_i|^n$  is the magnitude of the local moment at site  $i$  in the  $n$ -th iteration. A similar criteria has used for the  $\phi$  field as well.

In principle, one must solve for all the three components of  $\vec{M}^c$  at each site. For the square lattice, one can simplify the problem by retaining only the  $M_z^c$  component of the spin auxiliary field. This can be justified by performing a strong coupling expansion of the Keldysh action to find that the collinear state remains a consistent solution even at finite bias. We have elaborated on this point in Appendix A.

### 2.2.2 Langevin for the thermal steady state

Next, we derive an effective classical fluctuation theory, starting with Eq. 2.4, by making a series of approximations:

1. We fix the charge field ( $\phi$ ) to it's classical saddle point at equilibrium, i.e.,  $\phi_i^c, \phi_i^q = 0$ . This fixes the overall density to half-filling, but allows local density fluctuations due to dynamics of the spin-field ( $\vec{M}$ ). This is necessary because if the charge field is allowed to fluctuate, then its fluctuations become unbounded due to its negative stiffness about the saddle point. This is a well known problem in the literature. It must be emphasized that even though the dynamics of the charge field  $\phi$  is frozen, yet the theory allows for local

charge fluctuations due to amplitude fluctuations of the local moments  $|\vec{M}_i|$ . This point is discussed further in Appendix B.2.

2. We perform a cumulant expansion of the action to second order in  $\{M^q\}$  fields, introduce a ‘noise’ by decoupling the quadratic term, and evaluate the ‘classical’ saddle point to obtain a stochastic equation of motion (EOM).
3. We simplify the EOM by performing a semiclassical expansion of the two-point functions to obtain a ‘Langevin’ equation in terms of the ‘slow’ time coordinate. The noise kernel is assumed to be Gaussian, which can be motivated in the high temperature limit (Ref. Appendix B.1).

We discuss (2) and (3) below in detail.

### 2.2.2.1 Cumulant expansion

The  $\check{G}^{-1}$  introduced in Eq. 2.4a can be decomposed into a Green’s function  $\check{G}_c^{-1}$ , which depends only on the ‘classical’ field and a self-energy  $\check{\Sigma}_q$ , which depends only on the ‘quantum’ field.

$$\begin{aligned}\check{G}^{-1} &= (\mathbb{1} + \check{\Sigma}_q \circ \check{G}_c) \circ \check{G}_c^{-1} \\ \check{\Sigma}_q(t, t') &= \frac{1}{2} \vec{M}_i^q(t) \cdot \vec{\tau}_{\alpha\alpha'} \delta_{ij} \delta(t - t') \otimes \tau_K^x\end{aligned}\tag{2.9}$$

where  $\tau_K^x$  denotes the structure in  $2 \times 2$  Keldysh space. We expand the action in Eq. 2.4 to second order in  $\check{\Sigma}_q$ .

$$\tilde{S} = \tilde{S}^0 + \tilde{S}^1 + \tilde{S}^2 + \dots\tag{2.10}$$

$$\tilde{S}^0 = -i \text{Tr} \ln [\iota \check{G}_c^{-1}(t, t')] = 0\tag{2.10a}$$

$\tilde{S}^0$  vanishes from the causality relation between the retarded and advanced Green’s functions.

$$\tilde{S}^1 = \sum_i \int dt \left( \text{Im} \left[ \text{Tr} \left( \hat{G}_{ii}^K(t, t) \vec{\tau} \right) \right] - \frac{\vec{M}_i^c(t)}{U} \right) \cdot \vec{M}_i^q(t)\tag{2.10b}$$

$$\tilde{S}^2 = \frac{i}{2} \int dt \int dt' \sum_{ij;ab} M_{ia}^q(t) \left[ \hat{\Pi}^K(t, t') \right]_{ij}^{ab} M_{jb}^q(t')\tag{2.10c}$$

where

$$\begin{aligned}\left[ \hat{\Pi}^K(t, t') \right]_{ij}^{ab} &\equiv \text{Tr} \left[ \left( \hat{G}_{ij}^K(t, t') \tau^a \hat{G}_{ji}^K(t', t) \tau^b \right) \right. \\ &\quad \left. + \left( \hat{G}_{ij}^R(t, t') \tau^a \hat{G}_{ji}^A(t', t) \tau^b \right) + \left( \hat{G}_{ij}^A(t, t') \tau^a \hat{G}_{ji}^R(t', t) \tau^b \right) \right]\end{aligned}\tag{2.10d}$$

Now, we decompose the term quadratic in  $M^q$ .

$$e^{\iota \tilde{S}^2} = e^{-\frac{1}{2} M^q \circ \hat{\Pi}^K \circ M^q} \propto \int \mathcal{D}[\xi] \exp \left( -\frac{1}{2} \xi \circ [\hat{\Pi}^K]^{-1} \circ \xi + i \xi \circ M^q \right) \quad (2.10e)$$

Hence, this adds a term to the coefficient of  $M^q$  in  $\tilde{S}^1$  and additionally, the generating functional is reweighted by the quadratic piece in  $\xi$ .

We obtain the equation of motion by requiring that the first order variation w.r.t the ‘q’ fields must vanish at  $\phi^q = 0$ ,  $\vec{M}^q = 0$ . This gives us the following equation for the ‘c’ fields

$$\text{Im} \left[ \text{Tr} \left( \hat{G}_{ii}^K(t, t) \vec{\sigma} \right) \right] = \vec{M}_i^c(t) - \vec{\xi}_i(t) \quad (2.11a)$$

$$\langle \xi_i^a(t) \xi_j^b(t') \rangle = \left[ \hat{\Pi}^K(t, t') \right]_{ij}^{ab} \quad (2.11b)$$

Eq.2.11a is a stochastic equation for  $\{\vec{M}\}$  which looks decoupled in site index and time. This is, however, misleading as  $\check{G}_{ii}^K(t, t)$  is, in general, a non-local function of space and time. In order to calculate it one should solve the Kadanoff-Baym (KB) equations[149] taking into account the entire history of  $\{\vec{M}_i(t)\}$ . This is numerically challenging and so we would like to do away with the time kernels, if possible, while retaining the non-local character in spatial indices.

In the next section we shall see how the separation of timescales between the electronic and magnetic excitations can be invoked to simplify the time dependence.

### 2.2.2.2 Semiclassical expansion

In this section we suppress the spatial indices for the sake of notational brevity. Symbols with  $\hat{\phantom{x}}$  on them are to be interpreted as matrices. Starting from  $\hat{G}^K(t, t)$  and transforming to Wigner coordinates allows us to write

$$\hat{G}^K(t, t) = \hat{G}^K(t, t_r = 0) = \int d\omega \hat{G}^K(t, \omega) \quad (2.12)$$

In what follows, we would write a series expansion for  $\hat{G}^K(t, \omega)$  in powers of  $\hbar$ . For this purpose we first construct a series expansion for  $\check{G}^R$ .

**The retarded Green’s function  $\hat{G}^R$ :** The retarded Green’s function obeys the Dyson’s equation

$$(\hat{G}^{-1R} \circ \hat{G}^R)(t_1, t_2) = \delta(t_1 - t_2) \hat{1} \quad (2.13)$$

Transforming to Wigner coordinates allows us to expand the LHS in a Kramers-Moyal series[18],

$$\left(\omega - \hat{\mathcal{H}}^c(t) + \hat{\Gamma}^R(\omega)\right) \hat{G}^R(t, \omega) + \frac{\iota\hbar}{2} \left( \partial_t \hat{\mathcal{H}}^c(t) \partial_\omega \hat{G}^R - (\hat{1} + \partial_\omega \hat{\Gamma}^R) \partial_t \hat{G}^R \right) + O(\hbar^2) = \hat{1} \quad (2.13a)$$

where  $t \equiv \frac{t_1+t_2}{2}$  is the center-of-mass time, and  $\omega$  is the Fourier conjugate to the relative time  $t_r \equiv t_1 - t_2$ . Furthermore, we have assumed that  $\hat{\Gamma}^R$  depends only on the relative time, as is the case at steady state.

This expansion relies on the condition that  $\hbar \ll (\text{timescale for } \vec{M} \text{ fluctuations}) \times (\text{energy-scale for electronic excitations})$ . The timescale for magnetic fluctuations is set by  $J^{-1}$ , where  $J \sim \frac{t^2}{U}$  is the magnetic exchange scale, while the energy-scale for electronic excitations is set by the electronic bandwidth given by  $U$ , for  $U \ll t$ . Setting  $\hbar = 1$ , we then have the condition  $J \ll U$  for the expansion to be valid.

Inverting the equation above gives us

$$\hat{G}^R(t, \omega) = \hat{\mathcal{G}}^R(t, \omega) - \frac{\iota\hbar}{2} \left( \hat{\mathcal{G}}^R \partial_t \hat{\mathcal{H}}^c(t) \partial_\omega \hat{\mathcal{G}}^R + \hat{\mathcal{G}}^R (\hat{1} + \partial_\omega \hat{\Gamma}^R) \partial_t \hat{\mathcal{G}}^R \right) + O(\hbar^2) \quad (2.13b)$$

where,  $\hat{\mathcal{G}}^R(t, \omega)$  is the “adiabatic” retarded Green’s function given by

$$\hat{\mathcal{G}}^R(t, \omega) = \left( \omega \hat{1} - \hat{\mathcal{H}}^c(t) + \hat{\Gamma}^R(\omega) \right)^{-1} \quad (2.13c)$$

which depends only on the instantaneous configuration of the background field, and not on its history.

Now, for any matrix  $\hat{A}(\alpha)$ , we have  $\partial_\alpha \hat{A} = -\hat{A} \left( \partial_\alpha \hat{A}^{-1} \right) \hat{A}$ . Using this we can rewrite 2.13b to  $O(\hbar)$  as

$$\hat{G}^R(t, \omega) = \left( \hat{1} + \frac{\iota\hbar}{2} \left[ \hat{\mathcal{G}}^R \partial_t \hat{\mathcal{H}}^c, \hat{\mathcal{G}}^R (\hat{1} + \partial_\omega \hat{\Gamma}^R) \right] \right) \hat{\mathcal{G}}^R(t, \omega) \quad (2.13d)$$

where  $[ , ]$  denotes the commutator bracket.

**The Keldysh Green’s function  $\hat{G}^K$ :** Knowing  $\hat{G}^R$  and  $\hat{G}^A$  to any order in  $\hbar$  allows one to construct the  $\hat{G}^K$  to that order provided the distribution function is known apriori. In our case, the distribution function in the disconnected system  $F(\omega) = \tanh(\omega/2T)$  gets corrections due to hybridisation with the leads, as is apparent from the form of  $\hat{G}_K^{-1}(t', t'')$  defined in Eq.2.4d. From the structure of  $\check{G}^{-1}$ , it follows that

$$\hat{G}^K(t_1, t_2) = -\hat{G}^R(t_1, t') \circ \hat{G}_K^{-1}(t', t'') \circ \hat{G}^A(t'', t_2) \quad (2.14)$$

Transforming to Wigner coordinates and implementing the Kramers-Moyal expansion, as above, allows us to write

$$\hat{G}^K(t, \omega) = \hat{\mathcal{G}}^K(t, \omega) + \frac{i\hbar}{2} \left[ \hat{\mathcal{G}}^R \partial_t \hat{\mathcal{H}}^c, \hat{\mathcal{G}}^R \left( \hat{\mathbb{1}} + \partial_\omega \hat{\Gamma}^R \right) \right] F \hat{\mathcal{G}}^R - H.c. + (..) \quad (2.14a)$$

$$\hat{\mathcal{G}}^K(t, \omega) = F(\omega) \left( \hat{\mathcal{G}}^R(t, \omega) - \hat{\mathcal{G}}^A(t, \omega) \right) - \hat{\mathcal{G}}^R(t, \omega) \hat{\Gamma}^K(\omega) \hat{\mathcal{G}}^A(t, \omega) \quad (2.14b)$$

The terms denoted by  $(..)$  in Eq.2.14a can be dropped as their contribution is negligible for the gapped system. Now, we can write the matrix elements of adiabatic Green's function in the  $2 \times 2$  spin subspace as:

$$\hat{\mathcal{G}}_{ij}^R(t, \omega) = g_{ij}^R(t, \omega) \hat{\mathbb{1}}_2 + \vec{h}_{ij}^R(t, \omega) \cdot \vec{\sigma} \quad (2.15a)$$

and similarly, for,

$$\hat{\Lambda}_{ij}^R(t, \omega) \equiv -i\hbar \left[ \hat{\mathcal{G}} \partial_t \hat{\mathcal{H}}^c, \hat{\mathcal{G}}^R \left( \hat{\mathbb{1}} + \partial_\omega \hat{\Gamma}^R \right) \right] \quad (2.15b)$$

we can write,

$$\hat{\Lambda}_{ij}^R(t, \omega) = \rho_{ij}^R(t, \omega) \hat{\mathbb{1}}_2 + \vec{\lambda}_{ij}^R(t, \omega) \cdot \vec{\sigma} \quad (2.15c)$$

Plugging these in eq.2.14a we obtain

$$\begin{aligned} \text{Tr} \left[ \hat{G}_{ii}^K(t, \omega) \sigma^a \right] &= \text{Tr} \left[ \hat{\mathcal{G}}_{ii}^K(t, \omega) \sigma^a \right] + \sum_j \left( \Gamma_{ij}(t, \omega) \partial_t M_j^a \right. \\ &\quad \left. - \left( \vec{A}_{ij}(t, \omega) \times \partial_t \vec{M}_j \right)_a + \vec{B}_{ij}^a(t, \omega) \cdot \partial_t \vec{M}_j \right) \end{aligned} \quad (2.15d)$$

where,

$$\Gamma_{ij} = \left( \rho_{ij}^R g_{ji}^R - \vec{\lambda}_{ij}^R \cdot \vec{h}_{ji}^R + R \rightarrow A \right) \quad (2.15e)$$

$$\vec{A}_{ij} = \left( \rho_{ij}^R \vec{h}_{ji}^R - \vec{\lambda}_{ij}^R g_{ji}^R + R \rightarrow A \right) \quad (2.15f)$$

$$\vec{B}_{ij}^a = \left( \vec{\lambda}_{ij}^R h_{a,ji}^R - \lambda_{a,ij}^R \cdot \vec{h}_{ji}^R + R \rightarrow A \right) \quad (2.15g)$$

Finally, from eq.2.12 we know that the equal time Keldysh Green's function which enters the EOM eq 2.11a is obtained by performing an integral over  $\omega$  of eq.2.15d.

$$\int \text{Im} \left[ \text{Tr} \left( \hat{\mathcal{G}}_{ii}^K(t, \omega) \vec{\tau} \right) \right] d\omega \equiv \langle \vec{\sigma}_i(t) \rangle_{\{\vec{M}\}} \quad (2.16a)$$

where  $\langle \vec{\sigma}_i(t) \rangle$  is the instantaneous expectation value of the electron spin obtained under the adiabatic approximation. We further assume,

$$\int d\omega \Gamma_{ij}(t, \omega) \approx \frac{1}{\gamma_i(t)} \delta_{ij} \quad (2.16b)$$

$$\int d\omega \vec{A}_{ij}(t, \omega) \approx \frac{\alpha}{\gamma_i(t)} \vec{M}_i(t) \delta_{ij} \quad (2.16c)$$

$$[\Pi^K(t, t')]_{ij}^{ab} \approx 2D_i(t)T\delta_{ij}\delta_{ab}\delta(t - t') \quad (2.16d)$$

where  $\gamma_i$ ,  $\alpha$  and  $D_i$  are parameters, to be determined, and  $T$  is the temperature.  $\vec{B}_{ij}^a$  adds a small correction to the amplitude stiffness which has been neglected. The classical form of the noise kernel can be motivated by making a high temperature expansion of  $\Pi^K$  on the homogeneous mean-field state (Appendix B.1). The noise vanishes as  $T \rightarrow 0$  as a result of this approximation, but the actual noise survives even at zero temperature in a quantum system. The parameters  $\gamma_i$ ,  $\alpha$  and  $D_i$  may seem arbitrary as of now, but  $\gamma_i$  and  $D_i$  would be determined in terms of  $\alpha$  by imposing a couple of consistency conditions in the subsequent sections.

With these considerations, one can write a stochastic evolution equation for  $\{\vec{M}\}$ ,

$$\frac{d\vec{M}_i}{dt} - \alpha \vec{M}_i \times \frac{d\vec{M}_i}{dt} = \gamma_i(t) \left( \langle \vec{\sigma}_i \rangle_{\{\vec{M}\}} - \vec{M}_i + \vec{\xi}_i \right) \quad (2.17)$$

$$\langle \xi_i^a(t) \xi_j^b(t') \rangle = 2D_i(t)T\delta_{ij}\delta_{ab}\delta(t - t') \quad (2.17a)$$

$$\langle \vec{\sigma}_i \rangle_{\{\vec{M}(t)\}} = \int \text{Im} [\text{Tr} (\mathcal{G}_{ii}^K(t, \omega) \vec{\tau})] d\omega \quad (2.17b)$$

where  $a, b$  denote  $O(3)$  indices,  $\mathcal{G}^K$  denotes the *adiabatic* Keldysh Green's function, and the trace is over the local  $2 \times 2$  spin subspace.  $\vec{\sigma}_i = \frac{1}{2} \sum_{\alpha\beta} d_{i,\alpha}^\dagger \vec{\tau}_{\alpha\beta} d_{i,\beta}$  is the local fermion spin and  $\vec{\tau} \equiv (\tau^x, \tau^y, \tau^z)$  is the  $2 \times 2$  Pauli vector. Its average is computed on the instantaneous  $\{\vec{M}\}$  background.  $\langle \vec{\sigma}_i \rangle$  is a non-linear, non local, function of the  $\vec{M}$  field and encodes the strong correlation effects in the problem.  $\alpha$  is the dimensionless *Gilbert damping* [150, 151] parameter which provides a relaxational torque to the angular degrees of freedom,  $\gamma_i$ , which has the dimension of energy, contributes to longitudinal damping and  $D_i$  are position dependent diffusion coefficients.

As we had stated earlier,  $\gamma_i$  and  $D_i$  are not independent parameters. This can be clarified by casting Eq. 2.17 into a Landau-Lifshitz-Gilbert (LLG) form by solving for  $\frac{\partial \vec{M}}{\partial t}$ , which gives,

$$\frac{d\vec{M}_i}{dt} = A_i(t) \vec{M}_i \times \left( \langle \vec{\sigma}_i \rangle + \vec{\xi}_i \right) + B_i(t) \vec{M}_i \times \left( \vec{M}_i \times \left( \langle \vec{\sigma}_i \rangle + \vec{\xi}_i \right) \right) + \gamma_i(t) \left( \left( \langle \vec{\sigma}_i \rangle + \vec{\xi}_i \right) - \vec{M}_i \right) \quad (2.18)$$

with,  $A_i(t) \equiv \frac{\gamma_i(t)\alpha}{1+\alpha^2|\vec{M}_i(t)|^2}$  and  $B_i(t) \equiv \frac{\gamma_i(t)\alpha^2}{1+\alpha^2|\vec{M}_i(t)|^2}$ . The first term is the ‘Bloch’ term which leads to precessional motion of the spins. In order to capture the correct spin wave dispersion

$A_i = 2U$  must be satisfied, which follows from the subleading term in the strong coupling expansion of  $\langle \vec{\sigma}_i \rangle$ . This means that the time dependence in  $A_i(t)$  must drop out, which leads us to the condition,

$$\gamma_i(t) = \frac{2U}{\alpha} \left( 1 + \alpha^2 |\vec{M}_i(t)|^2 \right) \quad (2.19)$$

and hence,  $B_i = 2U\alpha$  also becomes independent of time. Hence Eq. 2.18 simplifies to,

$$\frac{d\vec{M}_i}{dt} = 2U\vec{M}_i \times \left( \langle \vec{\sigma}_i \rangle + \vec{\xi}_i \right) + 2U\alpha\vec{M}_i \times \left( \vec{M}_i \times \left( \langle \vec{\sigma}_i \rangle + \vec{\xi}_i \right) \right) + \gamma_i(t) \left( \left( \langle \vec{\sigma}_i \rangle + \vec{\xi}_i \right) - \vec{M}_i \right) \quad (2.20)$$

with  $\langle \xi_i^a(t) \xi_j^b(t') \rangle = 2D_i(t)T\delta_{ab}\delta_{ij}\delta(t-t')$ .

In the next section we shall determine the local diffusion coefficients  $D_i(t)$  in terms of  $\alpha$  by requiring *detailed balance* at equilibrium. Finally, the value of  $\alpha$  can be ascertained by evaluating Eq. 2.15f for a two site system. A tedious, but straightforward, calculation suggests  $\alpha = (U/t)^2$ . Hence, all the parameters which were introduced ‘by-hand’ get fixed upon further considerations and the final formulation does not have any free parameters. Having said that, we must note that unlike the other two parameters the value of  $\alpha$  doesn’t get fixed any consistency condition, but rather through a calculation. We shall test the sanctity of this result by benchmarking our scheme against equilibrium Monte-Carlo results in Chapter 4.

### 2.2.3 Accessing equilibrium dynamics

The Langevin scheme yields a time series for the auxiliary field  $\vec{M}_i(t)$  starting from an initial configuration which may be arbitrary. Thus the scheme allows for thermalisation of the system to the equilibrium state. However, it remains to be ascertained that the system reaches the *correct* equilibrium state, which is nontrivial, given the *multiplicative* nature of the noise. Moreover, the dissipation coefficient  $\gamma_i(t)$  and the diffusion  $D_i(t)$  not only vary over sites, but also depend on the instantaneous configuration of the auxiliary fields. Nevertheless, we shall show that even with such nontrivial parameters, the Langevin scheme converges to the *correct* long time equilibrium state. To do this we write the Fokker-Planck equation for the distribution function of the moments  $P(\{\vec{m}_i(t)\}, t) = \langle \prod_{i,a} \delta(m_i^a - M_i^a) \rangle$ .

$$\begin{aligned} \frac{\partial P}{\partial t} = -\frac{\partial}{\partial m_i^a} \cdot \left\{ \left[ \epsilon_{abc} m_i^b F_i^c + \alpha m_i^a m_i^b \left( F_i^b - T\tilde{D}_i \frac{\partial}{\partial m_j^b} \right) \right. \right. \\ \left. \left. + \frac{1}{\alpha} \left( F_i^a - T\tilde{D}_i \frac{\partial}{\partial m_i^a} - (\delta_{ab} + m_i^a m_i^b) T \frac{\partial \tilde{D}_i}{\partial m_i^b} \right) \right] P \right\} \quad (2.21) \end{aligned}$$

where the repeated indices are to be summed over, and

$$\tilde{D}_i = \frac{D_i \gamma_i}{2U} \quad (2.21a)$$



is the effective diffusion coefficient, and

$$\vec{F}_i = \langle \vec{\sigma}_i \rangle_{\{\vec{m}\}} - \vec{m}_i \quad (2.21b)$$

is a generalised force. At steady state  $\frac{\partial P}{\partial t} = 0$  leading to conservation of probability current. For the dynamics at equilibrium, the following conditions are additionally met:

- The force is *conservative*, and hence, can be derived from the spin-fermion Hamiltonian as  $\vec{F}_i = -\frac{\partial \mathcal{H}}{\partial \vec{m}_i}$ , where,

$$\mathcal{H} = \sum_{\langle ij \rangle, \sigma} t_{hop} c_{i\sigma}^\dagger c_{j\sigma} - 2U \sum_i (\vec{m}_i \cdot \vec{\sigma}_i + |\vec{m}_i|^2) \quad (2.22)$$

is the same Hamiltonian which was introduced in Eq. 2.4g if we include the classical stiffness of the auxiliary moments, and the charge field is fixed to the half-filling saddle point value.

- The distribution is given by a Boltzmann form,

$$P(\{\vec{m}_i(t)\}) \propto \text{Tr}_{el} (e^{-\beta \mathcal{H}}) \quad (2.23)$$

Using this form in Eq. 2.21, we find that the distribution becomes stationary if we assume

$$\tilde{D}_i = 1 \quad (2.24a)$$

which leads to,

$$D_i = \frac{2U}{\gamma_i} = \frac{\alpha}{1 + \alpha^2 |\vec{m}_i(t)|^2} \quad (2.24b)$$

This determines the diffusion coefficient in terms of the known parameters and the instantaneous background configuration.

Hence, we find that with a suitable choice of the dissipation and diffusion coefficients, the Langevin scheme indeed leads to the *correct* equilibrium state.

An alternative, and perhaps more intuitive approach, would be to show that the Langevin equation for the auxiliary fields maps to the well studied Landau-Lifshitz-Gilbert (LLG) equation at strong coupling. This is easy to see once we expand the electronic spin in powers of  $t/U$  in terms of the instantaneous background configuration,

$$\langle \vec{\sigma}_i(t) \rangle = \vec{M}_i(t) - \frac{J}{2U} \sum_{j \in NN} \vec{M}_j(t) \quad (2.25)$$

where  $J = 4t_{hop}^2/U$ . Substituting this in Eq. 2.20 and projecting the dynamics on the spheres

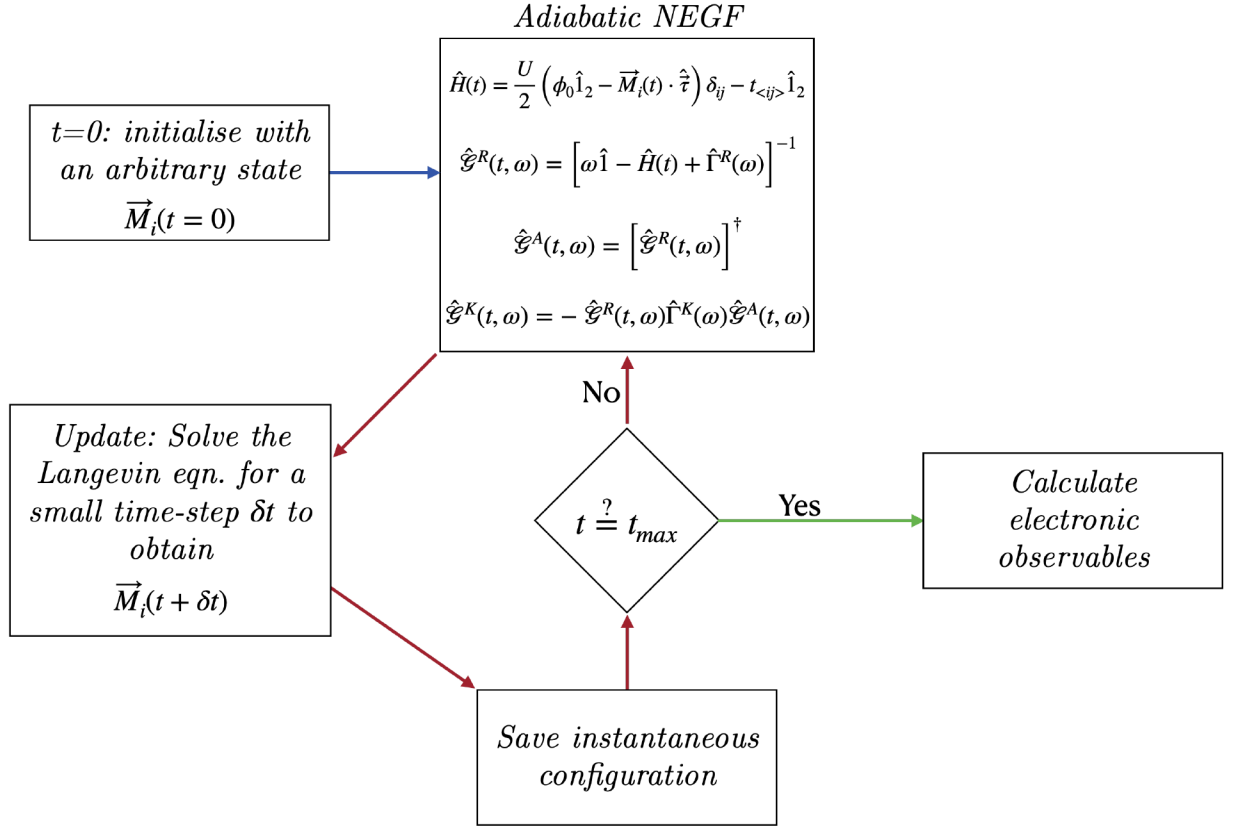


Figure 2.4: Flowchart for implementation of the Langevin scheme.  $t_{max}$  is the desired run length.

defined by  $|\vec{M}_i| = 1/2$  we get[152],

$$\frac{d\vec{M}_i}{dt} = \vec{M}_i \times (\vec{B}_i + \vec{\xi}_i) - \tilde{\alpha} \vec{M}_i \times (\vec{M}_i \times (\vec{B}_i + \vec{\xi}_i)) \quad (2.26)$$

where  $\vec{B}_i = J \sum_{i+z \in NN} \vec{M}_{i+z}$  and  $\tilde{\alpha} = \frac{3\alpha}{4} - \frac{1}{\alpha}$ . The configuration dependence of the parameters drops out. This is the celebrated LLG equation.

Thus, we find that the Langevin formulation reproduces the known limits consistently. However, in the context of Hubbard model the observable quantities are electronic correlations which can be calculated within the *adiabatic* approximation by solving the electronic problem in the instantaneous auxiliary field background. Thus, this gives us a time series for electronic operators as well, from which we can compute various static and dynamic correlators as we shall see in the next couple of sections.

### 2.2.3.1 Numerical implementation

A flowchart for the implementation of the Langevin scheme is shown in Fig.2.4 Although the noise in Eq.2.17 looks additive, it is actually multiplicative due to the torque term in the LHS. This becomes more apparent in the alternative form given in Eq.2.18. This leads to some formal problems because, for white multiplicative noise, any Langevin equation must be supplemented

by an interpretation rule to properly define it[153]. Two dominant interpretations, which lead to either the Itô or the Stratonovich stochastic calculus, are usually considered, yielding different dynamical properties for the system. Depending on the stochastic calculus used, disparate Fokker-Planck equations for the time evolution of the nonequilibrium probability distribution of the corresponding variables are obtained. It is well known that this equation reproduces Boltzmann equilibrium statistics *only if* the Stratonovich midpoint prescription stochastic calculus is used. For other kinds of time discretisations appropriate drift terms have to be added[154] to get the correct equilibrium.

We solve the above equation using a stochastic Heun discretisation scheme[155] to generate a time series for  $\vec{M}_i(t)$ . The stochastic Heun scheme converges in quadratic mean to the Stratonovich solution of Eq.2.17. Upon obtaining the time series, electronic observables are computed on the instantaneous configurations (assuming that electronic timescales are much shorter than spin fluctuation scales) and averaged over the time series.

## 2.3 Observables

In this section we discuss various observables which can be computed once we know the time series of the auxiliary fields. We shall compute the electronic observables from the instantaneous background fields under the assumption of adiabaticity, as discussed above.

### 2.3.1 Current

In a nonrelativistic fermionic system, defined in a lattice, the continuity equation for local charge conservation is given by

$$(-e)\frac{dn_i}{dt} + \vec{\nabla}_{lattice} \cdot \vec{J}_i = 0 \quad (2.27)$$

where  $n_i = c_i^\dagger c_i$  is the local charge density and  $\vec{J}_i$  is the local current density operator. For a system at steady state, the Heisenberg equation of motion for  $n_i$  is

$$\frac{dn_i}{dt} = \frac{i}{\hbar} [H, n_i] \quad (2.28)$$

where the RHS is an equal time commutator. For the Hubbard model Eq.1.2.2, this leads to

$$[H, n_i] = -t \sum_{j \in NN} (c_i^\dagger c_j - c_j^\dagger c_i) \quad (2.29)$$

The sum over nearest neighbours is the lattice divergence when the reference point is set at the site  $i$ . By comparing with Eq.2.27, we can identify  $-t (c_i^\dagger c_j - c_j^\dagger c_i)$  as the current density along the direction of nearest neighbour site  $j$  from the site  $i$ . The expectation value of the

current is

$$I_{i \rightarrow j} \equiv \langle J_{i \rightarrow j} \rangle a = -\frac{ieat}{\hbar} \left( \langle c_i^\dagger c_j \rangle - \langle c_j^\dagger c_i \rangle \right) \quad (2.30)$$

A bias voltage is usually applied by attaching leads across two ends of the sample. For the kind of systems we consider, this sets up a current along the longitudinal direction (defined by the two leads) and the transverse components (orthogonal to the longitudinal direction) of the current vanish. Furthermore, for a clean system at steady state the current along all bonds in a given direction are the same. Here, we focus only on the steady state average current of a clean system along the longitudinal direction, which, in terms of the nonequilibrium Green's functions (NEGF) is given by ( $e = a = \hbar = t = 1$ ).

$$I_{j, \rightarrow j+1}(V) = \sum_{\sigma} \int_0^{t_{max}} \frac{dt}{t_{max}} \int_{-\infty}^{\infty} \frac{d\omega}{2\pi} [\mathcal{G}_{j+1, j; \sigma}^<(t, \omega) - \mathcal{G}_{j, j+1; \sigma}^<(t, \omega)] \quad (2.31)$$

$$\mathcal{G}^<(t, \omega) = \frac{1}{2} (\mathcal{G}^K(t, \omega) + \mathcal{G}^A(t, \omega) - \mathcal{G}^R(t, \omega))$$

The adiabatic NEGFs are calculated on the instantaneous backgrounds using Eqs. 2.13c and 2.14b.

In order to stabilise the numerical computations, we need to add a small dissipation  $\eta$  at each site. This can be alternatively interpreted as weak coupling of each site in the system to noninteracting fermionic baths. Such a construction is necessary to regulate a Keldysh theory in absence of the leads, and is a part of the formulation itself, with the understanding that one should take the limit  $\eta \rightarrow 0$  at the end of a calculation. Numerically one has to work with a small  $\eta$  and ideally work in a limit where the results become independent of its value. In our calculations we find that the current conservation is sensitive to the choice of  $\eta$ , which is quite natural since a particle can escape into the bath before it reaches the other lead if the coupling to the bath is sufficiently strong. This can be avoided by choosing  $\eta$  to be much smaller than the average level spacing  $\delta$ . However choosing it to be very small may lead to ill-conditioning of the matrices during diagonalisation. We find that  $\eta \sim 0.1\delta$  is a good choice for numerical implementations. Later, we shall discuss this issue in detail.

Transport experiments measure the charge current in the leads which is the same as the longitudinal bond current defined above at steady state, if there is no leakage in the setup. By recording the current across the sample upon applying an external voltage ( $V_{source}$ ) the  $I - V$  characteristic of the sample is obtained. It is important to note that the contacts can also contribute to the measured resistance in a two terminal setup, which might lead to spurious features in the  $I - V$ . A four-probe measurement which records the voltage drop across the two ends of the sample ( $V_{sample}$ ) eliminates this problem. Experiments report both  $I - V_{source}$  as well as  $I - V_{sample}$ . We shall compare our results with  $I - V_{source}$  reported in experiments, as the voltage drop across the sample in a conducting state depends on other resistive elements in the circuits which we haven't accounted for in our theoretical models.

### 2.3.2 Density of states

The density of states (DOS) for an isolated non interacting system is given by

$$\mathcal{A}(\omega) = \frac{1}{N} \sum_n \delta(\omega - \epsilon_n) \quad (2.32)$$

where  $\epsilon_n$  is the  $n$ -th eigenvalue and  $N$  is the total number of sites. An open system cannot be ‘diagonalised’ by going to the energy basis. The presence of external dissipation necessarily leads to *broadening* of the exact eigenstates of the isolated system. A more general definition which is also applicable to open systems can be given in terms of the retarded Green’s function

$$\mathcal{A}_{ii}(\omega) = -\frac{1}{2\pi} \sum_{\sigma} \text{Im} [G_{ii,\sigma}^R(\omega)] \quad (2.33)$$

$$\mathcal{A}(\omega) = \frac{1}{N} \sum_i \mathcal{A}_{ii}(\omega) \quad (2.34)$$

where Eq.2.33 defines the local density of states (LDOS). Within the Langevin formulation, the LDOS is computed from the adiabatic retarded Green’s function  $\mathcal{G}^R(\{\vec{M}(t)\}, \omega)$  defined over the instantaneous background configuration and averaged over the time-series of  $\vec{M}_i(t)$ .

The DOS can be measured in photoemission spectroscopy (PES) while the LDOS can be measured via tunneling probes like scanning tunneling microscopy (STM). The angle resolved photoemission spectroscopy (ARPES) can measure the spectral function from which both the DOS and LDOS can be inferred.

### 2.3.3 Dynamical structure factor

The dynamical structure factor  $D_{\vec{q}}(\omega)$  correlates auxiliary fields at two different points in space and time,

$$D_{\vec{q}}(\omega) = \frac{1}{N^2} \sum_{ij} \int \frac{dt}{t_{max}} \int \frac{dt'}{t_{max}} \vec{M}_i(t) \cdot \vec{M}_j(t') e^{-i\omega(t-t') + i\vec{q} \cdot (\vec{r}_i - \vec{r}_j)} = |\vec{M}_{\vec{q}}(\omega)|^2 \quad (2.35)$$

where

$$\vec{M}_{\vec{q}}(\omega) = \frac{1}{N} \sum_i \int_0^{t_{max}} \frac{dt}{t_{max}} \vec{M}_i(t) e^{-i\omega t + i\vec{q} \cdot \vec{r}_i} \quad (2.35a)$$

and  $N$  is the total number of sites.

Inelastic neutron scattering (INS) experiments can measure the dynamical spin susceptibility  $\chi_{\vec{q}}(\omega)$  given by,

$$\chi_{\vec{q}}(\omega) = \frac{1}{N^2} \sum_{ij} \int \frac{dt}{t_{max}} \int \frac{dt'}{t_{max}} \langle \vec{\sigma}_i(t) \cdot \vec{\sigma}_j(t') \rangle e^{-i\omega(t-t') + i\vec{q} \cdot (\vec{r}_i - \vec{r}_j)} \quad (??)$$

$$= |\langle \vec{\sigma}_{\vec{q}}(\omega) \rangle|^2 + \text{vertex corrections} \quad (2.36)$$

If the vertex corrections are ignored, the dynamical spin susceptibility can be well approximated by the auxiliary field dynamical structure factor, which we demonstrate in Fig. 5.2.

### 2.3.4 Static structure factor

The time averaged auxiliary field static structure factor  $S(\vec{q})$  can be used to indicate the presence of long range magnetic order in a system. It is given by the zeroth moment of the dynamical structure factor defined above,

$$S(\vec{q}) = \int_{-\infty}^{\infty} d\omega D_{\vec{q}}(\omega) = \int_0^{t_{max}} \frac{dt}{t_{max}} |\vec{M}_{\vec{q}}(t)|^2 \quad (2.37)$$

where  $\vec{M}_{\vec{q}}(t)$  is the lattice Fourier transform of the instantaneous configuration  $\vec{M}_i(t)$ . The wavevector  $\vec{Q} = (\pi, \pi, \pi)$  is the relevant ordering vector for Néel antiferromagnetic order.  $S(\vec{q} = \vec{Q}) \sim O(1)$  indicates the presence of long range antiferromagnetic order, while  $S(\vec{q}) \sim \frac{1}{N^2}$  indicates a magnetically disordered state. We track the ordering peak of  $S(\vec{q})$  with temperature  $T$  to detect the transition from a Néel state at low  $T$  to a paramagnetic state at high  $T$ .

This maps on to the static spin structure factor of the electrons if the vertex corrections can be neglected. Experimentally the spin structure factor is an accessible quantity. The changes in magnetisation of a sample can be measured in superconducting quantum interference device (SQUID) magnetometry.

### 2.3.5 Magnetic moment distribution

The magnetic moment distribution is given by

$$P(m) = \frac{1}{N} \sum_i \int_0^{t_{max}} \frac{dt}{t_{max}} \delta(m - |\vec{M}_i(t)|) \quad (2.38)$$

For the equilibrium Mott insulator at low temperature the distribution is sharply peaked at the saturation value of the local moments ( $\sim 1$ ) and broadens on increasing temperature due to thermally induced amplitude fluctuations. This is not an experimentally accessible quantity, but it yields insight into the underlying magnetic state and is crucial in formulating effective theories, as we shall find out in Ch. 4

We have checked that the electronic moment distribution resembles the auxiliary field distribution at low temperature but gets significantly less broadened with increasing temperature in the insulating phase. The local electronic moment profile can be measured in nuclear magnetic resonance (NMR) experiments, from which the moment distribution can be inferred.

---

# Voltage driven insulator-metal transition at zero temperature

In this chapter we present our results on the mean field theory for a voltage driven insulator-metal transition (IMT) in a two dimensional Mott insulator at zero temperature. The Mott phase is realised within the single band Hubbard model. Before delving into the results we discuss the phenomenological background to the problem. We then discuss the mean-field ground state of the 2D Hubbard model and some of its features as a function of the onsite Hubbard repulsion. Finally, we discuss the nonequilibrium transport and spectral properties, and interpret our results in terms of a bias dependent length scale.

## 3.1 Background

The field driven breakdown of band insulators is well understood owing to the early work of Landau [156] and Zener [157]. In these insulators electron correlation effects are neglected and the breakdown is understood in terms of field assisted quantum tunneling of electrons across the band gap. In contrast, Mott insulators are strongly correlated, with a charge gap of many body origin due to Coulomb repulsion between electrons. The nonequilibrium physics of Mott insulators has attracted a lot of attention in recent times with both experimental [37–43, 45–57] and theoretical [69–72, 74, 75, 77, 78, 95–97, 106–121, 123, 137, 141–143] studies trying to explore the effect of the strong electron correlation on nonlinear transport in these insulators.

In most of the steady state experiments the current voltage (I-V) characteristic at low temperature has a sharp threshold voltage [37–43, 45–47]. The theory for band insulators predict that the I-V is given by the Landau-Zener (LZ) form  $I \sim V e^{-V_{th}/V}$ , with  $V_{th} \propto \Delta^2 L/W$ , where  $\Delta$  is the band gap,  $L$  is the longitudinal size and  $W$  the bandwidth of the system. The observed I-V characteristics at Mott breakdown are quite different from the LZ response, and show a sharp threshold at low temperature.



The theoretical studies broadly use two approaches: field driven and bias driven. In the field driven approach, a constant electric field is applied across the system, either by introducing a time dependent gauge field via Peierls coupling or by imposing a linear potential gradient. This has been used in the one dimensional Hubbard model to study the time-dependent Schrodinger equation [69], and also in an application of DMRG [95]. Nonequilibrium DMFT has extensively used this approach [106, 111, 115, 116]. Many of these studies find that the I-V characteristics obey the LZ form. Recently, the Hartree-Fock mean-field approach has also been used to study field driven problems. A discontinuous insulator to metal transition, along with a region of bistability, has been found within a *homogeneous* mean-field study [142]. For disordered systems, both hysteresis and filamentary conduction have been found within an unrestricted Hartree-Fock study [141].

In the bias driven setup the interacting “bulk” is coupled to non-interacting leads at the two ends. A chemical potential difference (bias) between the two leads tends to drive a current. Time dependent DMRG [97], nonequilibrium DMFT [108, 109], and a 3D time dependent Gutzwiller mean-field based study [77, 80], have used this setup. These methods impose a linear potential profile across the system, or construct a screening potential by hand [108]. Despite the assumed form for the potential the Gutzwiller method obtains spatially inhomogeneous behavior in various quantities. The current in these studies do not show the sharp voltage driven change that is observed in experiments [38–43, 45–47], and fit rather with the LZ form. A few bias driven calculations, however, do compute the internal field self-consistently and find that the breakdown process is preceded by a spatially modulated state [137, 143]. This hints that the spatial symmetry breaking due to the applied bias can promote inhomogeneous states which play a crucial role in the breakdown.

To explore this aspect, we used a Keldysh mean-field approach to study the 2D Hubbard model, at half-filling and strong interaction, connected to metallic leads. Our main finding is on the non-trivial spatial behavior of the charge and spin density in the Mott insulator as the system heads towards breakdown. We observe that there is a weakly size dependent threshold voltage  $V_c$ , of order the gap in the zero bias Mott insulator, which defines the reference scale in the biased problem. Around  $V = V_c$  the system shows crossover from exponentially small current to a high current state. The key features of this phenomenon can be captured by a bias dependent “penetration length”  $\xi(V)$ , which becomes comparable to system size as  $V \rightarrow V_c$ . We restrict ourselves to zero temperature since a model with  $SU(2)$  symmetry in one or two dimensions cannot have magnetic long-range order at finite temperature [158, 159]. A more sophisticated approach would be needed at finite temperature. Before launching into the voltage response we first discuss the nature of the  $V = 0$  state.

### 3.2 Equilibrium mean-field theory

At half-filling on the square lattice, with only nearest neighbour hopping, the ground state of the Hubbard model is an antiferromagnetic insulator (AF-I). At low  $U/t$  the magnetic order arises due to nesting of the Fermi surface, while at large  $U/t$  it is driven by nearest neighbour AF exchange. The effect is well captured within a mean field theory which starts by rewriting the interaction term as:

$$U n_{i\uparrow} n_{i\downarrow} = \frac{U}{4} (n_i)^2 - U \left( \vec{\sigma}_i \cdot \hat{\Omega}_i \right)^2 \quad (3.1)$$

with  $n_i \equiv n_{i\uparrow} + n_{i\downarrow}$  and  $\vec{\sigma}_i = \frac{1}{2} \sum_{\alpha\beta} c_{i\alpha}^\dagger \vec{\tau}_{\alpha\beta} c_{i\beta}$ , where  $\vec{\tau} \equiv \{\tau^1, \tau^2, \tau^3\}$  is the  $2 \times 2$  Pauli vector and  $\hat{\Omega}$  is an  $O(3)$  unit vector, followed by factorisation of the quadratic pieces in terms of expectation values.

$$\langle n_i \rangle = \phi_i, \quad \langle \vec{\sigma}_i \rangle = \frac{1}{2} \vec{M}_i \quad (3.2)$$

where  $\hat{M}_i = \hat{\Omega}$ . This leads to an effective mean-field Hamiltonian of the form

$$\mathcal{H}_{MF} = -t \sum_{\substack{\langle ij \rangle \\ \sigma \in \uparrow, \downarrow}} c_{i\sigma}^\dagger c_{j\sigma} + \sum_i \left( \frac{U}{2} \phi_i - \mu \right) n_i - \frac{U}{2} \sum_{i, \alpha\beta} c_{i\alpha}^\dagger \vec{M}_i \cdot \vec{\tau}_{\alpha\beta} c_{i\beta} - \frac{U}{4} \sum_i \left( \phi_i^2 - |\vec{M}_i|^2 \right) \quad (3.3)$$

where  $\phi_i$  and  $\vec{M}_i$  have to be determined self-consistently. For the periodic system, one can simplify the mean field equations by assuming the expectation values to be homogeneous.

While the ground state is an antiferromagnetic insulator (AF-I) for all values of  $U/t$  there is a qualitative difference between the  $U/t \lesssim 1$  insulator and the  $U/t \gg 1$  insulator. For  $U/t \lesssim 1$  one obtains a ‘Slater insulator’ where the charge gap is associated with the magnetic order. When  $U/t \gg 1$ , however, the charge gap (or a pseudogap) survives even when magnetic order is lost. This is the ‘Mott insulator’.

To locate the Slater to Mott crossover we used two indicators. In the first, Fig.3.1 (left panel), we compare the density of states (DOS) in the AF-I ground state with that in a ‘paramagnetic phase’ - where the moment magnitude is same as the AF-I state but the orientations are randomised. The results show that at  $U = 6t$  the loss of magnetic order still leaves a prominent pseudogap. At this  $U$  the  $V = 0$  state is a Mott insulator.

The second indicator is related to charge and spin excitation energies. The charge gap  $2\Delta$  between the upper and lower Hubbard bands at  $T = 0$  crudely defines the temperature scale  $T_{gap} \sim 2\Delta \sim U$  (at large  $U$ ) at which the DOS would become gapless. Another scale  $E_{mag}$  arises from the energy difference between the perfect AF-I state and the random orientation state. This defines the temperature scale at which magnetic order would be lost. Fig.3.1 (right panel) shows that for  $U/t = 6$  we are in a regime where  $2\Delta \gg E_{mag}$ . In fact  $2\Delta \sim U$ , while  $E_{mag} \sim t^2/U$ . Again the signature of a Mott insulator.

A full thermal theory has indeed been developed for the equilibrium problem [24–26] and recovers  $T_c$  scales consistent with Fig.3.1. See Fig.1 in [26]. We would discuss a non equilibrium

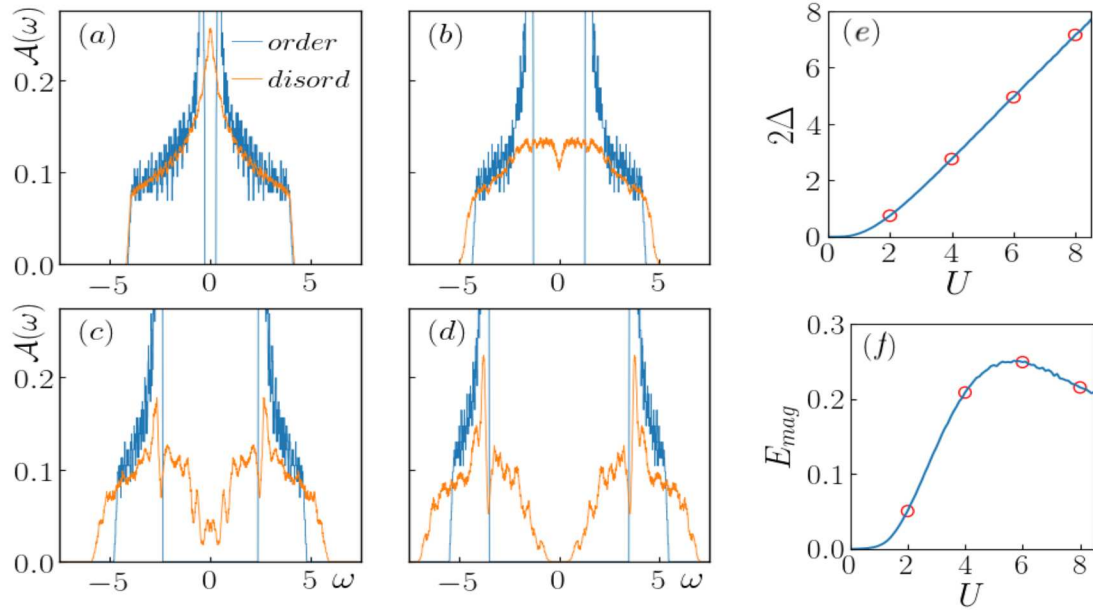


Figure 3.1: (a)-(d) Comparing the density of states in the antiferromagnetic state and the ‘paramagnetic’ phase with random moment orientations for  $U/t = 2, 4, 6, 8$  respectively. The ordered state remains gapped at all values of  $U$ . At  $U/t = 2$ , loss of order creates a gapless DOS. At  $U/t = 4$ , the ‘paramagnetic’ state is gapless but band singularities are absent. At  $U/t = 6$  there is a pseudogap, while  $U/t = 8$  shows a clean gap persisting in the ‘paramagnetic’ state. (e) Charge gap  $2\Delta$  as a function of  $U$  for the Hartree-Fock ground state at equilibrium. (f) Energy difference  $E_{mag}$  between the antiferromagnetic ground state and the ‘paramagnetic’ state with random moment orientations, as a function of  $U$ .  $E_{mag} \sim t^2/U$  at large  $U$ .

generalization of this approach in the next chapter.

### 3.3 Mean-field theory at finite bias

We uncover the following progression as the bias is increased across the Mott insulator. In our notation AF-I and AF-M are antiferromagnetic insulator and metal, respectively, and PM-M is paramagnetic metal.

1. Pre-breakdown AF-I ( $V \ll V_c$ ): In this window the charge and spin fields,  $\phi_i$  and  $M_i$ , are weakly modified near the edge, from the  $V = 0$  value. The deviation  $\delta\phi_i$  and  $\delta M_i$  decay as  $\sim e^{-R_i/\xi}$  into the bulk. There are exponential tails in the subgap density of states and a current  $I \sim e^{-V_c/V}$ .
2. Transition from AF-I to AF-M ( $V \sim V_c$ ): The lengthscale  $\xi(V)$  ‘diverges’ as  $V \rightarrow V_c$ , and the current rapidly rises over a small voltage window. The mean local moment magnitude drops sharply. Subgap peaks develop in the density of states, which gain weight with increasing  $V$ .
3. Low moment AF-M ( $V \gtrsim V_c$ ): This is a state with a large current, with small magnetic mo-

ments surviving close to the center of the system. It is an inhomogeneous antiferromagnetic metal.

4. Current saturation in PM-M, ( $V \gg V_c$ ): The spectral features and the current no longer change with voltage and the moments become vanishingly small.

Apart from the current, and the spatial behaviour of charge and spin variables, we provide detailed results on the voltage dependence of the local DOS.

We discuss the results for our implementation of the scheme in a 2D system, which is finite in the longitudinal direction, while being periodic in the transverse direction. For the conducting leads, we approximate the density of states (DOS) by a Lorentzian function.

$$\rho_{L,R}(\omega) = \left( \frac{D}{3 \tan^{-1}(\frac{3}{2})} \right) \frac{1}{\left( \omega^2 + \left( \frac{2D}{3} \right)^2 \right)} \quad (3.4)$$

Where  $D$  is the bandwidth of the bath. After integrating out the bath we retain only the diagonal terms arising from the bath Green's functions, which are proportional to the bath DOS, an approximation that is justified in the wide-bandwidth limit [137].

Unless explicitly mentioned, we have shown the results for a system with 32 sites in the longitudinal ( $x$ ) direction and 8 sites in the transverse ( $y$ ) direction. We have also studied the size dependence of our results by varying the longitudinal size from 12 to 48 sites, and the transverse size from 4 to 8 sites. The size dependence has been discussed in the relevant sections. Unless otherwise mentioned, all energies are measured in units of hopping in the system  $t_s = t = 1$ , and all currents are measured in units of  $et/\hbar$ .

### 3.3.1 I-V characteristic

The bond currents are calculated using the NEGFs as detailed in Sec. 2.3.1. Since the mean field state is static the time averaging of observables becomes trivial and the bond current between nearest neighbour sites in the  $x$  direction is given by the expression,

$$\begin{aligned} I_{j,j+1}(V) &= \sum_{\sigma} \int_{-\infty}^{\infty} \frac{d\omega}{2\pi} (G_{j+1,j;\sigma}^{<}(\omega) - G_{j,j+1;\sigma}^{<}(\omega)) \\ G^{<}(\omega) &= \frac{1}{2} (G^K(\omega) + G^A(\omega) - G^R(\omega)) \end{aligned}$$

where  $G^{R,A,K}$  are the NEGFs defined on the mean field state (Eq. 2.7b).

For the system in consideration, which has periodic boundary conditions along the transverse direction, the current is found to be the same along all longitudinal chains. Hence, the total current scales linearly with the transverse size of the system. At steady state one further expects the current to be the same on all bonds along the longitudinal axis. This has been numerically checked to be true strictly in the limit  $\eta \rightarrow 0$ . We discuss this further in Sec. 3.4.5.2.

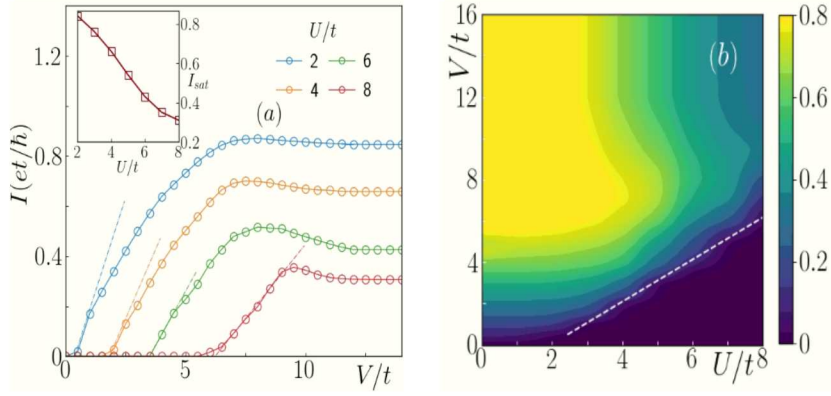


Figure 3.2: (a) The I-V characteristics for different values of interaction strength  $U$ , showing the transition from an insulating Mott state to a metallic state. The current rises sharply around a ‘critical bias’  $V_c$ , and finally saturates to a scale  $I_{sat}(U)$  when  $V \gg V_c$ . The dependence of  $I_{sat}$  on the  $U$  is shown in the inset. (b) A map of the current for varying  $U$  and  $V$ . The broken line demarcates the insulator-metal ‘phase boundary’.

For a sufficiently large system size and for  $U \gtrsim 2$  (that we have explored given our size constraints) we find that I-V characteristic has three different regions: (i) pre-breakdown, with exponentially suppressed current, (ii) breakdown - the current increases rapidly to attain its maximum value, and (iii) saturation - the current drops from the maximum to saturate at a finite value. Regime (ii) involves a transition from AF-I to AF-M, both spatially inhomogeneous, as we shall discuss later.

In Fig.3.2(a) we plot the current ( $I$ ) as a function of bias ( $V$ ) for various interaction strengths  $U$ . In regime (i), when  $V \ll V_c$ , the current  $I \sim e^{-V_c/V}$ , after which the system enters regime (ii), where the current increases rapidly, and then saturates in regime (iii) where  $V \gg V_c$ . For  $U > 2$ , and moderate sizes we encounter a region of negative differential resistance (NDR) in the I-V between the breakdown and saturation regimes. This has also been reported in other theoretical[72, 138–140] and experimental[46] studies. The existence of NDR can be attributed to the behaviour of charge field profile beyond  $V_c$ . It has a linear mean profile with modulations as shown in Fig.3.5 and further characterised in Fig.3.7. The linear mean profile  $\bar{\phi}_i$  leads to Wannier-Stark (WS) like peaks at the effective Bloch frequencies  $\omega_B = mE_{eff}$  (where  $m$  is an integer) in the density of states, as shown in Fig.3.4, while the modulations of charge fields  $\delta\phi_i$  leads to a broadening of the WS features.  $E_{eff} = U\bar{\phi}_0/L_x$  is the effective field in the system, beyond  $V_c$ . In this regime, the spin field  $M_i$  is essentially quenched near the edges, but has a finite amplitude near the center which diminishes with increasing  $V$ . This causes the local density of states at the center to develop a gap and kills the  $m = 0$  WS peak. The WS states are responsible for the NDR in the  $I - V$ , which has been documented in previous studies as well[72, 138–140]. The scattering between different WS states depends on the matrix elements of  $U\delta\phi_i$  and  $UM_i$  between the WS states. For a given  $L_x$ , they diminish at large  $V$ , beyond  $\omega_B \gtrsim U$ , and hence the  $I - V$  develops a peak at  $V_{peak}$ .

This also explains the  $U$  dependence of the NDR peak in  $I - V$ . It has also been shown that



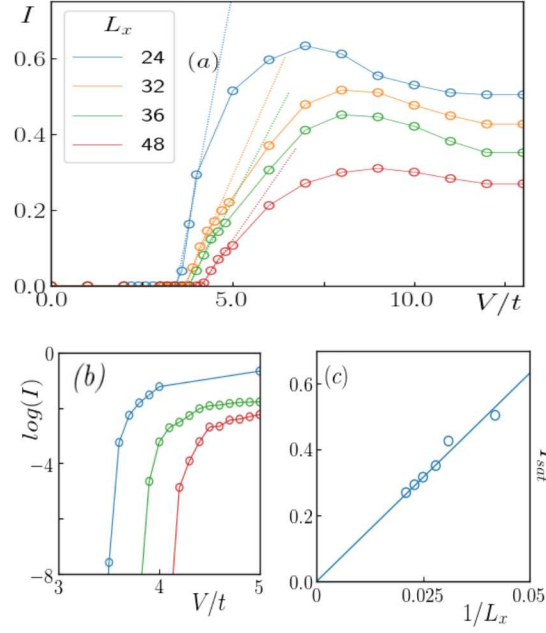


Figure 3.3: (a) Size dependence of I-V characteristics at  $U = 6$ . The current is measured in units of  $et/\hbar$ . Both the critical bias  $V_c$ , as well as the saturation current  $I_{sat}$  depend on the longitudinal size of the system. (b) The region around  $V_c$  has been plotted in log scale to highlight its size dependence. (c) Shows the dependence of  $I_{sat}$  on the longitudinal size. The data can be fitted reasonably to  $I_{sat} \propto 1/L_x$ . For a fixed  $V$  the current, and the ‘metallization’ effect in general, would vanish as  $L_x \rightarrow \infty$ .

in absence of external dissipation there is no  $dc$  component to the current at large  $V$ [139]. The auxiliary fields become independent of  $V$  for  $V$  greater than the bandwidth ( $W$ ) of the system, and we get a bath-dominated constant current in the saturation regime. One can construct a ‘phase diagram’ from the current map,  $I(U, V)$ , in Fig.3.2(b). It shows the required threshold bias as a function of  $U$  for a fixed size of the system,  $V_c(U, L_x)$ . Within our calculation we find  $V_c(U, L_x)$  to be dependent on the longitudinal size of the system. The phase diagram separates the insulating regime (i) from the metallic regimes (ii) and (iii), in the  $U - V$  plane. Note that for the square lattice, at half-filling, the ground state becomes antiferromagnetic for an arbitrarily small  $U$ , but for  $U/t \gtrsim 4$  the insulating character can survive even in the absence of magnetic order.

On studying the size dependence [Fig.3.3(a)] at a fixed value of  $U$ , one finds that the NDR feature diminishes with increasing length of the transport direction  $L_x$ , and ultimately goes away at large enough sizes. This is because for a given  $V$ , the  $E_{eff}$  reduces with increasing  $L_x$ , which lowers the energy gap between consecutive WS states, and hence pushes  $V_{peak}$  towards larger  $V$  values. With increasing  $L_x$ ,  $V_{peak}$  would cross the bandwidth  $W$ , and hence, the NDR region must disappear beyond a certain longitudinal size. The saturation current  $I_{sat}$  depends on the length of the system in the direction of transport  $L_x$  [Fig.3.3(a)]. Within our scheme the Mott insulator supports exponentially weak current at  $V < V_c(U)$  [Fig.3.3(b)], but beyond  $V_c(U)$  the current rises sharply and then reduces towards a saturation value. The size dependence of the

saturation current is shown in Fig.3.3(c).  $I_{sat} \sim 1/L_x$ , and vanishes as  $L_x \rightarrow \infty$ .

This is in contrast to the DMFT [108, 115, 116] and Gutzwiller mean field [80] studies in which the current appears to have a LZ functional form  $I \sim V e^{-\alpha/V}$ . However, we find that the low  $V$  current, although exponentially suppressed, deviates from this form. We could not derive an explicit low  $V$  form for the current due to several limitations, but a large- $N$  study[76] has suggested a form which is different from the LZ form for the low  $V$  current. However, it could not conclude whether the voltage driven breakdown is a ‘true’ transition or just a crossover. Within the limitations of our scheme we find that it is a crossover for the 1D and 2D Hubbard models connected to leads. Within our treatment, the I-V curve in these systems has a point of inflection (second derivative vanishes) at the ‘critical voltage’  $V_c$ , at which point it goes from being curved upwards to being curved downwards, while the LZ form does not have any such point. Such a point arises within our theory because the current saturates at large  $V$ , while the LZ current keeps growing linearly at large  $V$ . Within our theory, the current saturation occurs due to the finite bandwidth of system, irrespective of the bandwidth of the bath. The behaviour we observe has similarity to some experiments [37, 40].

### 3.3.2 Density of states

The overall density of states (DOS),  $\mathcal{A}(\omega)$ , is obtained by averaging the local DOS,  $\mathcal{A}_{ii}(\omega)$ , over the  $x$  direction.

$$\mathcal{A}_{ii}(\omega) = \sum_{\sigma} \mathcal{A}_{ii,\sigma} = -\frac{1}{\pi} \sum_{\sigma} \text{Im} (G_{ii,\sigma}^R(\omega)) \quad (3.5a)$$

$$\mathcal{A}(\omega) = \frac{1}{L} \sum_{i=1}^L \mathcal{A}_{ii}(\omega) \quad (3.5b)$$

At  $V = 0$  the LDOS is gapped at all sites, except for a couple of sites at the edges - which get renormalised due to coupling with the metallic baths. The sites away from the edges remain essentially unaffected in the absence of bias, as is evident in Fig.3.4(a1). Hence, the system averaged DOS at  $V = 0$ , Fig.3.4(b1), resembles that of an isolated Mott insulator, except for two subtleties:

(i) a small subgap weight shows up in the LDOS on all sites, which contributes to subgap weight which is discernible in Fig.3.4(b1). This is due to the presence of a small dissipation  $\eta$  at every site which is necessary to stabilise the numerical implementation, as we discussed in the previous section. The subgap weight at  $V = 0$  diminishes with reducing  $\eta$ .

(ii) There are additional peaks in the DOS at high energy, beyond the coherence peaks, when compared with the usual mean field DOS at the same value of  $U/t$ , shown in Fig.3.1(c). This is due to the rectangular geometry chosen where the transverse direction ( $Ly = 8$ ) is much shorter than the longitudinal direction ( $Lx = 32$ ). We have checked that those features merge into a smooth profile when the transverse size is increased to match with the longitudinal size.

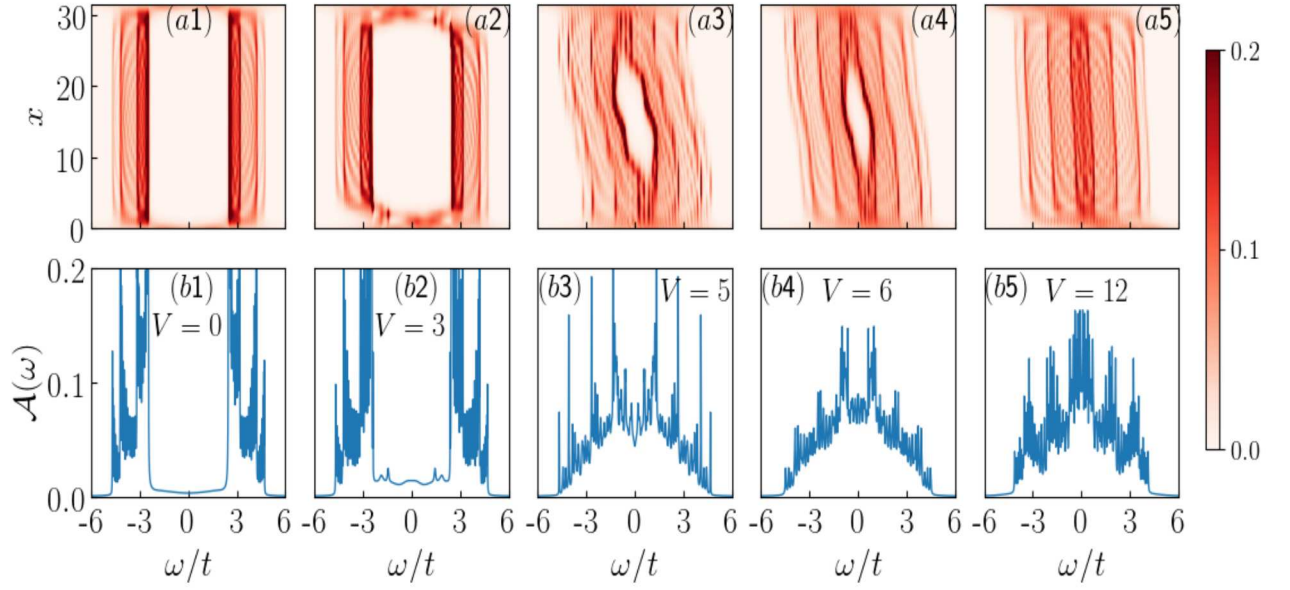


Figure 3.4: Density of states: the upper row shows the variation of local DOS  $A_{ii}(\omega, x)$  along the longitudinal direction,  $(x)$ , with changing bias at  $U = 6t$ . The panels a1-a5 are for  $V = \{0, 3, 5, 6, 12\}$  respectively. The regimes are (a1) the reference AF-I state at  $V = 0$ , (a2) AF-I at low  $V$ , (a3) AF-I to AF-M breakdown, (a4) AF-M at large current, (a5) PM-M state with current saturation. The lower row shows the behavior of the system averaged density of states with changing bias at  $U = 6t$ . Panels b1-b5 are for the same values of  $V$  as the respective panel above. The system size is  $32 \times 8$ .

At low bias  $V \ll V_c$ , in the pre-breakdown exponentially suppressed regime, the effect of bias decays exponentially inside the system, as we will see in the next section, with a ‘penetration length’ controlled by the bias. As the penetration length increases, sites progressively away from the edges start to ‘sense’ the bias and the gap in the LDOS collapses for these sites, Fig.3.4(a2). One can now find subgap states in the DOS, even though the edges in the global DOS, Fig.3.4(b2), remain sharply defined. In this regime the behaviour of the DOS can be understood, approximately, in terms of a weak site-dependent perturbation on top of a translation invariant parent state. We discuss this further in Sec.3.4.1.

After the breakdown,  $V \gtrsim V_c$ , when the current rises rapidly, all the sites feel the effect of the bias and a significant fraction of sites towards the edges become gapless, while the gap for sites at the center gets suppressed significantly [Fig.3.4(a3)]. The overall DOS [Fig.3.4(b3)] becomes gapless indicating that the fraction of ungapped sites is comparable to the gapped ones. In this regime, the gap in the LDOS shrinks with increasing  $V$  [Fig.3.4(a4)], and ultimately vanishes as we hit the saturation regime [Fig.3.4(a5)], while the DOS develops increasing weight around  $\omega = 0$ . As we move from the edge to the center of the system the LDOS remains ungapped close to the edges, develops a ‘pseudogap’ for some intermediate sites and sustains a suppressed gap close to the center even though a large current flows through the system. This can be understood from the behaviour of the charge field  $\phi_i$  and moment amplitude  $|M_i|$



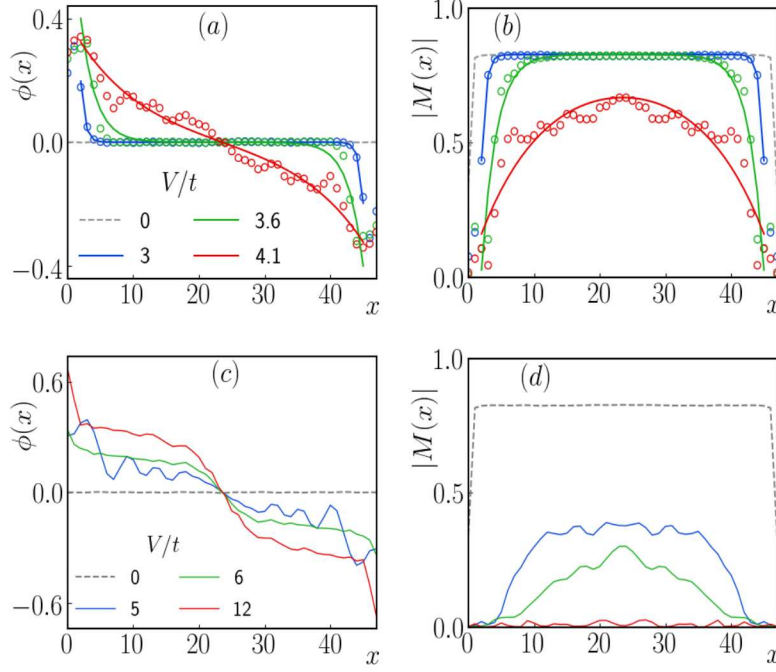


Figure 3.5: The auxiliary fields,  $\phi(x, V)$  and  $|M(x, V)|$  as a function of bias for  $U = 6t$ . Panels (a) and (b) show the spatial profile for a few values of  $V$  corresponding to the pre-breakdown regimes in the I-V curve. The open circles denote the data points, while solid lines denote fitted curves for  $\phi$  in (a) and  $|M|$  in (b) using the trial functions. The broken lines in grey denote the zero bias profiles and serve as reference. Panels (c) and (d) show the auxiliary field profiles in the post-breakdown  $V = 5, 6$  and saturation  $V = 12$  regimes. The results shown are for a  $48 \times 8$  system at  $U = 6$ .

profile beyond the breakdown, shown in Fig. 3.5(c)-(d).  $|M_i|$  become vanishingly small in a neighbourhood of the edges which leads to the collapse of the gap in the LDOS. Beyond this neighbourhood  $|M_i|$  gradually grows across a few sites, while  $\phi_i$  shows modulations above a mean profile. The small amplitude moments tend to open up a gap, while the ‘disorder’ due to modulations in the auxiliary fields smears the gap edges. Both of these effects lead to the formation of a pseudogap in the LDOS.  $|M_i|$  attains its maximum value near the center of the system, which leads to the opening of a gap. The size of this gap is significantly smaller than the  $V = 0$  gap, and it diminishes further with increasing  $V$ . This effect does not depend on the transverse direction due to translation invariance. Hence the current passes along linear channels across the system. However, nontrivial conducting paths can occur in presence of thermal or quenched disorder.

### 3.3.3 Charge and spin profiles

Within our framework the effect of the bias gets encoded in the auxiliary fields through the self-consistency. The electrons respond to the auxiliary field patterns and sense the bias through them. For the unbiased open system the charge field  $\phi$  vanishes throughout the system, whereas

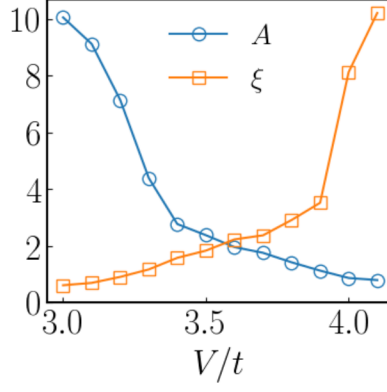


Figure 3.6: The fitting parameters - penetration length  $\xi$  and scale factor  $A$  as a function of bias  $V$ , in the neighbourhood of the voltage driven crossover for  $U = 6$ . The system size is  $48 \times 8$ .

the spin field magnitude is uniform ( $\leq 1$ ) on all sites, except for the edge sites. We have checked that the spin field alternates from site to site even at finite  $V$ .

If the bias is applied symmetrically, i.e.  $\mu_L + \mu_R = 2\mu$  condition is satisfied, then the auxiliary fields must have a specific symmetry: the charge field  $\phi_i$  is antisymmetric with respect to the center of the system, while  $|\vec{M}_i|$  is symmetric. Fig.3.5(a) and 3.5(b) (open circles) show the bias dependence of the  $\phi$  and the  $|M|$  fields in the pre-breakdown regime at  $U = 6t$ . Till close to  $V_c$  the effect of the bias remains confined to the edges. In this regime, we obtain a “mean profile” for the auxiliary fields by fitting them with the trial functions:

$$\phi_{tr}(x) = A \left( e^{-x/\xi} - e^{-(L_x-x)/\xi} \right) \quad (3.6a)$$

$$M_{tr}(x) = \left( M_0 - A \left( e^{-x/\xi} + e^{-(L_x-x)/\xi} \right) \right) \times \cos(\pi x) \quad (3.6b)$$

where  $L_x$  is the length in the longitudinal direction.  $M_0$  is the mean-field moment size for the translation invariant system. The bias dependence of the deviation fields enters through the parameters  $A$  - an overall scale factor, and  $\xi$  - the penetration length. The fitted curves for  $\phi$  and  $|M|$  have been plotted using solid lines in Fig.3.5(a) and 3.5(b).

Fig.3.6 shows the bias dependence of fitting parameters. For  $V \ll V_c$  the effect of bias remains localized to the edges and  $\phi$  and  $|M|$  decay exponentially within a few sites from the edges. As  $V$  approaches  $V_c$  the effect of bias penetrates deeper, indicated by the rapidly rising penetration length for both the fields. Once the penetration length attains a significant value, the entire system senses the effect of bias and the current rises rapidly. Across the transition  $\xi$  grows continuously by almost an order of magnitude. The scale factor  $A$  falls rapidly before the transition and then saturates to unity beyond the transition, for all system sizes. Hence, in terms of the ‘deviation fields’ the Mott breakdown can be visualised as a transition from a strong deviation close to the edges to a system wide effect near the transition.

Beyond  $V_c$  the fields show a spatial modulation on top of a mean profile, as is evident in Fig.3.5(c) and 3.5(d). The modulations tend to die off as one approaches the saturation regime. In

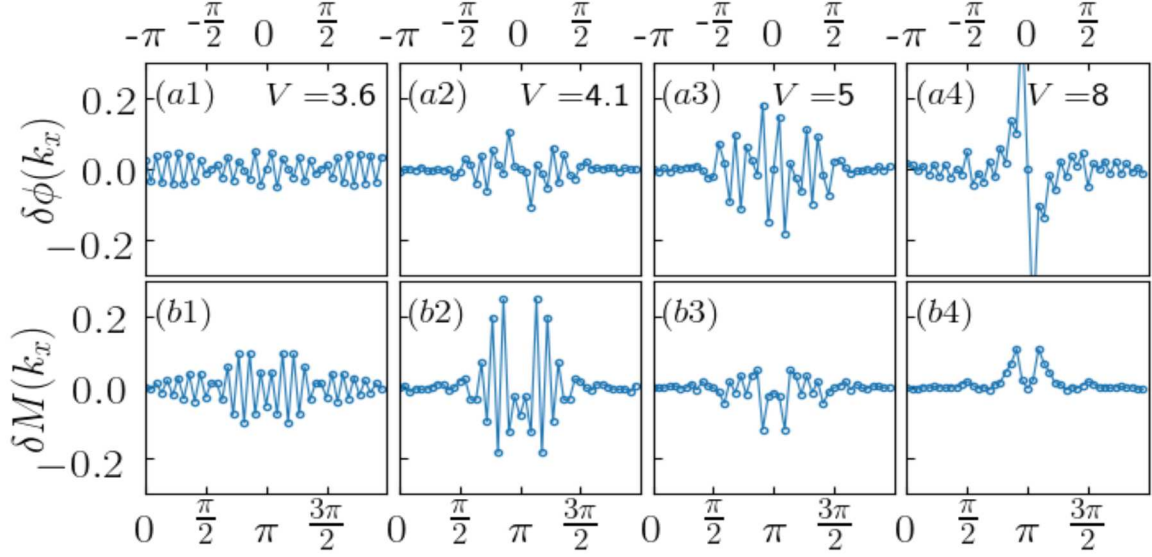


Figure 3.7: Fourier content of the auxiliary field modulations at  $U = 6t$  plotted for different  $V$ . The upper panels show the Fourier transform of  $\delta\phi(x) = \phi(x) - \phi_{tr}(x)$ , while the lower panels show the Fourier transform of  $\delta M(x) = M(x) - M_{tr}(x)$ . Voltages are  $V = \{3.6, 4.1, 5, 8\}$  from left to right columnwise. As  $V$  increases across the transition, the interval containing the dominant modes shrinks to a narrow interval around  $k_x = 0$  for  $\delta\phi(k_x)$  and  $k_x = \pi$  for  $\delta M(k_x)$  respectively.  $L_x = 48$  for the plot shown.

this regime the mean  $\phi$  acquires a linear profile while the mean  $|M|$  becomes vanishingly small. In order to analyse the mode content on top of the mean profiles we subtract out the mean curve and then Fourier analyse the modulating fields  $\delta\phi(x)$  and  $\delta M(x)$  in the longitudinal direction, Fig.3.7. Before breakdown the auxiliary field profiles are dominated by the mean curves and hence, the Fourier profiles of the deviations are vanishingly small. Even for  $V \lesssim V_c$ , Figs.3.7(a1) and (b1), one finds that the Fourier weights are small and evenly spread over the entire  $k$  range. For  $V \approx V_c$ , Figs.3.7 (a2), (b2) and (a3),(b3), the dominant weights lie in an interval of  $\pm\frac{\pi}{2}$  around the  $k = 0$  mode  $\phi$  and  $k = \pi$  mode for  $M$ . As  $V$  increases beyond  $V_c$ , the interval containing the dominant modes progressively shrinks. At  $V \gg V_c$ , Figs.3.7 (a4) and (b4), the Fourier profile is dominated by a few modes in the vicinity of  $k_x = 0$  and  $\pi$  for the charge and spin fields respectively. As noted in ref. [137], we find that spatially modulated patterns arise in the auxiliary fields as the system metallizes, indicating that the system is susceptible to pattern formation. We emphasize that the transition itself is not driven by these patterns but by the suppression of the magnetic moments through the bulk of the system. In principle, one should be able to provide a Ginzburg-Landau description for the effect of bias on the auxiliary fields. Such a description would be a valuable aid to our understanding, since all other properties of the system can be inferred from the behaviour of the auxiliary fields. However, such a description could not be established despite numerous attempts and needs further effort.

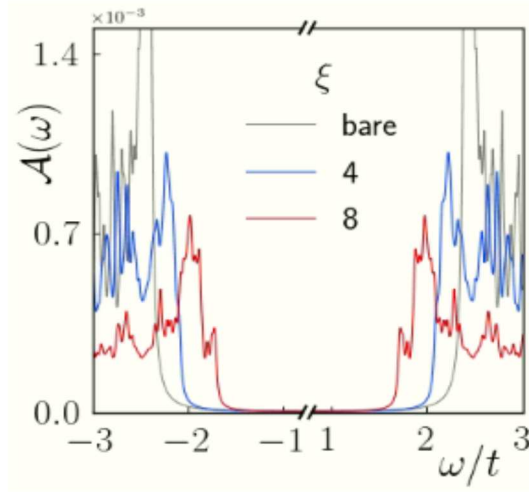


Figure 3.8: The perturbatively corrected DOS, in the pre-breakdown regime for different values of  $\xi$  keeping  $A$  fixed at 1.5. The gap reduces with increasing  $\xi$ .

### 3.4 Discussion

In what follows discuss an approximate method for accessing the  $V$  dependence of spectral features, touch upon the nature of the 2D IMT and the large bias state, and discuss some of the numerical issues related to our computation.

#### 3.4.1 Spectrum at finite bias

We set up a perturbative calculation which captures the gap renormalisation in the global DOS at finite bias,  $V \ll V_c$ . In this regime, the deviation of the auxiliary fields from the translation invariant background profile is small, and one can treat the deviation fields  $\delta\phi$  and  $\delta M$  within perturbation theory. In this, we neglect the contribution coming from renormalisation of the local DOS at the edges due to the hybridisation with the leads. This is justified because the edge contribution to the global DOS is suppressed by a factor of  $1/L_x \ll 1$ . Under these assumptions, the bare problem becomes analytically tractable. One can obtain the bare DOS by diagonalising a  $2 \times 2$  Hamiltonian in momentum space. The deviation fields:

$$\delta\phi(x) = Ae^{-L/2\xi} \left( e^{(\frac{L}{2}-x)/\xi} - e^{-(\frac{L}{2}-x)/\xi} \right) \quad (3.7a)$$

$$\begin{aligned} \delta M(x, y) &= -Ae^{-L/2\xi} \left( e^{(\frac{L}{2}-x)/\xi} + e^{-(\frac{L}{2}-x)/\xi} \right) \\ &\quad \times \cos(\pi x + \pi y) \end{aligned} \quad (3.7b)$$

are treated within perturbation theory. We compute the second order self energy corrections to the bare DOS and show, in Fig.3.8, that for a fixed  $A$ , the gap in the spectrum decreases with increasing  $\xi$ . The details of the calculation are provided in Appendix A.2.



---

### 3.4.2 Nature of the transition

Most experiments on the bias driven insulator-metal transition show (i) a first order jump from the insulating to the conducting state on increasing bias, (ii) a hysteretic response to bias cycling, and (iii) a seemingly growing current, an ‘ohmic response’, as the bias is increased past breakdown. We do not see these in our results at  $U = 6t$  so some clarification is in order

The I-V curves for the bias driven insulator-metal transition, within this study, grow smoothly across  $V_c$ , from an exponentially suppressed current state to high current state. The transition within our *inhomogeneous* mean field study does not require the magnetic order parameter to vanish throughout the system, rather it is driven by a ‘penetration length’ becoming comparable to system size - with moments still surviving in the center of the system. This is specific to low spatial dimensions - 1D and 2D, and unlike the scenario reported in Ref. [142], where the system undergoes a discontinuous transition with respect to the applied field. This crucial difference might be due to the assumption of a uniform order parameter in that study. However, a 3D generalisation (to be discussed in the next chapter) of this method yields I-V characteristics in which the current switches discontinuously between the two regimes. There we also find hysteresis with respect to upward and downward voltage sweeps. This is the scenario reported in most of the experiments [37–43, 45–47] on voltage driven Mott insulators.

### 3.4.3 The large bias state

Within our scheme the current saturates at large values of bias since the current kernel is bounded by the bandwidth of the bath-connected system. Increasing  $V$  beyond this scale does not have any effect on the current. The range of  $V$ , post-breakdown, for which the current keeps growing depends on the ratio of gap ( $\Delta$ ) to the bandwidth ( $W$ ). For example, in Fig.3.2(a), for  $U/t = 2$  we have  $\Delta/W \approx 10$ , and one needs to apply a bias which is ten times larger than the breakdown voltage to find current saturation. This might be the scenario for most experiments [37–43, 45–47] where they do not report saturation upto  $V \sim 2V_c$ .

### 3.4.4 Quantum fluctuations and long range Coulomb effects

In this chapter we found that a mean field theory successfully captures the bias driven insulator to metal transition in the 2D Hubbard model. However, due to neglect of fluctuations, it may not predict the correct transition scales. In the  $V \sim V_c$  regime, where the local moments are still large at the center, while those near the edges get completely quenched, quantum fluctuations might significantly alter the parent state. The long range Coulomb interaction, as considered in Ref.[143], should also play a significant role in this regime. It would redistribute the charges accumulating at the edges into a more uniform profile. Overall, it is very likely that incorporating quantum fluctuations and long range Coulomb effects would not only reduce the critical voltage, but may also change the nature of the transition, inducing a discontinuous change from insulating

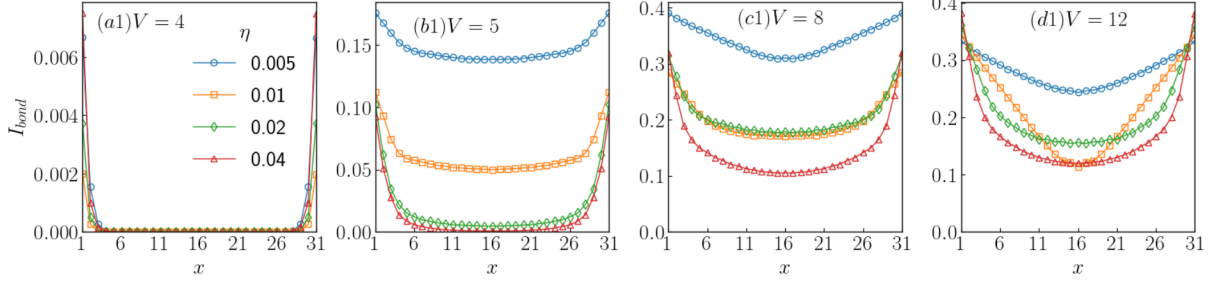


Figure 3.9: (a1)-(d1)  $\eta$  dependence of bond currents across the system for various voltage ( $V$ ) values.  $\eta$  must be chosen to be much smaller than the average level spacing  $\delta$  ( $\sim 0.02$  for a  $32 \times 8$  system) to avoid gross violation in current conservation across the system.

to metallic state as one tunes the voltage.

### 3.4.5 Numerical checks

#### 3.4.5.1 Size dependence

Our problem is formulated explicitly for a finite sized system. For a fixed  $V$ , if one takes  $L_x \rightarrow \infty$  one does not expect to see a breakdown since the field inside the system vanishes. We have studied the size dependence of the  $I(V)$  character in Fig.3.3. The gross features in the DOS, namely the gap and the bandwidth, are less sensitive to longitudinal size variation. The fit of the auxiliary field profiles with the trial functions suggested in Eq.3.6(a) and (b) systematically improves with increasing longitudinal size. Moreover the penetration depth,  $\xi$  rises more sharply around  $V_c$  with increasing  $L_x$ . The transverse size  $L_y$  does not have any effect on the auxiliary field profiles.

#### 3.4.5.2 $\eta$ dependence and frequency discretisation

In order to stabilise the Schwinger-Keldysh action, even for an isolated system, one needs to work with a small, but finite  $\eta$ . Microscopically, this can be interpreted as slight broadening of exact eigenlevels due to weak coupling with the environment. In a numerical implementation,  $\eta$  should be chosen to be as small as allowed by numerical stability, and certainly smaller than the average level spacing. We find that the choice of  $\eta$  can affect the results significantly.

Fig.3.9 shows the effect of  $\eta$  on current conservation across the system. Current conservation is grossly violated unless  $\eta$  is chosen to be much smaller (an order of magnitude) than the average level spacing  $\delta \sim 0.02$ , for a  $32 \times 8$  system. Moreover, for  $\eta \gtrsim \delta$ , the transition itself gets ‘smeared’, with local moments surviving in the metallic phase even in the saturation regime. Hence,  $\eta$  has been chosen an order of magnitude smaller than  $\delta$  and we have ensured that reducing it further does, within the numerically accessible range, does not affect our results.

The choice of  $\eta$  also dictates the frequency discretisation  $\Delta\omega$ , as one must satisfy the condition  $\Delta\omega \ll \eta$  in order to satisfy the DOS sum rules. This forces us to work with a very large frequency

---

grid  $\sim 5 \times 10^3$ .

### 3.5 Conclusion

We have studied the breakdown of a two dimensional antiferromagnetic Mott insulator in response to a voltage bias, using Keldysh mean field theory at zero temperature. We obtained the current-voltage characteristics for a finite sized system and studied its size dependence. The I-V results which we obtain show a threshold behaviour, unlike those obtained from dynamical mean field theory studies. We studied the variation of the local density of states in the longitudinal direction in response to the bias. The LDOS changes from ‘gapped’ to ‘ungapped’ as one moves from the center to the edge at  $V < V_c$ , with the fraction of ‘ungapped’ sites increasing as one heads towards  $V_c$ . These effects emerge due to the progressive ‘penetration’ of the applied bias into the bulk over a lengthscale  $\xi(V)$ , which grows to system size near the critical bias. All response functions can be calculated, approximately, based on a knowledge of this lengthscale. The results emphasize the role of spatial symmetry breaking due to the applied bias, and the need for a real space treatment of the resulting problem. Our method readily generalizes to disordered and frustrated Mott systems.

## Nonequilibrium response of the Mott insulator at finite temperature

In the last chapter we discussed the voltage driven breakdown of a two dimensional (2D) Mott insulator at zero temperature. The transport characteristics showed a sharp *crossover* from an insulating to a metallic state across a voltage  $V_c$ , and the essential physics could be attributed to a voltage dependent length scale  $\xi$  which is responsible for penetration of the effects of bias from the edges to the center of the system. It also motivated pattern formation accompanying the insulator-metal transition. However, as with any mean field theory, it neglected fluctuations of the auxiliary fields. This is particularly debilitating in the study of Mott systems, which usually have magnetically ordered ground states and undergo a thermally driven magnetic transition driven by angular fluctuations of the magnetic order parameter. Mean field theory fails to capture this entirely, and thus cannot be reliably compared with experiments which often explore the voltage driven insulator metal transition with varying temperature.

Moreover, as we discussed in Sec.1.3.1, several experiments in Mott insulators reveal a *discontinuous* current-voltage characteristic along with hysteresis. One also observes a strong temperature dependence in the current response. While the actual experimental scenario might be very complicated due to the presence of multiple orbitals in real materials and the coupling of lattice degrees of freedom with the electrons, in this chapter, we explore the interplay of magnetism and nonequilibrium charge transport in Mott insulators by studying the three dimensional (3D) Hubbard model at finite temperature in the presence of a voltage bias.

A 3D system is considered because there is no real magnetic transition in lower dimensions for the systems we study. Although a finite sized calculation in lower dimensional systems may reveal an apparent ‘transition’, the results become strongly size dependent and the ‘transition’ does not survive in the thermodynamic limit. We also neglect the effects of lattice and multiple orbitals in this study, which must be built-in if a quantitative comparison with experiments has to be made. We use the effective Langevin scheme introduced in Chapter2, which incorporates thermal fluctuations of the magnetic auxiliary field that is used to decouple the Hubbard interaction.



---

Before going into the results, we discuss the background to this problem in the next section.

## 4.1 Background

Strongly correlated systems driven out of equilibrium define a frontier in condensed matter. Experiments have probed the response to large bias in Mott insulators [36–43, 45–48], explored ‘pump-probe’ phenomena where a material is subjected to an intense pulse of radiation [55–57], and revealed metastable hidden phases [11–15]. Among these, the voltage biased Mott insulator is widely studied due to the well understood equilibrium state and the occurrence of a bias driven insulator-metal transition (IMT). The breakdown of the ‘collectively localised’ Mott state is expected to be very different from that of a band insulator.

Experiments across multiple materials suggest that the current-voltage (I-V) characteristic across the bias driven transition has a common form [38–43, 45]. These include (i) a low temperature hysteresis in the current with respect to voltage sweep - changing abruptly from low current to high current at some voltage  $V_c^+$  on the upward sweep, and showing the reverse switching at  $V_c^- < V_c^+$  on the downward sweep, and (ii) reduction of  $V_c^\pm$  and also  $\Delta V_c = V_c^+ - V_c^-$  with increasing temperature, with hysteresis vanishing above some temperature  $T^*$ . These features have been observed in samples of nanometer size [42] to millimeter size [41].

Multiple theories have tried to model the voltage induced breakdown [69, 95, 97, 104, 108–111, 116, 120, 137, 141–146, 160–165]. Most microscopic approaches suggest a Landau-Zener (LZ) like mechanism [69, 95, 97, 109, 116]. The resulting I-V characteristic fails to capture the discontinuous nature of breakdown, and the strong temperature dependence observed in a wide variety of compounds. Phenomenological network models invoking the ideas from percolation [160, 161] capture the low  $V$  transport for some materials but their applicability in the strongly nonequilibrium state remains uncertain. It is only for narrow gap “dirty” Mott insulators, with in-gap states, that a successful theory [162] based on ideas of Frohlich [163–165] seems to be available. In our understanding the limitations for strong coupling systems arise from (i) the neglect of spatial symmetry breaking (due to the bias), (ii) the difficulty in accessing the long time, steady state, current, and (iii) ignoring the magnetic order that occurs at low temperature.

This chapter addresses the whole set of issues using a scheme that is non perturbative in both the interaction strength and the applied bias and only exploits the “slowness” of the magnetic fluctuations on electronic timescales. Our Keldysh based Langevin equation approach retains the effects of dissipation channels (the leads), the applied bias, strong interaction, and thermal fluctuations, and yields the nonequilibrium electronic state at long times. The approach is a ‘twofold’ generalisation of the standard magnetic mean field theory of the Hubbard model: (i) at zero temperature ( $T = 0$ ) we get a Keldysh mean field theory for magnetism in the biased open system, while (ii) at finite temperature a ‘thermal noise’ generates magnetic fluctuations in the driven system. The result is a stochastic evolution equation for the magnetic moments  $\vec{M}_i(t)$  (see later) which define the background for electron physics.

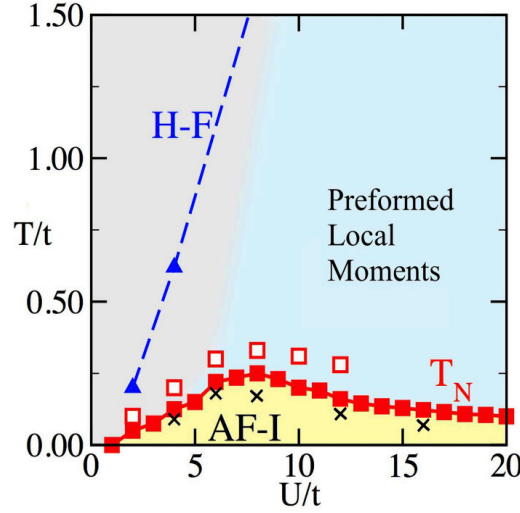


Figure 4.1: Equilibrium phase diagram of the 3D Hubbard model in the temperature  $T/t$  vs interaction strength  $U/t$  plane, where  $t$  is the hopping strength. The solid red squares show dependence of the Néel temperature  $T_N$  on  $U/t$ , as obtained from a classical auxiliary field Monte-Carlo method on  $4^3$  clusters. The AF-I region denotes the Néel antiferromagnetic phase and insulating characteristics. The open squares are the  $T_N$  obtained from a DQMC method (Ref.[166]). The light blue region depicts the preformed local moment regime which is a paramagnetic insulator phase. The dashed line shows the  $T_N$  obtained from Hartree-Fock theory and the gray region denotes the paramagnetic metal phase. Taken from Ref.[26]

## 4.2 Physics at equilibrium

The equilibrium physics of the Hubbard model at half-filling on a cubic lattice has been studied using various Monte Carlo techniques. Although the numerically exact quantum Monte Carlo (QMC)[166] sets the benchmark, a much simpler approximate technique, the static path auxiliary field classical Monte Carlo[26], can capture the not only the phases correctly but also gets the transition scales to a good accuracy.

Within the static path approximation (SPA), the Hubbard model is mapped to a non-interacting problem of tight-binding electrons coupled to background static auxiliary fields which are classical. The auxiliary fields are sampled using an exact diagonalisation based classical Monte Carlo to get the finite temperature equilibrium ensemble. The observables can be calculated by diagonalising the electronic Hamiltonian for each background configuration and averaging over the configurations.

The half-filling phase diagram within SPA, and its comparison with QMC is shown in Fig.4.1. For any finite  $U/t$  the ground state is an antiferromagnetic insulator (AF-I). At temperature  $T = 0$  the magnetic moment per site grows with increasing  $U$  and saturates to  $1/2$  as  $U/t \rightarrow \infty$ . As the temperature is increased the system loses long range order (LRO) at a scale  $T_N(U)$ . Beyond  $T_N$ , the system is a paramagnetic metal (PM) for  $U \lesssim 4t$  and a paramagnetic insulator (PI) for  $U \gtrsim 4t$ . The crossover region from PM to PI shows a pseudogapped density of states (DOS) [26].

To illustrate this we plot the thermally averaged single particle density of states, given by Eq.2.32, for  $U = 6t$  in Fig.4.2(a). It shows a crossover from a gapped state at low temperature to a pseudogapped state beyond  $T_{pg} = 0.2t$ . Fig.4.2(b) shows the optical conductivity with varying temperature. A Drude weight develops in the optical spectrum as the system undergoes a crossover to the pseudogap phase.

The resistivity ( $\rho$ ) is defined as[167],

$$\rho = \frac{1}{\sigma_{dc}}, \text{ where} \quad (4.1)$$

$$\sigma_{dc} = \frac{1}{\Omega} \int_0^\Omega d\omega \text{Re} [\sigma^{xx}(\omega)] \quad (4.2)$$

$$\sigma^{xx}(\omega) = \frac{1}{N} \sum_{mn} \frac{e^{-\beta E_n} e^{-\beta R_m}}{Z (E_m - E_n)} \frac{|\langle n | j_x | m \rangle|^2}{\omega + i\eta - (E_m - E_n)} \quad (4.3)$$

where  $\sigma^{xx}(\omega)$  is the longitudinal optical conductivity and  $\Omega$  is a small cutoff in energy which has been taken to be  $0.5t$ .  $j_x$  is the current operator defined in Eq.2.30,  $\beta$  is the inverse temperature  $Z$  is the partition function and  $N$  is the number of sites in the system.  $|m\rangle, |n\rangle$  are single-particle eigenstates obtained by diagonalising the electron problem in the auxiliary field background, and the results are averaged over the auxiliary field configurations. Fig.4.2(c) shows the variation of  $\rho$  (in log scale) with inverse temperature. The straight line fit demonstrates that it follows a form  $\rho = \rho_0 e^{\Delta/T}$ , where  $\Delta$  is the  $T = 0$  gap in the DOS, up to the pseudogap temperature  $T_{pg}$ .

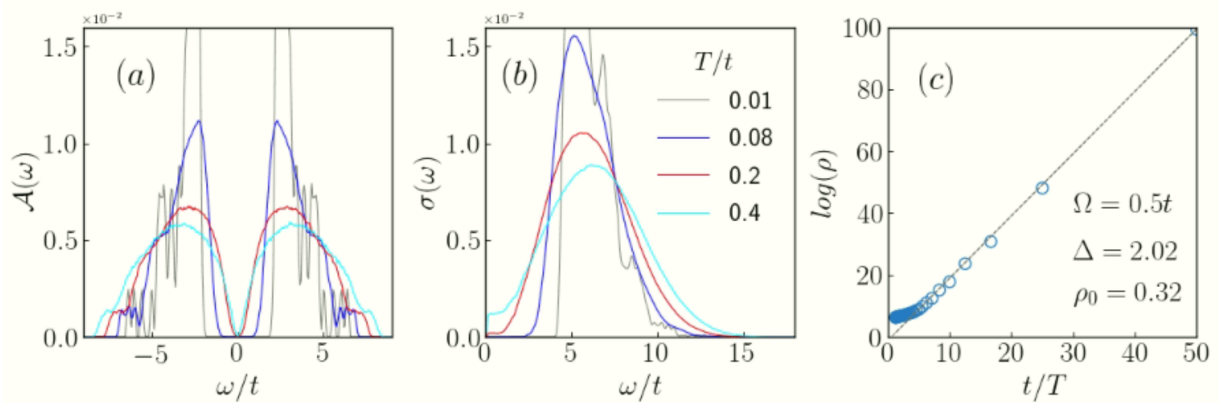


Figure 4.2: Results for equilibrium 3D Hubbard model at  $U/t = 6$ . (a) The variation of the single particle density of states (DOS) with temperature. The charge gap reduces with increasing temperature and crosses over to a pseudogap at  $T = 0.2t$ . (b) The variation of optical conductivity with temperature. A Drude weight appears in the optical spectrum as the system undergoes the pseudogap crossover. (c) Dependence of the logarithm of resistivity on inverse temperature. The data above the pseudogap crossover ( $t/T = 5$ ) fits well with a straight line having slope equal to the zero temperature single particle gap  $\Delta$  and intercept  $\log(\rho_0)$ .  $\Omega$  is the energy cutoff used to calculate the d. c. conductivity (unpublished).

### 4.3 Effective Langevin equation

We consider the repulsive 3D Hubbard model in a finite geometry, connected to leads along the long direction. We recapitulate the Hamiltonian introduced in Eq.2.1

$$\begin{aligned}
\mathcal{H} &= \mathcal{H}_{sys} + \mathcal{H}_{bath} + \mathcal{H}_{coup} \\
\mathcal{H}_{sys} &= -t_s \sum_{\langle ij \rangle} \sum_{\sigma} \left( d_{i\sigma}^{\dagger} d_{j\sigma} + h.c. \right) + U \sum_i n_{i\uparrow} n_{i\downarrow} - \mu N \\
\mathcal{H}_{bath} &= \sum_{\nu} \sum_{\beta \in \{L, R\}} (\epsilon_{\nu} - \mu_{\beta}) c_{\nu}^{\dagger \beta} c_{\nu}^{\beta} \\
\mathcal{H}_{coup} &= - \sum_{\langle ij \rangle, \sigma} v_{ij} \left( c_{i\sigma}^{\dagger L} d_{j\sigma} + c_{i\sigma}^{\dagger R} d_{j\sigma} + h.c. \right)
\end{aligned}$$

where  $t_s$ ,  $\mu$  and  $U$  are the nearest-neighbour hopping amplitude, chemical potential and onsite Coulomb repulsion strength in the system, respectively.  $\epsilon_{\nu}$  are the eigenenergies and  $\mu_{\beta}$  are the chemical potentials in the conducting leads, where  $\beta = (L, R)$ , with  $L$  denoting the left lead and  $R$  the right lead.  $\mu_{L,R} = \mu \pm (V/2)$ ,  $V$  being the applied bias.  $v_{ij}$  denotes the system-bath coupling matrix.

Starting from the complex time Keldysh action for the above Hamiltonian we decouple the quartic term by performing a Hubbard-Stratonovich transformation. This introduces real auxiliary fields at each instant, which couple to the instantaneous density and spin of the electrons - henceforth called the charge field  $\phi_i(t)$  and spin field  $\vec{M}_i(t)$  respectively. The action becomes quadratic in the fermionic fields which can be formally integrated out. We fix the charge field at it's equilibrium saddle point value. Using assumptions related to the slowness of the  $\vec{M}_i(t)$ , and a simplified noise kernel, both discussed in Chapter2, we arrive at the stochastic dynamical equation for  $\vec{M}_i(t)$ , which we reproduce here for completeness,

$$\frac{d\vec{M}_i}{dt} - \alpha \left( \vec{M}_i \times \frac{d\vec{M}_i}{dt} \right) = \gamma_i(t) \left( \langle \vec{\sigma}_i \rangle_{\{\vec{M}\}} + \vec{\xi}_i - \vec{M}_i \right) \quad (4.4a)$$

$$\langle \xi_i^a(t) \xi_j^b(t') \rangle = \frac{4T}{U \gamma_i(t)} \delta_{ij} \delta_{ab} \delta(t - t') \quad (4.4b)$$

$$\langle \vec{\sigma}_i \rangle_{\{\vec{M}(t)\}} = \int \text{Im} [\text{Tr} (\mathcal{G}_{ii}^K(t, \omega) \vec{\tau})] d\omega \quad (4.4c)$$

where  $\gamma_i(t) = \frac{2U}{\alpha} (1 + \alpha^2 |\vec{M}_i(t)|^2)$ .  $a, b$  denote  $O(3)$  indices,  $\mathcal{G}^K$  denotes the *adiabatic* Keldysh Green's function, and the trace is over the local  $2 \times 2$  spin subspace.  $\vec{\sigma}_i = \frac{1}{2} \sum_{\alpha\beta} d_{i,\alpha}^{\dagger} \vec{\tau}_{\alpha\beta} d_{i,\beta}$ ,  $\vec{\tau} \equiv (\tau^x, \tau^y, \tau^z)$  being the  $2 \times 2$  Pauli vector, is the local fermion spin. Its average is computed on the instantaneous  $\{\vec{M}\}$  background.  $\langle \vec{\sigma}_i \rangle$  is a non-linear, non local, function of the  $\vec{M}$  field and encodes the strong correlation effects in the problem.

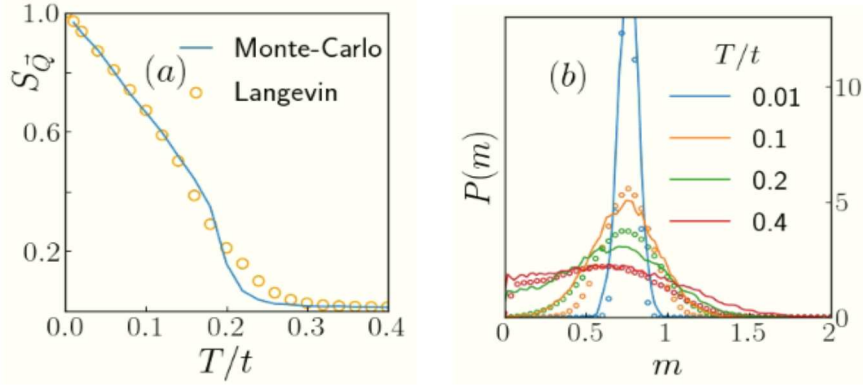


Figure 4.3: (a) Comparison of temperature dependence of the structure factor peak with equilibrium ‘classical’ Monte Carlo. The Néel temperature  $T_N = 0.22t$  at  $U = 6t$ . The two curves coincide, except very close to  $T_N$ . (b) Comparison of moment distribution for different temperatures. The distributions match at low temperature and somewhat deviate near  $T_N$ .

## 4.4 Benchmarks

As discussed in Sec.2.2.2.2, a toy calculation on a 2-site system suggests  $\alpha = (U/t_{hop})^2$ . We check this by benchmarking the scheme against classical auxiliary field Monte-Carlo results at equilibrium. We compare the temperature dependence of the structure factor (Sec.2.3.4) peak across the two formulations, in Fig.4.3(a). The MC predicts a magnetic transition at  $T_{MC} = 0.22t$ , which is also reproduced by the Langevin scheme. The two curves coincide for almost the entire range of temperature. The magnetic transition temperature within QMC is about  $0.25t$ .

We also compare the moment magnitude distribution, defined in Sec.2.3.5, at different temperatures in Fig.4.3(b). The distributions match at low temperature, but slightly deviate for close to the transition temperature.

## 4.5 Results at finite bias

The results presented here pertain to a  $8 \times 4 \times 4$  system, with  $L = 8$  being the longitudinal (transport) direction. Starting with an arbitrary  $\{\vec{M}\}$  configuration the system is evolved for  $\sim 10^6$  steps with a time discretisation of  $10^{-3}\tau_0$ , where  $\tau_0 \sim 1/J_{eff}$ , with  $J_{eff} \sim \frac{t^2}{U}$ , is the characteristic timescale of the auxiliary field. After allowing the system to equilibrate for  $100\tau_0$ , the rest of the configurations are saved to construct the time series for  $\vec{M}_i(t)$ .

### 4.5.1 Magnetism and ‘phase diagram’

Connecting leads to the Mott insulator, without a bias, modifies the moment magnitude at the edges, explored earlier in 1D [137, 143] as well in 2D, as we saw in Sec.3.3.3. For the 3D geometry that we explore, we find that the presence of leads (at  $V = 0$ ) does not affect the structure factor significantly when  $U \gtrsim 4t$ , Fig. 4.9. Additionally, at low  $T$ , increasing  $V$  hardly



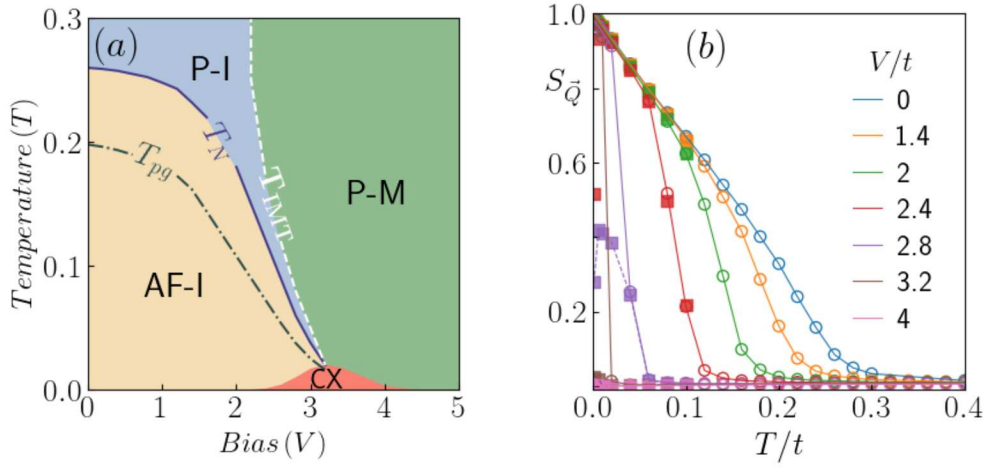


Figure 4.4: (a) Phase diagram of the voltage biased repulsive Hubbard model at  $U = 6t$ . The AF-I, P-M and P-I are the antiferromagnetic insulator, paramagnetic metal and paramagnetic insulator phases respectively. Insulating regimes have  $\partial I/\partial T > 0$  and the metal has  $\partial I/\partial T < 0$ . CX marks the hysteretic window. The solid blue line indicates  $T_N(V)$ , the dashed white line  $T_{IMT}(V)$  and the broken grey line indicates  $T_{pg}(V)$ . (b) The magnetic ordering peak,  $S(\pi, \pi, \pi)$  as a function of temperature ( $T$ ) for upward (open circles) and downward (solid squares) voltage ( $V$ ) sweeps. Beyond  $T = 0.02t$  the two curves coincide for all values of  $V$ . The inflection point for each curve gives the Néel temperature ( $T_N$ ) for the corresponding  $V$ .

changes the state upto  $V_c^+$ , after which the moments collapse, the gap closes, and the system carries a large current. In the downward sweep, the current carrying low moment state continues till  $V_c^-$ , after which the system switches back to the insulating state.

We construct a nonequilibrium  $V - T$  phase diagram, Fig.4.4(a), highlighting the magnetic, transport and spectral regimes that occur in the biased problem. There are three phases, the antiferromagnetic insulator AF-I, paramagnetic insulator P-I and the paramagnetic metal P-M, and a low  $T$  coexistence (CX) window bounded by  $V_c^\pm$ . The bias dependent temperature scales are  $T_N$  for the antiferromagnet to paramagnet transition, which can be inferred from the magnetic structure factor,  $T_{IMT}$  for the narrow window of thermally induced insulator-metal transition, which can be inferred from the temperature dependent current-voltage characteristics, and  $T_{pg}$  for crossover from gapped to pseudogap DOS, which we have discussed earlier. The relevance of these temperature scales shall be further discussed in subsequent sections.

**Magnetic structure factor:** Fig.4.4(b) shows the peak,  $S_{\vec{Q}}(T)$ , in the magnetic structure factor  $S_{\vec{Q}}$  defined in Sec.2.3.4. For the present problem,  $\vec{Q} = (\pi, \pi, \pi)$ , pertaining to Néel AF order is the relevant wavevector. For each  $V$  the Néel temperature is estimated from the point of inflection of the  $S_{\vec{Q}}(T)$  curve. There exists a coexistence region at  $T = 0$  in the interval  $2.2 \leq V/t < 4.3$ , which extends upto  $T_{coex} = 0.02t$ . The state in this region depends on the direction of voltage sweep. In Fig.4.4(b), the open circles denote the  $T$  dependence of  $S(\vec{Q})$  for upward sweep, while the solid squares denote the same for the downward sweep. The solid blue curve in Fig.4.4(a) shows the dependence of  $T_N$  on  $V$  for the upward sweep.  $T_N$  decreases slowly initially, with  $V$ ,

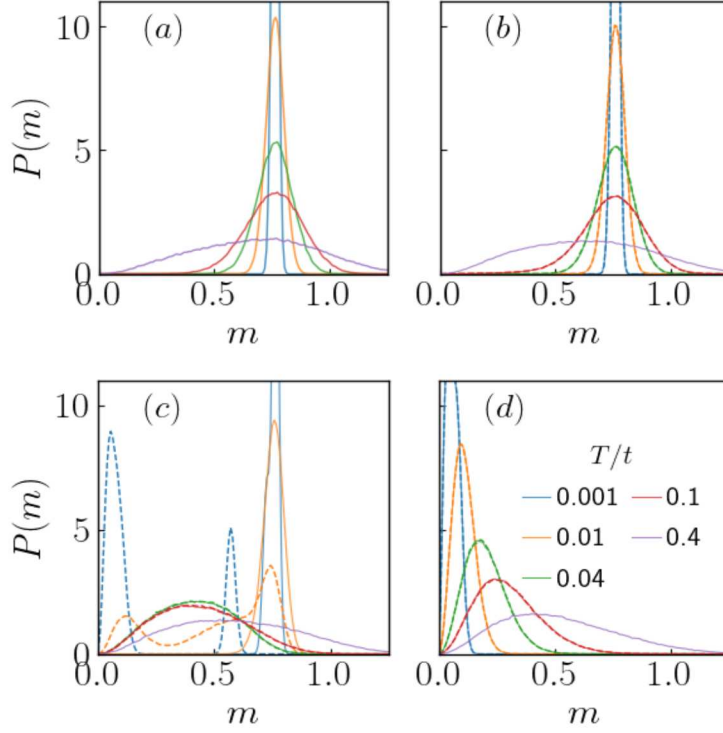


Figure 4.5: (a-d) Variation of the moment magnitude distribution with temperature ( $T$ ) for  $V/t = 0, 2, 3$  and  $5$  respectively. The solid (dashed) lines denote the distribution for upward (downward) sweeps at different temperatures.

and then quicker for  $V \gtrsim 0.5V_c^+$  and vanishes at  $V \approx 3.6t$ .

**Moment distribution:** The effect of bias on the distribution of the local moment magnitudes, as defined in Sec.2.3.5, is an important feature. The evolution of  $P(m)$  with temperature in different voltage regimes has been plotted in Fig.4.5. For  $V/t \leq 2$ , and  $T \ll T_N$ , the moments remain almost pinned to their equilibrium  $T = 0$  value. Hence, the  $P(m)$  is sharply peaked around  $0.8$ . As  $T$  increases the distribution broadens around the mean value up to  $T \approx T_N$ . Beyond  $T_N$  the distribution becomes skewed and the mean starts shifting to lower values with increasing  $T$ .

Between  $V = 2.2t$  and  $4.3t$  the low  $T$  moment distribution changes from being unimodal to bimodal, and acquires a sweep dependence. This is because the “effective potential” governing the moment distribution develops a metastable low moment minimum, as we discuss in the next section. Beyond  $V = 4.3t$ , where the system is metallic, the low temperature  $P(m)$  peak gets pushed to  $m = 0$  as the moments collapse throughout the system. With increasing  $T$ , the distribution broadens while the mean shifts towards larger  $m$  values.

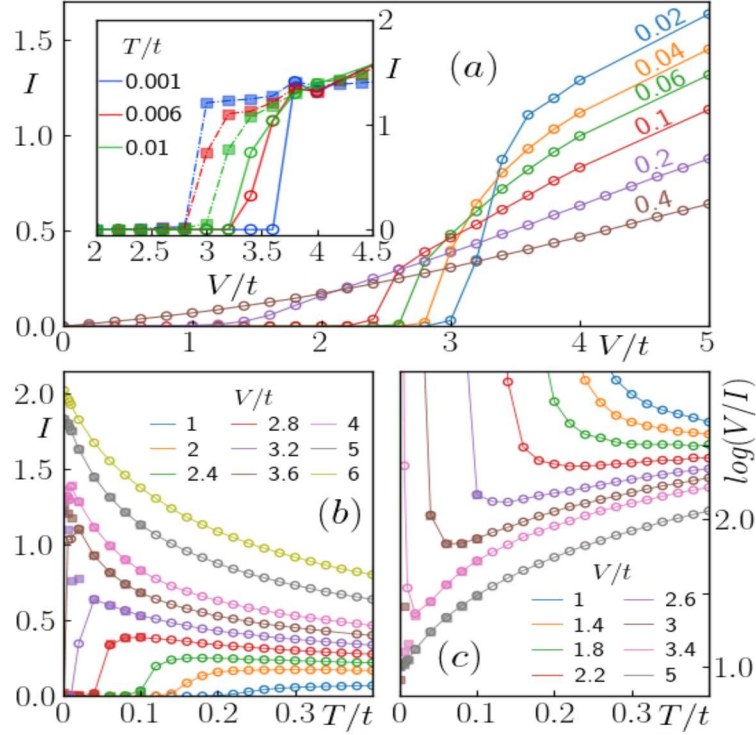


Figure 4.6: (a) The current-voltage characteristics with changing temperature ( $T$ ) for upward voltage sweeps. The inset shows the hysteretic behaviour at very low  $T$ . The solid lines and open circles correspond to upward voltage sweeps while the dashed lines and filled squares correspond to downward voltage sweeps. At  $T < 0.02t$ , the current changes discontinuously at  $V_c^\pm(T)$  for the upward and downward sweeps, respectively. Beyond the coexistence region the I-V has a unique threshold at  $V_c(T)$  which gets smeared with increasing  $T$  and vanishes for  $T > 0.1t$ . (b) Current ( $I$ ) as a function of temperature ( $T$ ) for different  $V$ .  $\partial I/\partial T > (<) 0$  indicates an insulating (metallic) phase. The peak in the  $I(T, V)$  curve for a fixed  $V$  indicates a temperature driven insulator to metal transition (IMT). (c) Resistance ( $R = V/I$ ) vs  $T$  plotted on a log scale. A minimum in the  $R(T, V)$  curve for a fixed  $V$  indicates insulator to metal crossover.

## 4.5.2 Transport characteristics

The charge transport is characterised by the current-voltage (I-V) characteristics, with the current given by

$$I_j(V) = \int_0^{t_M} \frac{dt}{t_M} \int_{-D}^D \frac{d\omega}{2\pi} \text{Tr} [\mathcal{G}_{j+1,j;\sigma}^<(t, \omega) - \mathcal{G}_{j,j+1;\sigma}^<(t, \omega)]. \quad (4.5)$$

$I_j(V)$  is the bond current between sites  $j$  and it's neighbouring site in the longitudinal direction and  $\mathcal{G}^<$  is the *adiabatic* lesser Green's function and the trace is over the  $2 \times 2$  spin subspace. Within our approximation the Green's function with label  $t$  depends only on the instantaneous configuration  $\{\vec{M}(t)\}$ . Due to current conservation  $I_j(V)$  must be independent of  $j$ , although in a numerical implementation the conservation depends sensitively on the dissipation parameter  $\eta$  which introduced to stabilise the numerics. We have discussed this point at length in Chapter 3. For the finite temperature implementation we have checked that current conservation holds good



at higher temperatures, particularly in the metallic phase. At very low temperatures  $T < 0.05t$  current conservation can be violated by up to 10% near the edges. For obtaining the current-voltage characteristics  $I - V$ , we have averaged the current along the longitudinal direction.

The I-V characteristics is plotted in Fig.4.6(a) for different temperatures. The inset shows hysteresis for  $T < T_{coex} \sim 0.02t$  while the main panel shows the response for  $T \gtrsim 0.02t$ . Above  $T_{coex}$  and upto  $T \sim 0.3t$  the I-V characteristic has a “threshold” at some  $V_c(T)$  below which, the current remains exponentially suppressed. Beyond  $V_c$ , the current rises sharply with increasing  $V$  and saturates as  $V$  approaches the bandwidth  $D$  of the connected system. With increasing  $T$ , the threshold reduces, vanishing for  $T \gtrsim 0.3t$ . The current saturation at large  $V$  is similar to what we observed in the 2D problem at zero temperature. The suppression of  $V_c$  with increasing  $T$  has been observed in experiments on various driven Mott systems [37–43].

Fig.4.6(b) shows  $I(T)$  at different  $V/t$  values. The results reveal three regimes:

1. Insulating, where the system becoming more conducting with increasing  $T$ , showing  $\partial I/\partial T > 0$  at all  $T$ . This happens for  $V/t \leq 2$ .
2. Metallic, where the system becoming less conducting with increasing  $T$ , showing  $\partial I/\partial T < 0$  at all  $T$ . This occurs for  $V/t > 3.8$ .
3. Showing an insulator-metal transition: crossing over from  $\partial I/\partial T > 0$  to  $\partial I/\partial T < 0$  with increasing  $T$ . We label the temperature at which  $\partial I/\partial T = 0$  as  $T_{IMT}$ . The thermal IMT happens for  $2 < V/t < 3.8$ .

The corresponding ‘resistance’  $R = V/I$  is shown in Fig.4.6(c) on a logarithmic scale. In the deep insulating regime  $R$  decreases exponentially with increasing  $T/t$  and well in the metal it rises monotonically with  $T/t$ . At intermediate  $V/t$  it shows non monotonic  $T/t$  dependence. This feature, arising from thermal fluctuations in a non equilibrium situation, is the most important result of our paper. We will discuss the physical basis further on. Note that within a linear response treatment of the Mott insulator  $V/I$  is independent of  $V/t$  and solely dependent on  $T/t$ . This would be true of the  $V \lesssim 1$  window (the top right curve). The effective resistance at all other voltages depends crucially on the applied bias.

### 4.5.3 Density of states

Another quantity of interest is the system averaged single particle density of states (DOS)

$$\mathcal{A}(\omega) = -\frac{1}{2\pi N} \int_0^{t_M} \frac{dt}{t_M} \sum_i \text{Im} \left( \text{Tr} [\mathcal{G}_{ii}^R(t, \omega)] \right), \quad (4.6)$$

where  $\mathcal{G}^R$  is the *adiabatic* retarded Green’s function and the trace is over the local  $2 \times 2$  spin subspace.  $N$  is the total no. of sites.

The behaviour of the DOS with increasing  $T$ , in different voltage regimes, is shown in Fig.4.7(a). For  $0 \leq V/t \leq 2.4$ , for low  $T$ , the DOS has a gap. With increasing  $T$  the gap gets smeared at the edges and ultimately develops into a pseudogap beyond  $T_{pg}$  (Fig.4.7(b)). However, there is significant weight at the Fermi level in the pseudogap phase even at  $V = 0$ , which is different from the behaviour in the disconnected equilibrium system, evident from Fig.4.2(a). This is due to dissipation coming from the leads, and the weight at the Fermi level above  $T_{pg}$  in the insulating phase may subside with increasing size in the longitudinal direction.

For  $2.4 < V/t < 3.4$ , in the upward sweep the DOS remains gapped at low temperatures, but develops subgap weight upon increasing  $T$ , even in the insulating phase (Fig. 4.7(c)). Upon heating beyond  $T_{IMT}(V)$  the DOS becomes ungapped and broadens with increasing  $T$  further. For the downward voltage sweep in this regime, the DOS remains ungapped even to the lowest temperature. For  $V/t > 3.4$ , the DOS remains ungapped up to the lowest temperature, broadens with increasing  $T$ , and further develops a pseudogap at high  $T$ .

In Fig.4.8, we plot the temperature dependence of the local DOS (LDOS) for the edge (panels (a1)-(d1)) and the central site (panels (a2)-(d2)) with varying voltage. The edge sites remain

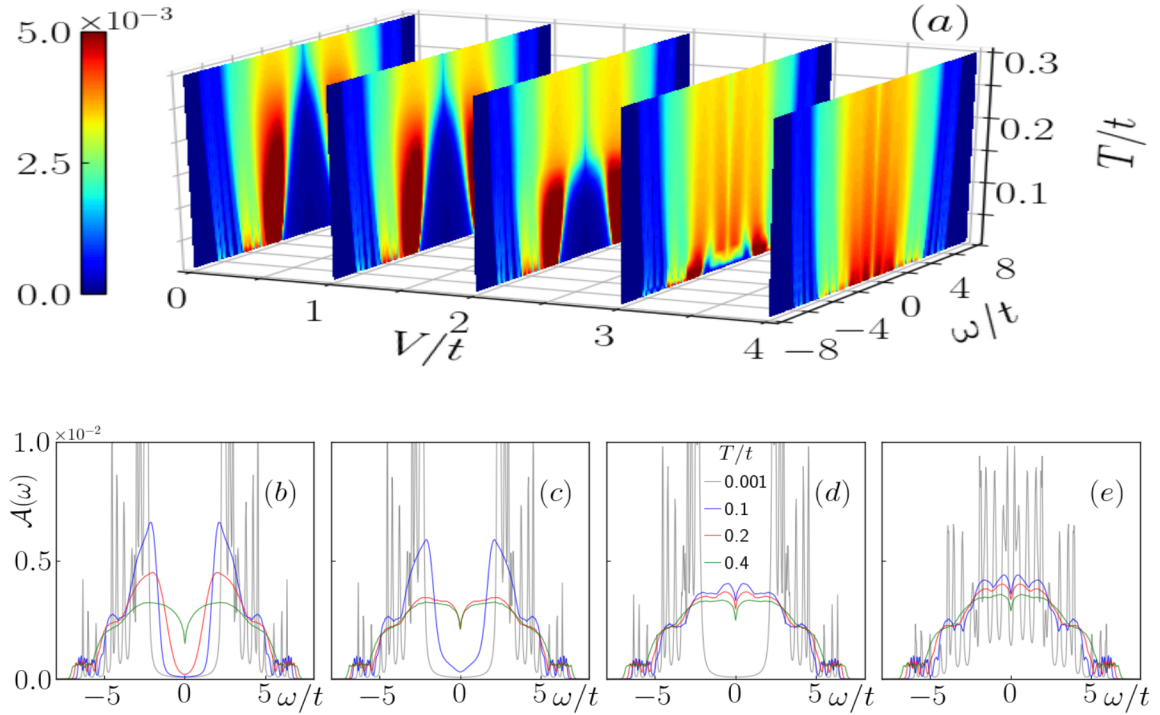


Figure 4.7: Top: Map of DOS for varying temperature and voltage, on the upward sweep. For  $V/t \leq 2.2$ , the low  $T$  DOS remains gapped and becomes pseudogapped for  $T > T_{pg}$ , in both the sweep cycles. For  $2.2 < V/t < 3.4$  the DOS remains gapped at low temperature, develops subgap weight with increasing  $T$ , even in the insulating phase, and ultimately becomes pseudogapped at large  $T$ . For the downward sweep, the DOS in this regime retains subgap weight even to the lowest temperature. For  $V/t \geq 3.4$  the DOS remains ungapped at low  $T$ , broadens with increasing  $T$ , and develops a pseudogap at high  $T$ . Bottom: The variation of density of states (DOS) with temperature for  $V/t = 0, 2.2, 3.4$  and  $5$ .

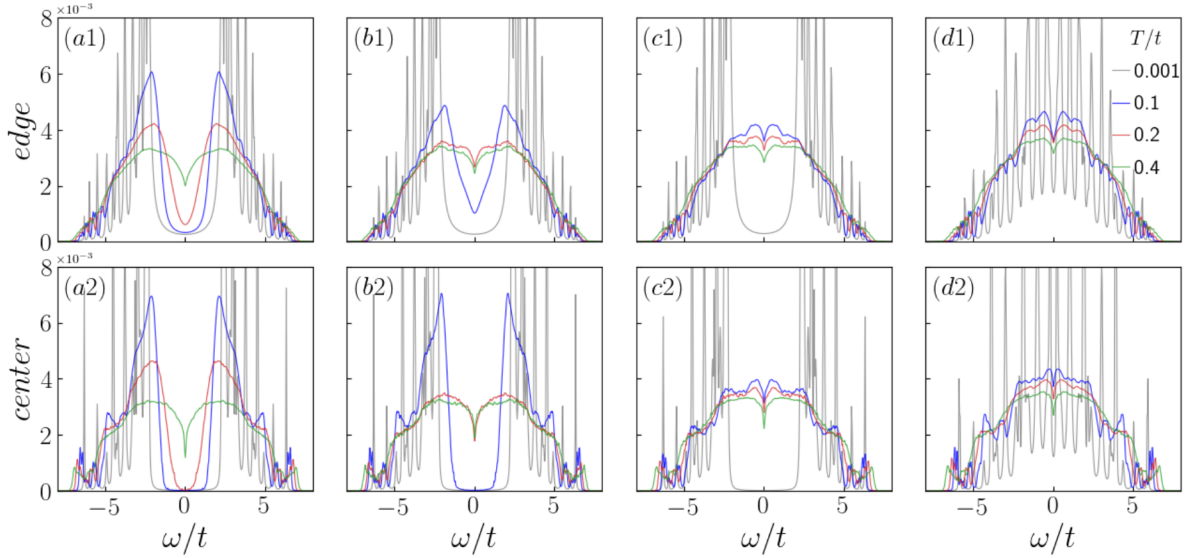


Figure 4.8: LDOS at an edge site (top row) and at a central site (bottom row) for  $V/t = 0, 2.2, 3.4$  and  $5$  from left to right. The edge sites remain ungapped for all voltages and temperatures due to hybridisation with the leads, while the sites at the center remain (un)gapped in the (metallic) insulating phase. Increasing temperature leads to enhancement of weight at the Fermi level up to the pseudogap temperature  $T_{pg}(V)$ . Beyond  $T_{pg}$  the LDOS broadens and the weight at the Fermi level gradually decreases.

ungapped for all values of  $V$  at low  $T$ . This is due to strong hybridisation with the metallic baths. They gain weight at the Fermi level with increasing  $T$ . The sites at the center remain gapped at low  $T$  in the insulating phase, but become ungapped in the as  $V$  goes beyond  $V_c$ , evident from panels (a2)-(d2) in Fig.4.8. With increasing temperature the sites at the center go from gapped to pseudogapped at  $T_{pg}(V)$  in the insulating phase, while in the metallic phase the LDOS broadens due to enhanced scattering at higher temperatures.

#### 4.5.4 Local charge and spin density

In Fig.4.9, we show the average charge and moment magnitude which are defined as:

$$\langle \delta n_{i_x} \rangle = 1 - \sum_{i_y, i_z}^{L_y, L_z} \int_0^{t_M} \frac{dt}{t_M} \int_{-D}^D \frac{d\omega}{2\pi} \text{Tr} (\mathcal{G}_{ii}^K(t, \omega)) \quad (4.7a)$$

$$\langle |\vec{S}_{i_x}| \rangle = \sum_{i_y, i_z}^{L_y, L_z} \int_0^{t_M} \frac{dt}{t_M} \left| \int_{-D}^D \frac{d\omega}{2\pi} \text{Tr} (\mathcal{G}_{ii}^K(t, \omega) \vec{\sigma}) \right| \quad (4.7b)$$

where  $\mathcal{G}^K$  is the adiabatic Keldysh Green's function and the trace is over the  $2 \times 2$  local spin subspace. At  $V/t = 0$ , the average charge profile remains vanishingly small throughout the longitudinal direction at all temperatures, while the moment magnitude falls as the system is heated beyond  $T_N$ . For  $0 < V/t < 2$ , the charge profile shows slight deviations at the edges,

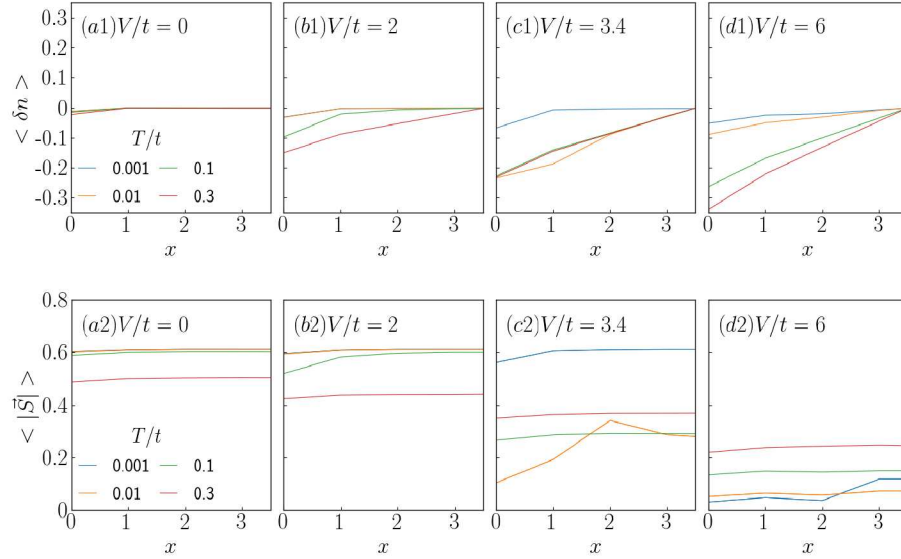


Figure 4.9: (a1-d1) Variation of the average charge profile, along the longitudinal direction, with increasing temperature for  $V/t = 0, 2, 3.4$  and  $6$ . With sufficient averaging the profile becomes antisymmetric about the center of the system, hence only the left half has been shown. (a2-d2) Variation of the average local moment magnitude along the longitudinal direction. The averaging leads to a symmetric profile across the center of the system.

even at very low  $T$ , and becomes linear at high  $T$ . The moment magnitude also shows deviations at the edges, and gets diminished throughout the system with increasing  $T$ . For  $2 < V/t < 3.6$ , the charge profile shows edge deviations in low  $T$  insulating phase, but becomes linear as one heats up the system to reach the P-M phase. The moment magnitude shows nonmonotonic behaviour with temperature. For  $V/t > 3.6$ , the system remains in the P-M phase at all  $T$ . The charge profile remains linear, whose slope increases with increasing  $T$ , while the moment profile remains fairly constant and increases with increasing  $T$ .

## 4.6 Effective models

Beyond the detailed numerics we suggest a qualitative understanding of the nonequilibrium phenomena by providing simpler effective models in certain parameter regimes.

### 4.6.1 $T = 0$ state at finite $V$

The  $T = 0$  transition can be modeled by extremising a functional of the form

$$F(M) = \frac{a(V)}{2}M^2 - \frac{b}{3}M^3 + \frac{c}{4}M^4 \quad (4.8)$$

where  $M$  is the magnitude of the local moment, assumed to be uniform across the system.  $a(V) = a_0 \left( e^{-V^*/V} - e^{-V^*/V_c^-} \right)$ ;  $a_0, V^*, b, c$  are fitting parameters which take positive values.  $a_0, V^*$  and  $b$  can be determined in terms of the moment magnitude at  $V = 0$  and  $V = V_{c+}$ , and



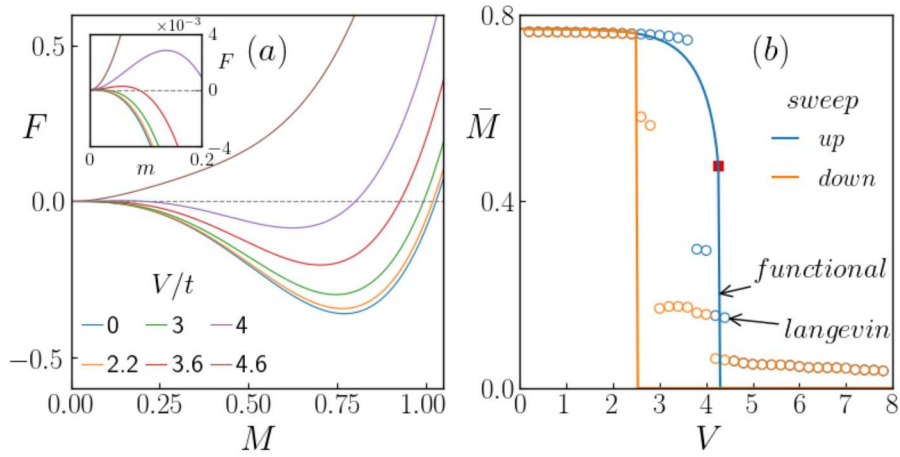


Figure 4.10: (a) Effective functional for different values of  $V/t$ . For  $V < V_c^-$  it has a unique minimum at large  $M$ . For  $V_c^- < V \leq V_c^+$  it develops two minima (inset). For  $V > V_c^+$  there is a unique minimum at  $M = 0$ . (b) The resulting moment  $\bar{M}$  at the minimum, which gets a sweep dependence in the coexistence region due to the presence of two minima. The open symbols are actual data points for  $T = 0.001t$ . The lines show the corresponding profile obtained from the effective functional. The red square indicates the point at which the moment profile jumps in the upward sweep according to the effective functional. In the effective description, the large  $V$  moment has been approximated to be zero.

$\Delta V_c$ . The moment profile does not depend on the parameter  $c$ , which just sets the overall scale of  $F$ . It can be fixed by fitting the low  $T$ ,  $P(m)$  at  $V = 0$ . Here, we have approximated the moment amplitude in the large  $V$  state to vanish. The  $V$  dependence of  $F$  has been shown in Fig. 4.10(a) and the resulting moment profile has been shown in Fig. 4.10(b) (solid lines), along with order parameter variation within  $T = 0$  mean-field theory (open symbols). For  $V < V_c^-$ ,  $F$  has a unique minimum at finite  $M$ . For  $V_c^- < V \leq V_c^+$ ,  $F$  develops another minimum at  $M = 0$ . Beyond  $V_c^+$  only the  $M = 0$  minimum survives. For the upward voltage sweep the system remains stuck in the finite  $M$  minimum till  $V_c^+$  and then switches to the  $M = 0$  minimum discontinuously. A similar discontinuous transition happens in the downward sweep, in which the stating state corresponds to the  $M = 0$  minimum, which changes abruptly at  $V_c^-$ . This explains the low  $T$  coexistence and hysteresis. A power law dependence of  $a(V)$  on voltage leads to a stronger dependence of the  $\bar{M}$  on bias. The coefficients  $a, b, V^*$  should ideally be extracted from the  $T = 0$  Keldysh mean field theory. While the  $T = 0$  moment magnitude sets a reference it does not explain the behaviour of  $T_N$  - which falls in a continuous manner despite  $\bar{M}(V)$  at  $T = 0$  being sharply discontinuous.

### 4.6.2 Suppression of Néel temperature

We find that the Néel temperature  $T_N$  decreases with increasing  $V$ . Making the crude assumption that the bare Heisenberg exchange scale ( $J = \frac{t^2}{U}$ ) remains unchanged with  $V$ , the reduction in  $T_N$  with increasing  $V$  may be attributed to a reduction in the average moment magnitude  $\langle |M| \rangle$ , for a fixed temperature, with increasing  $V$ . Fig. 4.11(a) shows the variation of  $\langle |M| \rangle$  with increasing

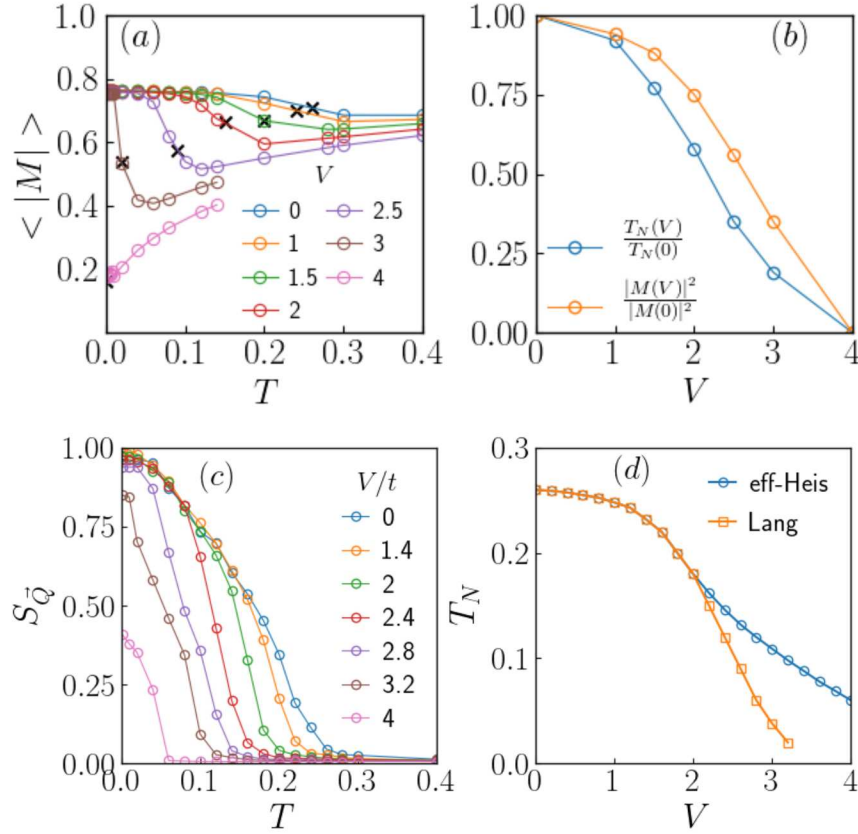


Figure 4.11: (a) Variation of average moment magnitude  $\langle |M| \rangle$  with temperature ( $T$ ) for different values of bias voltage ( $V$ ). For each  $V$  the corresponding Néel temperature ( $T_N(V)$ ) has been marked with a black cross on the trace.  $\langle |M| \rangle(T)$  develop minima at  $T_*(V)$ . (b) Comparison of the ratios of Néel temperatures at finite  $V$  over that at  $V = 0$  and and the corresponding squared average moment magnitudes at  $T_*$ . The comparison suggests that the finite  $V$  magnetic transition can be modeled by an effective Heisenberg model with  $J_{ij}^{eff} = \frac{t^2}{U} |\vec{M}_i| |\vec{M}_j|$ , where the amplitudes must be sampled from the  $P(m; V, T)$  distributions obtained through the full Langevin scheme. (c) Variation of magnetic structure factor peak at  $(\pi, \pi, \pi)$  with temperature for different values of  $V$ . From this, the Néel temperature for the effective Heisenberg model is extracted and compared with that obtained from the full calculation in (d). They show almost exact match at low  $V$ , and significant difference at large  $V$  close to the metallic phase which indicates failure of the effective Heisenberg picture.

$T$ , for different  $V$  values. We find that  $\langle |M| \rangle$  behaves nonmonotonically with temperature between  $1 < V/t < 4$ , and develops a minimum at a temperature  $T_*(V) > T_N(V)$ . In Fig. 4.11(b) we have compared  $T_N(V)/T_N(0)$  with  $\langle |M| \rangle^2(V)/\langle |M| \rangle^2(0)$  at  $T_*(V)$ , and find that they follow a similar trend with increasing  $V$ . This suggests that an effective quadratic theory for the local moments may be able to describe the underlying physics. We can further assume that the amplitude distributions of the local moments are same across the system, given by  $P(m; V, T)$  and shown in Fig. 4.5. In the insulating phase, increasing voltage leads to reduction in the local moment amplitudes, which is negligible at low  $V$  but becomes significant near  $V \lesssim V_c$  (above the coexistence region). Moreover, thermal amplitude fluctuations lead to broadening of  $P(m)$  such that the mean moment size increases with temperature for high temperatures in the paramagnetic

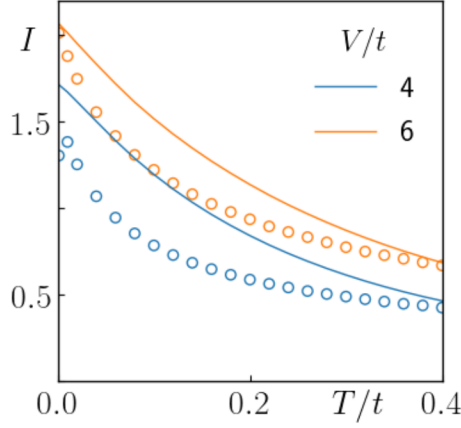


Figure 4.12: Comparison of the approximate current (solid lines) with the exact result (open circles) in the paramagnetic metal phase for  $V/t = 4, 6$ .

phase. A competition between these two effects leads to a nonmonotonic behaviour of  $\langle |M| \rangle(V)$  with temperature, as is evident in Fig. 4.11(a).

Motivated by this, we attempt to explain the drastic reduction in  $T_N$  beyond  $V \sim 0.5V_c^+$  by invoking an effective Heisenberg model in which the moment magnitudes are determined by the  $P(m)$  distribution described in Sec. 4.5.1. For the amplitude modulated Heisenberg model the effective exchange coupling is given by  $J_{ij}^{eff} = \frac{t^2}{U} |\vec{M}_i| |\vec{M}_j|$ , where  $|\vec{M}_i|$  is obtained by sampling  $P(m; V, T)$ . This gives a reasonable match for both the structure factor Fig. 4.11(c) as well as the Néel temperature Fig. 4.11(d), with the full calculation, except very near  $V_c$ . We also tried to promote the  $F(M)$ , introduced in the previous section, to a ‘Boltzmann weight’ for local fluctuation of moment magnitude, and couple these moments via a nearest neighbour exchange  $J_{eff}$  that reproduces the  $V = 0$  Néel temperature. This did not work since the configurational weights have a non trivial  $T$  dependence near  $V_c$  (Fig. 4.5).

### 4.6.3 The large $V$ state

We can set up an approximate calculation for the current at large  $V$ , where the mean moment size gets quenched. One can approximate the adiabatic lesser Green’s function  $\mathcal{G}^<(t, \omega)$ , which enters the expression for the current in Eq. 4.5 in the main text, by setting up a perturbation theory about the tight-binding limit.

$$\mathcal{G}^< = \frac{1}{2} (\mathcal{G}^K - (\mathcal{G}^R - \mathcal{G}^A)) \quad (4.9a)$$

$$\begin{pmatrix} \mathcal{G}^R & \mathcal{G}^K \\ 0 & \mathcal{G}^A \end{pmatrix} = \begin{pmatrix} [g^{-1}]^R - \Sigma^R & [g^{-1}]^K - \Sigma^K \\ 0 & [g^{-1}]^A - \Sigma^A \end{pmatrix}^{-1} \quad (4.9b)$$

with,

$$\Sigma_{i,j;\alpha,\beta}^{R,A,K}(t, \omega) = M_i^\alpha(t) M_j^\beta(t) g_{ij}^{R,A,K}(\omega) \quad (4.9c)$$

where  $g^{R,A,K}$  are the Green's functions of the connected tight-binding system. The mean current is computed by averaging over the time-series of  $M$ . This can be simplified further if one averages over the self-energy instead of the Green's function, assuming the distribution for  $M$ s to be normal, i.e.,  $\langle M_i^\alpha(t) M_j^\beta(t) \rangle \approx T \delta_{ij} \delta_{\alpha\beta}$ . So the average self-energy

$$\langle \Sigma_{i,j;\alpha,\beta}^{R,A,K}(\omega) \rangle = T \delta_{ij} \delta_{\alpha\beta} g_{ij}^{R,A,K}(\omega) \quad (4.10)$$

can be used to approximate the mean current. Fig.4.12 compares the temperature dependence of the approximate current with the actual result in the P-M phase. They seem to compare well for sufficiently large  $V$ , given the *drastic* nature of the approximations.

This suggests that the current in the metallic phase is essentially given by the tight-binding result for  $V \geq 6t$  as  $T \rightarrow 0$ . For a finite system this has a finite value, and scales linearly with the number of conduction channels which is proportional to the cross sectional area  $A$ . Hence the resistance in the metallic phase is finite even as  $T \rightarrow 0$  within a finite sized calculation, as is evident in Fig.4.12, and would vanish only if  $A \rightarrow \infty$ . As the temperature increases, thermal fluctuations of the background moments leads to enhanced scattering which depletes the current further.

## 4.7 Discussion

### 4.7.1 Validity of approximations

The Langevin equation we use involves two key assumptions: (i) adiabaticity, and (ii) thermal noise. The adiabatic assumption would be valid if the typical frequency associated with magnetic fluctuations were self consistently smaller than the electron frequency. We have not shown the magnetic spectra here but at  $U = 6t$  the magnetic bandwidth is  $3J_{eff} \sim \frac{12w^2}{U}$ , while the electronic bandwidth is  $\sim U$ , and their ratio is  $\sim 1/3$ . This argument does not hold in the deep metallic state where  $U$  is rendered ineffective. The ‘thermal noise’ is used in the spirit of a first approximation, consistent with mean field theory at  $T = 0$ . In a scheme with quantum fluctuations built in, the noise would need self consistent modification.

The noise in the current carrying state is nontrivial. The noise kernel (Eq.4.4b) depends on bias through the local diffusion coefficients  $D_i(t) = \alpha/(1 + \alpha^2 |\vec{M}_i(t)|^2)$ , which themselves depend on the local moment magnitude. For a given  $\alpha$ , the noise grows stronger as  $|\vec{M}_i|$  diminishes, which is the primary effect caused by increasing bias, as we have discussed in the previous sections.

### 4.7.2 Landau damping in the metallic phase

In the metallic phase, one expects Landau damping of the local moments due to the electrons, which has a characteristic  $1/q$  dependence in the long wavelength limit, and would give long



range dissipative kernel in space. The present scheme should be able to capture the physics of Landau damping since it retains the spatial variations of the classical auxiliary fields exactly. Here we demonstrate it explicitly by linearising the Langevin equation about a mean field saddle point.

We recollect the Langevin equation governing the dynamics of the spin field,

$$\frac{d\vec{M}_i}{dt} - \alpha \vec{M}_i \times \frac{d\vec{M}_i}{dt} = \gamma_i \left( \langle \vec{\sigma}_i \rangle - \vec{M}_i + \vec{\xi}_i \right) \quad (4.11)$$

where  $\gamma_i = \frac{2U}{\alpha} (1 + U^2 |\vec{M}_i|^2)$  is the dissipation coefficient and  $\vec{\xi}_i$  is the noise.  $\langle \vec{\sigma}_i \rangle$  depends on the background  $\vec{M}$  configuration through the relation,

$$\langle \vec{\sigma}_i \rangle = \text{Tr} \left[ \hat{\mathcal{G}}_{ii}^K(t, t) \vec{\tau} \right] \quad (4.12)$$

where  $\hat{\mathcal{G}}^K$  is the adiabatic Keldysh Green's function defined for a given  $\vec{M}$  background. Linearising this about an antiferromagnetic (AFM) saddle point by assuming  $\vec{M}_i(t) = M_i \hat{z} + \delta \vec{m}_i(t)$  and retaining only the terms linear in  $\delta \vec{m}$  gives us,

$$\delta \dot{m}_{i,a} - \alpha \epsilon_{abc} M_{i,b} \delta \dot{m}_{i,c} = 2U \gamma_i \int dt' \Pi_{ij,ab}^R(t, t') \delta m_{j,b}(t') + \gamma_i \xi_{i,a} \quad (4.13)$$

where  $\Pi^R$  is the electronic polarisation in the AFM saddle point and a summation over repeated indices is assumed.

This gets further simplified when we consider the paramagnetic (PM) phase for which  $M_i$  vanish and  $\Pi_{ij,ab}^R \rightarrow (\Pi_0)_{ij}^R \delta_{ab}$ , where  $\Pi_0$  is the polarisation of free electrons in a tight-binding lattice.

Thus, the above equation in the fourier representation becomes,

$$\left[ -\iota \frac{\omega}{\gamma} + 2U (\Pi_0)_{\vec{q}}^R(\omega) \right] \delta \vec{m}_{\vec{q}}(\omega) = \vec{\xi}_{\vec{q}}(\omega) \quad (4.14)$$

$$(\Pi_0)_{\vec{q}}^R(\omega) = \sum_{\vec{k}} \frac{n_F(\epsilon_{\vec{k}+\vec{q}/2}) - n_F(\epsilon_{\vec{k}-\vec{q}/2})}{\omega + \iota\eta - (\epsilon_{\vec{k}+\vec{q}/2} - \epsilon_{\vec{k}-\vec{q}/2})} \quad (4.15)$$

where  $\epsilon_{\vec{k}} = -2t_{hop} \sum_i \cos(k_i)$  is the tight-binding dispersion with hopping amplitude  $t_{hop}$  and  $n_F$  is the Fermi distribution function.

Linearising the dispersion in  $\vec{q}$  and defining  $\vec{v}(\vec{k}) \equiv 2t_{hop} \sin(\vec{k})$ , we get,

$$(\Pi_0)_{\vec{q}}^R(\omega) \approx \sum_{\vec{k}} \frac{n_F(\epsilon_{\vec{k}} - \vec{v}(\vec{k}) \cdot \vec{q}/2) - n_F(\epsilon_{\vec{k}} + \vec{v}(\vec{k}) \cdot \vec{q}/2)}{\omega + \iota\eta - \vec{v}(\vec{k}) \cdot \vec{q}} \quad (4.16)$$

$$= \int d\epsilon \rho(\epsilon) \frac{n_F(\epsilon - \vec{v}(\epsilon) \cdot \vec{q}/2) - n_F(\epsilon + \vec{v}(\epsilon) \cdot \vec{q}/2)}{\omega + \iota\eta - \vec{v}(\epsilon) \cdot \vec{q}} \quad (4.17)$$

(4.18)

where we have replaced the momentum sum by an integration over the density of states. At low temperature, the Fermi functions in the numerator restrict the integral to a narrow strip of width  $\vec{v} \cdot \vec{q} \ll \epsilon_F$  about the Fermi energy. Hence, in the long wavelength limit, we can approximate the above integral by,

$$(\Pi_0)_{\vec{q}}^R(\omega) \approx -\frac{\rho(\epsilon_F)}{2} \int_{-1}^1 dz \frac{v_F q z}{\omega + i\eta - v_F q z} \quad (4.19)$$

$$= \rho(\epsilon_F) \left[ 1 + \frac{\omega}{2v_F q} \ln \left| \frac{v_F q - \omega}{v_F q + \omega} \right| \right] + i\pi \rho(\epsilon_F) \frac{\omega}{2v_F q} \theta(v_F q - |\omega|) \quad (4.20)$$

The singular  $1/q$  contribution in the imaginary part of  $(\Pi_0)^R$  is the Landau damping term.

### 4.7.3 Numerical issues

There are several numerical issues in this study which we try to address here. Firstly, in order to stabilise the inversion routines one needs to add a small dissipation  $\eta$  at each site in the system, as we discussed at length in Ch.3. In order to get physically sensible results, one must choose  $\eta \ll \delta$ , where  $\delta$  is the average level spacing in the problem. Once this criteria is met, we find that current conservation across the system is better respected in the 3D problem, as compared to the 2D case ( $\sim 10\%$  as compared to  $\sim 25\%$  for the lowest value of  $\eta$ ).

The second issue is with the run length in the Langevin dynamics in order to achieve a steady state. As discussed in Sec.4.5, the time taken for thermalisation is controlled by a characteristic timescale  $\tau_0$  for the equilibrium system. This can, in principle, vary in presence of large bias, and hence we let the system thermalise for  $100\tau_0$  before recording the time-series. We have also, varied the run length at a few parameter points and checked that the results presented here do not change with increasing run length up to twice the duration.

Lastly, there is the issue of size dependence of our results. The Langevin scheme presented here leads to a numerically intensive computation primarily because of the presence of leads in the nonequilibrium problem, and is worsened by the presence of multiplicative noise. As a result, for each site in every time step we need to diagonalise the electronic Hamiltonian twice. Moreover, one needs to have a sufficiently long run length in order to achieve a steady state. All these considerations constrain us to a modest size of  $8 \times 4 \times 4$ .

However, to our benefit, we discovered that the voltage driven insulator-metal transition is first order for the 3D system. This means the transition should be realised even in larger systems although the coexistence region may pick up a size dependence. Furthermore, the magnetic transition at equilibrium is easily captured within our working size and several other studies have used even smaller systems to study it. For the voltage driven problem, a larger size may provide more resolution around the low temperature insulator-metal transition region of the phase

---

diagram, but it should not change the essential features highlighted in this study. We have also checked the size independence of results for a few parameter points on a  $10 \times 4 \times 4$  system.

#### 4.7.4 Comparison with experiments

Experimentally, the I-V characteristics have a generic form across the transition metal oxides, TMO's, (e.g. vanadium oxides [38, 39], ruthenates [40, 41], magnetites [42, 43]) and some organics [45]. All these show a first order transition at low  $T$  which gets weaker with increasing temperature. This aspect is well captured by our theory, unlike other microscopic approaches. Some TMOs also undergo a temperature driven structural transition at equilibrium. However, the transport measurements have been made below this equilibrium transition temperature. Our theory suggests that the transport characteristics can be explained via a purely electronic mechanism. An experiment on a multiorbital ruthenate has also reported suppression of Néel temperature with increasing current [48].

### 4.8 Conclusion

We have constructed a nonperturbative real time finite temperature scheme to study steady state nonequilibrium effects in a strongly correlated system. This Langevin equation approach simplifies the underlying Keldysh field theory by assuming adiabaticity, *i.e.*, that electrons are much faster than magnetic degrees of freedom, and a thermal noise. With these assumptions we could implement a numerical study of a Mott insulator in a finite 3D geometry. We have established a voltage sweep driven hysteretic insulator-metal transition at low temperature, the collapse of the Néel and pseudogap temperature with increasing bias, and a thermally induced insulator-metal transition at finite bias.

In our analysis the primary driver of the finite temperature effects is thermal amplitude fluctuation of the local moments in the bias induced first order landscape. As  $V \rightarrow V_c$ , the thermal amplitude fluctuation of the moments drives the thermal response of the system. A softening of the moment implies stronger charge fluctuation and greater metallicity. The behaviour of moment magnitudes and their angular fluctuation directly affects the DOS. Deep in the AF-I phase the large ordered moments generate a large 'gap' in the DOS, albeit with exponentially suppressed low energy weight and current. With increasing  $T$  the angular fluctuations of the moments smear the gap and increase the current. As the voltage increases, amplitude fluctuations of the moments also join in, creating additional low energy DOS and larger current.

In the deep metallic phase the moment magnitude is small at low  $T$ . This closes the Mott gap and allows a large current to flow. As  $T$  increases, the moment distribution broadens, the mean moment increases, and its angular fluctuation scatters the electrons. This suppresses the current. At intermediate  $V$  a combination of activation induced current increase competes with scattering induced current decrease leading to the thermal IMT.

---

The Langevin approach has opened up a scope to tackle various nonequilibrium problems which have remained inaccessible till now.

---

# Nonequilibrium magnetic dynamics

## 5.1 Background

Antiferromagnetic insulators have been the subject of intense study, especially in 2D, since the discovery of high temperature superconductivity in layered cuprates [169]. It has been suggested that superconductivity in these materials might be related to their magnetic properties [170–174], although the exact mechanism behind superconductivity remains debated to this day. This makes the antiferromagnetic Mott insulating parent state, and magnetism in the doped Mott insulator, an object of great interest.

The low temperature collective excitations in a magnet are spin waves. Inelastic neutron scattering experiments, introduced in Sec.1.3.4, measure the dynamical spin correlations in a solid through the interaction of neutrons with the magnetization density. It can measure the spin wave dispersion and broadening of the lineshapes. Theoretical modeling of quantum magnets constitutes writing down effective quantum spin models, like the Heisenberg model, based on phenomenological considerations. However, these can be *derived* as the low energy effective model, starting from a *microscopic* electronic Hamiltonian, like the Hubbard model, in the strong coupling regime where the charge excitations are essentially gapped out, which leads to fixed amplitude of the quantum spins in the corresponding spin model. Linear spin-wave theory (LST) [175, 176], has been extensively used to describe low temperature behaviour of the quantum spin models. Under the assumption of a large (fixed) amplitude of the spins, it maps the quantum spin model to a quadratic bosonic problem which can be easily solved. It has been successful in describing low temperature experimental results [68] and has also been tested against exact numerics [177].

An alternative approach is to start from the *parent* electronic model which hosts a magnetically ordered ground state that is accessible through a mean field treatment of the electronic interactions in the same spirit as we have discussed in Ch.3. The small oscillation dynamics of the order parameter about the mean field state can be recovered by using the random phase approximation

(RPA) approach. Being a more microscopic approach as compared to LST, it is applicable in more general scenarios. In the context of Hubbard model, it can not only capture the correct spin wave dispersion but also yield high-energy features like the particle-hole continuum[183]. It can also treat unconventional ordered states and incorporates small fluctuations in the size of the local moments. This approach has been used to describe several experiments in Mott insulators[178–183].

However, as we have seen in Chapter 3, the presence of a strong voltage drive promotes double occupancy locally in the 2D Hubbard model, even when overall half-filling is maintained. In this scenario, the size of the local moment reduces and the spins can undergo large amplitude fluctuations which cannot be captured by LST or RPA. Specifically, since RPA captures Gaussian fluctuations about an ordered state, it fails to capture a regime where the ordered state itself tends to destabilise through slow, but large amplitude fluctuations of the order parameter. Moreover, inhomogeneous driven systems have not been treated by these methods. In this chapter we briefly discuss the magnetic excitations in the 2D Hubbard model at equilibrium and then use the Langevin scheme, discussed in the previous chapter, to study excitations in a driven dissipative 2D Mott insulator at low but finite temperature.

## 5.2 Model and method

### 5.2.1 Model

We work with the 2D Hubbard model connected to noninteracting leads, which we had introduced in Ch.2 and recapitulate here,

$$\mathcal{H} = \mathcal{H}_{sys} + \mathcal{H}_{bath} + \mathcal{H}_{coup} \quad (5.1)$$

$$\mathcal{H}_{sys} = \sum_{\langle ij \rangle, \sigma} -t_{ij} d_{i\sigma}^\dagger d_{j\sigma} + U \sum_i n_{i\uparrow} n_{i\downarrow} \quad (5.1a)$$

$$\mathcal{H}_{bath} = \sum_{\nu, \beta} (\epsilon_\nu - \mu_\beta) c_\nu^{\dagger\beta} c_\nu^\beta \quad (5.1b)$$

$$\mathcal{H}_{coup} = \sum_{\langle ij \rangle, \sigma} v_{ij} \left( c_{i\sigma}^{\dagger L} d_{j\sigma} + c_{i\sigma}^{\dagger R} d_{j\sigma} + h.c. \right) \quad (5.1c)$$

where  $c_\nu^{\dagger\beta}$  ( $c_\nu^\beta$ ) denote the creation (annihilation) operators at the energy level  $\nu$  of the leads  $\beta \in \{L, R\}$  ( $L$  denotes the left lead and  $R$  the right lead).  $\mu_\beta$  are the chemical potentials in the conducting leads.  $\mu_{L,R} = \mu \pm (V/2)$ ,  $V$  being the applied bias.  $v_{ij}$  denote the matrix elements of the system-bath coupling.  $d_{i\sigma}^\dagger$  ( $d_{i\sigma}$ ) are the creation (annihilation) operators for the system.  $t_s$ ,  $\mu$  and  $U$  are the nearest-neighbour hopping amplitude, chemical potential and onsite Coulomb repulsion strength, respectively, in the system. We set  $t_{hop} = 1$ , and consider it to be the unit of energy.



### 5.2.2 Equilibrium Heisenberg limit

The Hubbard model Eq.5.1a at strong coupling  $U \gg t_{hop}$  reduces to the Heisenberg model. This can be seen most easily starting from the local term  $U \sum_i n_{i\uparrow} n_{i\downarrow}$  as the parent Hamiltonian and treating the kinetic term  $-t_{hop} \sum_{\langle ij \rangle, \sigma} c_{i\sigma}^\dagger c_{j\sigma} + h.c.$  under second order degenerate perturbation theory. The second order energy correction is given by

$$\delta E^{(2)} = -t_{hop}^2 \sum_{\langle ij \rangle} \sum_{|E\rangle} \sum_{\alpha, \alpha'} \langle \alpha_i \alpha_j | \left( c_{i\alpha}^\dagger c_{j\alpha} + h.c. \right) | E \rangle \frac{1}{U} \langle E | \left( c_{i\alpha'}^\dagger c_{j\alpha'} + h.c. \right) | \alpha'_i \alpha'_j \rangle \quad (5.2)$$

Using the relation  $\vec{\sigma}_i = \frac{1}{2} \sum_{\alpha\beta} c_{i\alpha}^\dagger \vec{\tau}_{\alpha\beta} c_{i\beta}$ , where  $\vec{\tau}$  is the  $2 \times 2$  Pauli vector, and considering the fact that the sum over  $|E\rangle$  acts as a complete sum, we can write

$$H_{eff} = \frac{4t_{hop}^2}{U} \sum_{\langle ij \rangle} \vec{\sigma}_i \cdot \vec{\sigma}_j = J \sum_{\langle ij \rangle} \vec{\sigma}_i \cdot \vec{\sigma}_j \quad (5.3)$$

with  $J \equiv \frac{4t_{hop}^2}{U}$ . This is the nearest neighbour Heisenberg model. Here we have neglected a constant term. More complicated spin models can be obtained if we go to higher orders in perturbation theory and for more complex lattices with longer-range hopping terms. Upon implementing a Holstein-Primakoff transformation and keeping fluctuations at the leading order in  $S = |\sigma|$  (the magnitude of the spin), gives us a quadratic bosonic Hamiltonian which can be diagonalized using a Bogoliubov transformation to obtain the spin wave dispersion [3, 175, 176]

$$\omega_{\vec{q}} = \pm 2JS \sqrt{\epsilon_0^2 - \epsilon_q^2} \quad (5.4)$$

where  $\epsilon_{\vec{k}}$  is the tight binding dispersion and the lattice constant  $a = 1$ . This is strictly true in the  $U \rightarrow \infty$  limit. At finite values of  $U$  the dispersion gets corrected due to the terms neglected in deriving the effective spin Hamiltonian, Eq.5.2.2.

### 5.2.3 Random phase approximation

The random phase approximation (RPA) describes spin excitations on the magnetically ordered equilibrium state of the Hubbard model. It captures the magnetic dynamics and order parameter renormalization both at weak and strong coupling [178, 179] and does a reasonable interpolation at intermediate coupling [180]. Starting with a mean-field decomposition of the Hubbard Hamiltonian, as discussed in Sec. 3.2, and assuming a homogeneous ordered state, we diagonalize the  $2 \times 2$  mean-field Hamiltonian in momentum space (Ref. Appendix A) to obtain the band dispersions

$$E_{\vec{k}}^{A,B} = \pm \sqrt{\epsilon_{\vec{k}}^2 + \Delta^2} \equiv \pm E_{\vec{k}} \quad (5.5)$$

where  $\epsilon_{\vec{k}} = -2t_{hop} (\cos(k_x) + \cos(k_y))$  is the tight-binding dispersion and the order parameter  $\Delta = \frac{U}{2} \sum'_{\vec{k}, \sigma} \text{sgn}(\sigma) \langle c_{\vec{k}+\vec{Q}, \sigma}^\dagger c_{\vec{k}, \sigma} \rangle$  (with  $\text{sgn}(\sigma) = \pm 1$  for  $\uparrow$  ( $\downarrow$ ) respectively) must be obtained by

solving the gap equation. Here the  $\vec{Q} = (\pi, \pi)$  and summation is on the reduced Brillouin zone (denoted by  $\prime$ ).

$$\frac{1}{U} = \sum_{\vec{k}}' \frac{f(E_{\vec{k}})}{E_{\vec{k}}} \quad (5.6)$$

Here we have assumed that the homogeneous saddle point value of the charge field  $\phi$  and the chemical potential  $\mu$  cancel each other, which is indeed the case for the translation invariant system at half-filling.

The antiferromagnetic ordering implies the existence of low energy bosonic excitations, which are the transverse spin waves, as well as longitudinal spin fluctuations. The spin waves are gapless by the Goldstone theorem since they arise due to a spontaneously broken spin rotation invariance. These can be analyzed by studying the transverse dynamical spin susceptibility,

$$\chi^{+-}(\vec{q}, \vec{q}', \omega) = \int dt \left[ \frac{i}{2N} \langle T \sigma_{\vec{q}}^+(t) \sigma_{-\vec{q}'}^-(0) \rangle \right] e^{i\omega t} \quad (5.7)$$

where  $N$  is the total number of sites,  $T$  is the time ordering operator,  $\vec{\sigma}_{\vec{q}} = \frac{1}{2} \sum_{\vec{k}, \alpha\beta} c_{\vec{k}+\vec{q}, \alpha}^\dagger \vec{\tau}_{\alpha\beta} c_{\vec{k}, \beta}$  is the Fourier transform of the local electron spin operator, and  $\vec{\tau}$  are the usual Pauli matrices.

For the translation invariant mean field state the transverse susceptibility is a  $2 \times 2$  matrix at each point in the reduced Brillouin zone due to doubling of the unit cell caused by antiferromagnetic ordering at  $\vec{Q} = (\pi, \pi)$ ,

$$\hat{\chi}_0^{+-} = \begin{bmatrix} \chi_0^{+-}(\vec{q}, \vec{q}, \omega) & \chi_0^{+-}(\vec{q}, \vec{q} + \vec{Q}, \omega) \\ \chi_0^{+-}(\vec{q} + \vec{Q}, \vec{q}, \omega) & \chi_0^{+-}(\vec{q} + \vec{Q}, \vec{q} + \vec{Q}, \omega) \end{bmatrix} \quad (5.8)$$

The RPA transverse susceptibility can be obtained by solving a Dyson equation,

$$\hat{\chi}_{RPA}^{+-} = (\hat{1} - U \hat{\chi}_0^{+-})^{-1} \cdot \hat{\chi}_0^{+-} \quad (5.9)$$

The spin-wave spectrum can be obtained by analyzing the pole structure of  $\hat{\chi}_{RPA}^{+-}$ , which shall be discussed later.

The spin wave dispersion be obtained from the poles of the RPA susceptibility, Eq.5.9, which is given by the condition,

$$\det \left( \begin{bmatrix} 1 - U \chi_0^{+-}(\vec{q}, \vec{q}, \Omega) & -U \chi_0^{+-}(\vec{q}, \vec{q} + \vec{Q}, \Omega) \\ -U \chi_0^{+-}(\vec{q} + \vec{Q}, \vec{q}, \Omega) & 1 - U \chi_0^{+-}(\vec{q} + \vec{Q}, \vec{q} + \vec{Q}, \Omega) \end{bmatrix} \right) = 0 \quad (5.10)$$

where  $\chi_0^{+-}$  are the susceptibilities of the homogeneous mean field state given by,

$$\chi_0^{+-}(\vec{q}, \vec{q}, \omega) = -\frac{1}{2} \sum_{\vec{k}}' \left( 1 + \frac{\epsilon_{\vec{k}} \epsilon_{\vec{k}+\vec{q}} - \Delta^2}{E_{\vec{k}} E_{\vec{k}+\vec{q}}} \right) \left[ \frac{f(E_{\vec{k}+\vec{q}}^A) - f(E_{\vec{k}}^A)}{\omega^+ - (E_{\vec{k}+\vec{q}}^A - E_{\vec{k}}^A)} + \frac{f(E_{\vec{k}+\vec{q}}^B) - f(E_{\vec{k}}^B)}{\omega^+ - (E_{\vec{k}+\vec{q}}^B - E_{\vec{k}}^B)} \right]$$

$$+ \left( 1 - \frac{\epsilon_{\vec{k}} \epsilon_{\vec{k}+\vec{q}} - \Delta^2}{E_{\vec{k}} E_{\vec{k}+\vec{q}}} \right) \left[ \frac{f(E_{\vec{k}+\vec{q}}^B) - f(E_{\vec{k}}^A)}{\omega^+ - (E_{\vec{k}+\vec{q}}^B - E_{\vec{k}}^A)} + \frac{f(E_{\vec{k}+\vec{q}}^A) - f(E_{\vec{k}}^B)}{\omega^+ - (E_{\vec{k}+\vec{q}}^A - E_{\vec{k}}^B)} \right], \quad (5.10a)$$

$$\begin{aligned} \chi_0^{+-}(\vec{q}, \vec{q} + \vec{Q}, \omega) = & \frac{\Delta}{2} \sum_{\vec{k}}' \left( \frac{1}{E_{\vec{k}+\vec{q}}} - \frac{1}{E_{\vec{k}}} \right) \left[ \frac{f(E_{\vec{k}+\vec{q}}^A) - f(E_{\vec{k}}^A)}{\omega^+ - (E_{\vec{k}+\vec{q}}^A - E_{\vec{k}}^A)} - \frac{f(E_{\vec{k}+\vec{q}}^B) - f(E_{\vec{k}}^B)}{\omega^+ - (E_{\vec{k}+\vec{q}}^B - E_{\vec{k}}^B)} \right] \\ & - \left( \frac{1}{E_{\vec{k}+\vec{q}}} + \frac{1}{E_{\vec{k}}} \right) \left[ \frac{f(E_{\vec{k}+\vec{q}}^B) - f(E_{\vec{k}}^A)}{\omega^+ - (E_{\vec{k}+\vec{q}}^B - E_{\vec{k}}^A)} - \frac{f(E_{\vec{k}+\vec{q}}^A) - f(E_{\vec{k}}^B)}{\omega^+ - (E_{\vec{k}+\vec{q}}^A - E_{\vec{k}}^B)} \right] \end{aligned} \quad (5.10b)$$

where  $E_{\vec{k}}^{A,B} = \pm E_{\vec{k}} = \sqrt{\epsilon_{\vec{k}}^2 + \Delta^2}$ ,  $\epsilon_{\vec{k}}$  is the tight-binding dispersion and  $\omega^+ = \omega + i\eta$  with  $\eta \rightarrow 0^+$ . Also note that,  $\chi_0^{+-}(\vec{q} + \vec{Q}, \vec{q}, \omega) = \chi_0^{+-}(\vec{q}, \vec{q} + \vec{Q}, \omega)$  and  $\chi_0^{+-}(\vec{q} + \vec{Q}, \vec{q} + \vec{Q}, \omega)$  can be obtained from Eq.5.10a.

At low temperature  $T \ll \Delta$ , the Fermi factors in Eq.5.10 can be approximated by their zero temperature values, and for  $t_{hop} \ll \Delta$ ,  $E_{\vec{k}}$  can be expanded in powers of  $t_{hop}/\Delta$ . With these approximations the solution of Eq.5.10 is given by Eq.5.4 with  $S = \frac{\Delta}{U}$ .

#### 5.2.4 Langevin dynamics approach

The RPA approach captures the small ‘Gaussian’ fluctuations about an ordered state. However, as the order gets suppressed the moments undergo large angular fluctuations which are not captured within RPA. The Langevin scheme introduced in Sec.2.2.2 provides a framework for dealing with such a scenario, as the dynamics, in this case, is not constrained around a particular quantization axis.

We rewrite the effective Langevin equation in Landau-Lifshitz- Gilbert(LLG) form introduced in Eq.2.18,

$$\begin{aligned} \frac{d\vec{M}_i}{dt} = & \gamma_i(t) \left( \left( \langle \vec{\sigma}_i \rangle_{\{\vec{M}\}} + \vec{\xi}_i \right) - \vec{M}_i \right) + 2U \vec{M}_i \times \left( \langle \vec{\sigma}_i \rangle_{\{\vec{M}\}} + \vec{\xi}_i \right) \\ & + 2U \alpha \vec{M}_i \times \left( \vec{M}_i \times \left( \langle \vec{\sigma}_i \rangle_{\{\vec{M}\}} + \vec{\xi}_i \right) \right) \end{aligned} \quad (5.11a)$$

with  $\gamma_i(t) = (2U/\alpha)(1 + \alpha^2 |\vec{M}_i(t)|^2)$  and the noise defined is given by ( $t_{hop} = 1$ ),

$$\langle \xi_i^a \rangle = 0, \quad \langle \xi_i^a(t) \xi_j^b(t') \rangle = \frac{2\alpha T}{(1 + \alpha^2 |\vec{M}_i|^2)} \delta_{ab} \delta_{ij} \delta(t - t') \quad (5.11b)$$

$\alpha$  is the Gilbert damping parameter, which is set to  $(U/t_{hop})^2$ . The second term in the RHS of

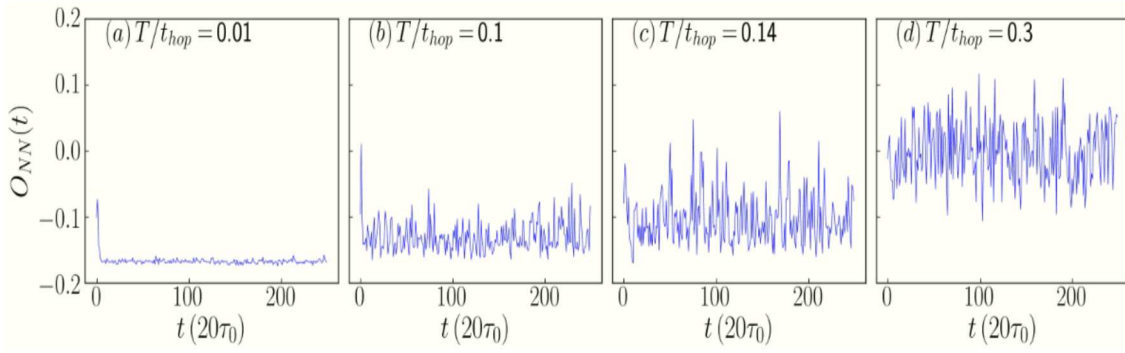


Figure 5.1: Variation of the time-series for the nearest neighbor overlap  $O_{NN}$  across the thermally driven antiferromagnet (AF) to paramagnet (PM) crossover in the 2D Hubbard model. Panels (a)-(d) represent temperatures  $T/t_{hop} = 0.01, 0.1, 0.16$  and  $0.3$  respectively, while the crossover temperature is  $T_c = 0.15t_{hop}$  at  $U/t_{hop} = 6$ . The mean of the time-series at low temperature has a negative value owing to AF correlations, which gradually goes to zero with increasing temperature as the system becomes magnetically disordered.  $\tau_0 = 1/t_{hop}$  is the unit of time.

Eq.5.11a corresponds to the RHS of the Bloch equation (Eq.5.14) in the strong coupling limit, and gives rise to spin waves.

## 5.3 Results from Langevin dynamics

### 5.3.1 The equilibrium case

The primary output of the effective Langevin scheme is a time-series for the auxiliary field  $\vec{M}_i(t)$ . In order to analyse the behaviour of time series we calculate the instantaneous nearest neighbour (NN) overlap  $O_i^{NN}(t)$  of the spins given by,

$$O_i^{NN}(t) = \sum_{z \in NN} \vec{\sigma}_i(t) \cdot \vec{\sigma}_{i+z}(t) \quad (5.12)$$

In Fig. 5.1, we show the variation of  $O_i^{NN}(t)$  with temperature at the central site of a Hubbard model with  $U/t = 6$ , defined on a  $12 \times 12$  square lattice with periodic boundaries. The time-series show fluctuations about a mean value which is negative at low T, owing to antiferromagnetic (AF) correlations, and goes to zero in the high T paramagnetic phase. The fluctuations grow in magnitude as the system is heated, and even below the crossover temperature  $T_c = 0.15t_{hop}$  there are large deviations in  $O^{NN}$  from its mean value due to significant angular fluctuations.

The time series for  $\vec{M}_i$  can be used to compute the dynamical structure factor for the auxiliary fields  $D_{\vec{q}}(\omega)$  which reveals information on the dispersion and broadening of the spin waves. It is given by,

$$D_{\vec{q}}(\omega) = \sum_{ij} \int_0^{t_{max}} \frac{dt}{t_{max}} \vec{M}_i(t) \cdot \vec{M}_j(0) e^{-i\omega t + i\vec{q} \cdot (\vec{r}_i - \vec{r}_j)} \quad (5.13)$$

A similar quantity can also be computed for the electron spin, under the assumption of ‘adiabatic-

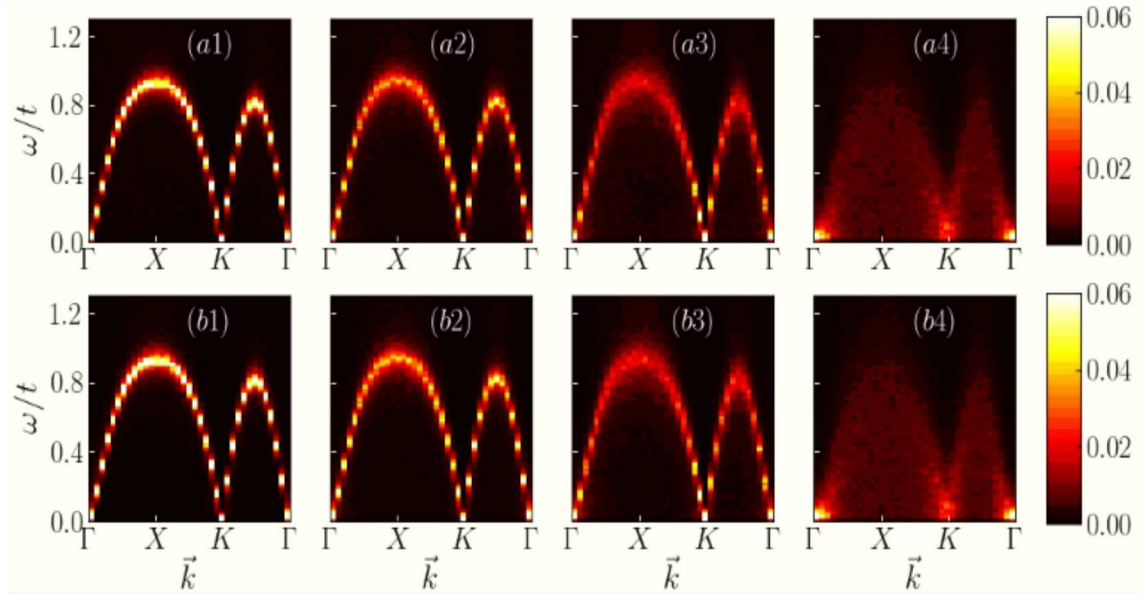


Figure 5.2: (a1)-(a4) Temperature dependence of the auxiliary field dynamical structure factor  $D_{\vec{q}}(\omega)$  at  $U/t_{hop} = 6$ . Panels from left to right correspond to  $T/t_{hop} = 0.001, 0.08, 0.12$  and  $0.18$  respectively. (b1)-(b4) Corresponding plots for the dynamical spin structure factor  $\mathcal{D}_{\vec{q}}(\omega)$ .

ity', by correlating the instantaneous spin configurations in space and time to get the dynamical spin structure factor  $\mathcal{D}_{\vec{q}}(\omega)$ .

Fig.5.2 shows the temperature dependence of both the auxiliary field and spin dynamical structure factors. They look identical across the entire range of temperature. At low temperatures (Panels (a1) and (a2)) the spin waves are weakly damped and the dispersion is sharply defined at all wavevectors. There are Goldstone modes at  $(0, 0)$  and  $(\pi, \pi)$ . At intermediate temperatures (Panel (a3)) the spectrum shows broadening, away from the Goldstone modes. At temperatures larger than the crossover temperature  $T_c$ , the spectrum becomes diffusive and does not possess sharply defined modes, although some low energy weight at the Goldstone wavevectors survives.

Fig.5.3 shows the dependence of the low temperature auxiliary field dynamical structure factor on the Hubbard interaction strength  $U$  for  $U/t_{hop} = (a)6, (b)8$  and  $(c)20$ . Both the spin

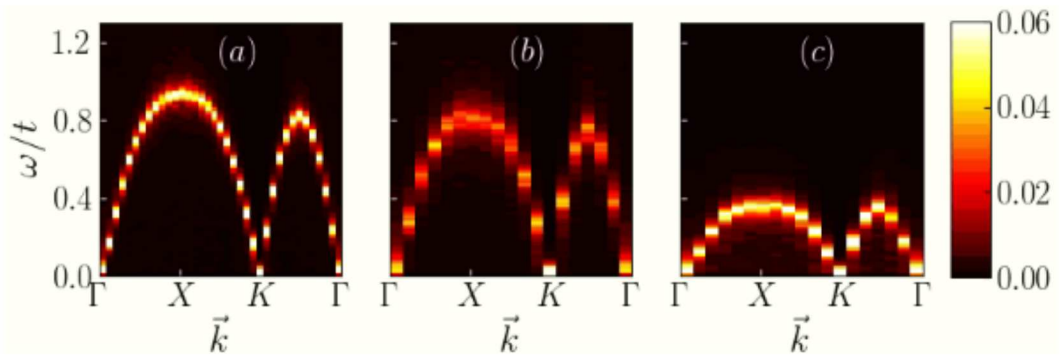


Figure 5.3: Variation in the auxiliary field dynamical structure factor with changing onsite Hubbard interaction strength at  $T/t_{hop} = 0.01$ . The panels correspond to  $U/t_{hop}$  values (a) 6, (b) 8 and (c) 20.



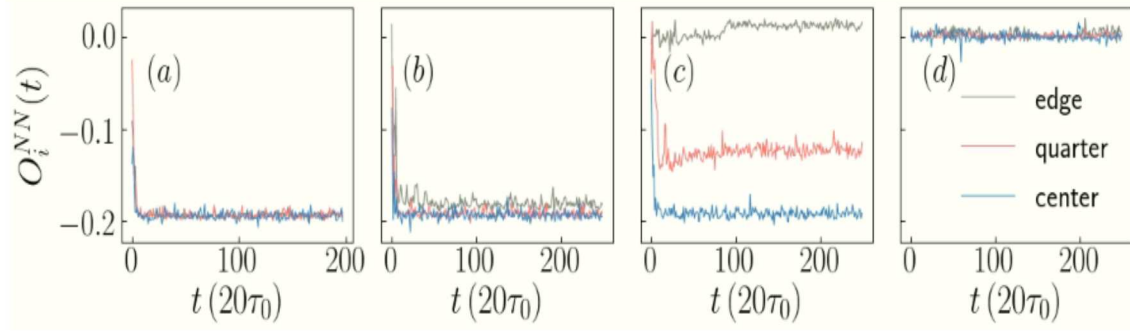


Figure 5.4: Time-series of the nearest neighbour overlap of the spins  $O_i^{NN}$  at the edge, quarter (half-way between the edge and the center) and the central sites with varying bias  $V/t_{hop}$  values (a) 0, (b) 4, (c) 5 and (d) 6. The Hubbard interaction  $U/t_{hop} = 8$  and the temperature  $T/t_{hop} = 0.01$ .

wave velocity and the magnetic bandwidth decrease with increasing  $U$ . The dispersion is well approximated by a Heisenberg model at  $U/t_{hop} \sim 20$ . For lower values of  $U$ , the corrections due to higher order spin coupling terms become important.

### 5.3.2 Effect of voltage bias

Next, we focus on the low temperature out of equilibrium dynamics of the Hubbard model at moderately large  $U (= 8t_{hop})$ . In Fig.5.4, we plot the nearest neighbour overlaps of the electron spins  $O_i^{NN}$  as a function of time, given by Eq.5.12, for three different sites - the edge site, the site midway between the center, which we call ‘quarter’ site, and the edge and the central site, across a range of voltages which sweep through the insulator metal transition ( $V_c = 5.2t_{hop}$ ). At  $V = 0$ , Fig.5.4(a), the overlaps at all the three sites equilibrate to a negative value, owing to the antiferromagnetic correlations.

As the voltage is increased the mean of the time-series differ for the three sites, with the edge being most affected, followed by the ‘quarter’ site while the mean overlap for the central site

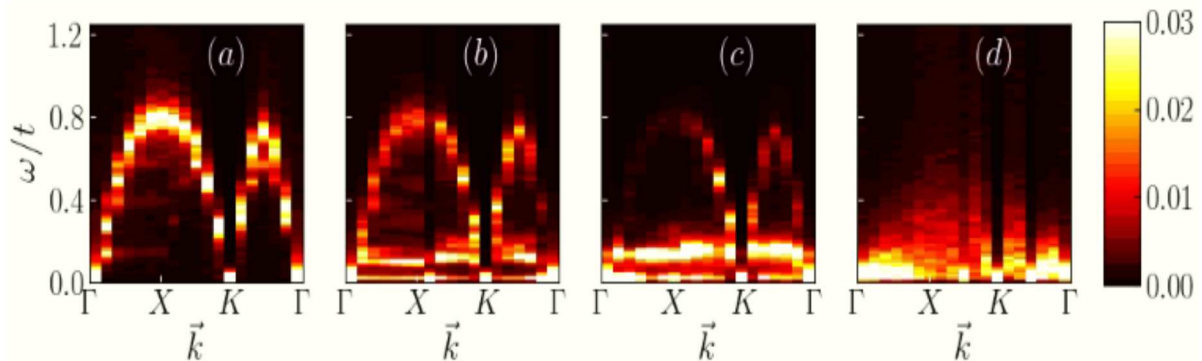


Figure 5.5: Magnon spectrum with increasing bias ( $V$ ) in the driven dissipative 2D Hubbard model at  $U/t_{hop} = 8$  and temperature  $T/t_{hop} = 0.01$ . Panels (a)-(d) correspond to bias  $V/t_{hop} = 0, 4, 5$  and  $6$  respectively. The system size is  $12 \times 12$  with periodic boundary condition in the transverse direction.

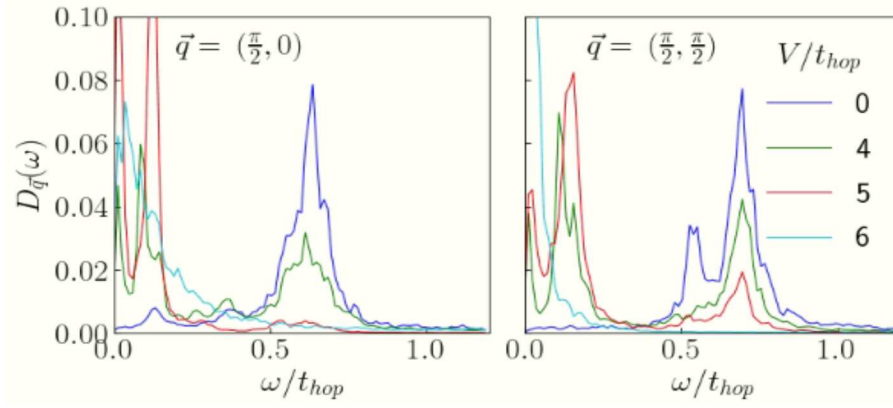


Figure 5.6: Variation of lineshapes with bias voltage for  $\vec{q} = (\frac{\pi}{2}, 0)$  and  $(\frac{\pi}{2}, \frac{\pi}{2})$  at  $U/t_{hop} = 8$  and  $T/t_{hop} = 0.01$ . The multi-peak features are due to the spatial inhomogeneity in the longitudinal direction due to the presence of leads. It also contributes to the unusual broadening of the peaks along with Gilbert damping and longitudinal relaxation of the local moments.

remains almost pinned to its  $V = 0$  value for  $V < V_c$  (Fig.5.4(b) and (c)). This is primarily due to the bias-dependent ‘penetration length’ for the 2D problem, as discussed in Sec.3.3.3 which leads to an exponentially larger suppression of the moment amplitudes close to the edges as compared to the center. Beyond  $V_c$ , the moment amplitudes throughout the system get quenched which leads to large angular fluctuations of the local moments and the mean overlap goes to zero for all sites.

The effect of voltage bias on the magnon spectrum can be analysed by calculating the auxiliary field dynamical structure factor  $D_{\vec{q}}(\omega)$ , as given in Eq.5.13. Fig.5.5 shows the low temperature ( $T/t_{hop} = 0.01$ ) magnon spectrum at  $U/t_{hop} = 8$ , with varying voltage. At  $V/t_{hop} = 0$ , Fig.5.5(a), the spectrum has diffuse modes in addition to the usual spin wave mode. This is due to the breaking of translation symmetry along the longitudinal direction as a result of coupling with baths at the edges. With increasing  $V$ , a low energy branch develops in the spectrum (Fig.5.5 (b) and (c)) and as  $V$  approaches  $V_c$  more and more weight is transferred to the low energy part. Beyond  $V_c$  the spin wave mode vanishes and a diffuse spectrum at low energy remains (Fig.5.5 (d)).

Fig. 5.6 shows the lineshapes for  $\vec{q} = (\frac{\pi}{2}, 0)$  and  $(\frac{\pi}{2}, \frac{\pi}{2})$  with varying  $V/t_{hop}$ . They show the development of a low energy peak with increasing  $V$  and, as the system undergoes an insulator metal transition, a complete shift of weight close to  $\omega = 0$  from the original spin wave peak.

## 5.4 Discussion

The strong coupling expansion of the Hubbard model gives a quantum Heisenberg model, as discussed in Sec.5.2.2. However, the Langevin scheme is based on an approximate treatment of the Hubbard model which probes the dynamics of the effective spin-fermion Hamiltonian in Eq.2.4g. The assumption of a ‘classical’ noise misses out the quantum dynamics at zero



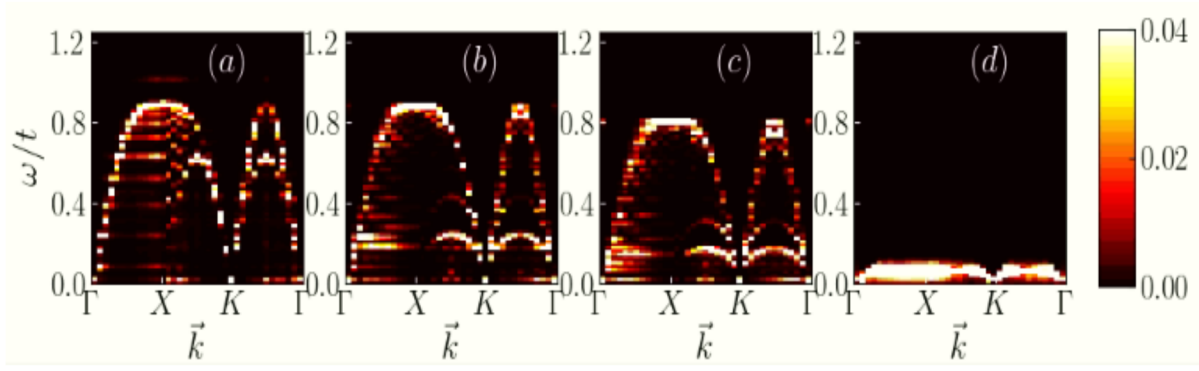


Figure 5.7: Magnon spectrum with increasing bias ( $V$ ) for the effective Heisenberg model. The moment amplitudes are fixed by the  $T = 0$  nonequilibrium mean field profiles. Panels (a)-(d) correspond to bias  $V/t_{hop} = 0, 4, 5$  and  $6$  respectively. The system size is  $24 \times 24$  with periodic boundary condition in the transverse direction.

temperature. The effective Langevin dynamics at low temperature is captured by a classical Heisenberg model which can be obtained within a strong coupling expansion of the spin-fermion Hamiltonian in Eq.2.4g.

$$H_{eff-cl} = J \sum_{\langle ij \rangle} \vec{M}_i \cdot \vec{M}_j \quad (5.14)$$

where  $\vec{M}_i^c \equiv \vec{M}_i$  is a  $O(3)$  vector and we have rescaled the  $\{\vec{M}^{c,q}\}$  fields as  $\vec{M}^{c,q} \rightarrow \frac{U}{2} \vec{M}^{c,q}$  to make them dimensionless. Using Poisson bracket relations we can write down the classical equations of motion for the Hamiltonian above.

$$\frac{d\vec{M}_i}{dt} = J \sum_{j \in NN} \vec{M}_i \times \vec{M}_j \quad (5.15)$$

This is the Bloch equation for classical spins. The classical Heisenberg model lacks intrinsic dynamics at  $T = 0$ , while the quantum model has dynamical magnon excitations even at  $T = 0$ . In order to impart dynamics to the classical model one can (a) impose nonequilibrium initial conditions, or (b) simulate the system at finite temperature.

Here, we take the first route to simulate the effective low temperature dynamics with increasing bias. As we have seen in Ch. 3, the effect of bias is encapsulated in a modified amplitude profile of the local moments which can be parametrised by two voltage dependent parameters, a penetration length  $\xi$  and a scale factor  $A$ . Fig.5.7 shows the magnon spectrum obtained from the effective Heisenberg model by evolving the Bloch equation Eq.5.15 for different choices of  $\xi$  and  $A$  corresponding to a range of voltages. Panels (a)-(d) correspond to  $V = 0, 4, 5$  and  $6$  respectively. The gross features of the spectrum in Fig.5.5, like the diffusive features due to broken translation invariance and the formation of a low energy branch with increasing  $V$  are captured by this effective model. However, due to absence of Gilbert damping and longitudinal relaxation the broadening of the lineshapes aren't captured correctly. This becomes more prominent at higher values of the bias. From this, one can also conclude that the low energy features arise

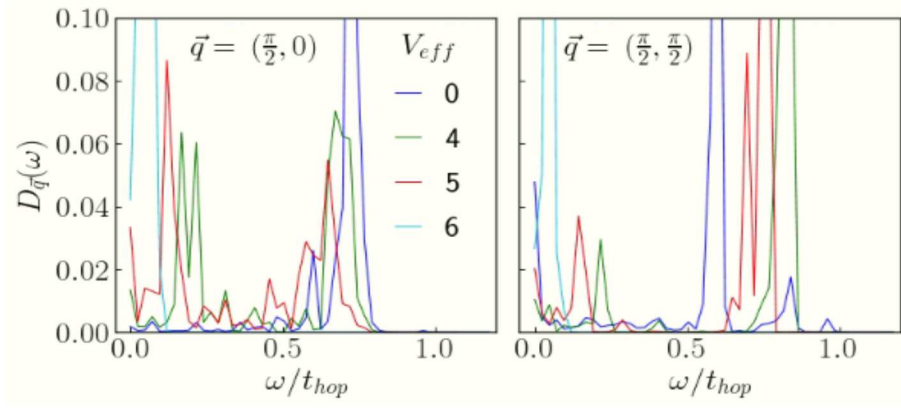


Figure 5.8: Variation of lineshapes of the amplitude modulated Heisenberg model at  $J = 0.5t_{hop}$  with effective bias voltage ( $V_{eff}$ ) for  $\vec{q} = (\frac{\pi}{2}, 0)$  and  $(\frac{\pi}{2}, \frac{\pi}{2})$ . The effective voltage enters the model through the parameters  $A$  and  $\xi$ , which define the approximate amplitude profile of the local moments through Eqs.3.6.

from the quenched moments close to the edges, and the shift of spectral weight to lower energies is due to the effect of bias penetrating deeper into the system as the voltage is tuned across the insulator-metal crossover in 2D.

# Nonequilibrium response and dynamics in the Mott insulator

Name: Arijit Dutta  
Enrolment no.: PHYS08201105001

## List of publications

### Published

1. “Spatial behavior in a Mott insulator near the voltage-driven resistive transition”, Arijit Dutta and Pinaki Majumdar, Phys. Rev. B., **2020**, 101, 245155.

### Preprint

1. “Thermal fluctuation driven nonequilibrium resistive and magnetic transitions in a voltage biased Mott insulator”, Arijit Dutta and Pinaki Majumdar, arxiv:2009.05533.